NASA Contractor Report 3626

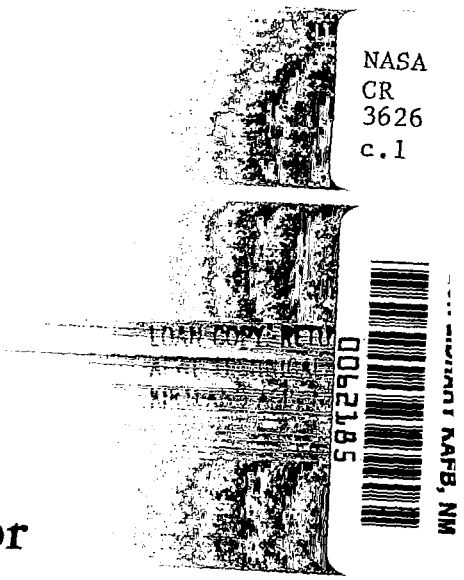

The Transfer Function Method for Gear System Dynamics Applied to Conventional and Minimum Excitation Gearing Designs

William D. Mark

CONTRACT NAS3-21978
OCTOBER 1982

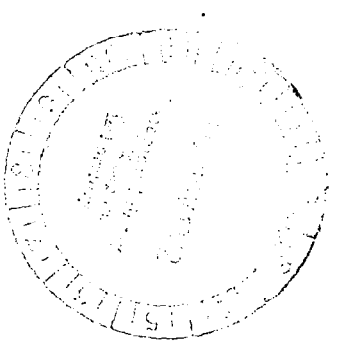

NASA

NASA Contractor Report 3626

The Transfer Function Method for Gear System Dynamics Applied to Conventional and Minimum Excitation Gearing Designs

William D. Mark
Bolt Beranek and Newman Inc.
Cambridge, Massachusetts

Prepared for
Lewis Research Center
under Contract NAS3-21978

National Aeronautics
and Space Administration

**Scientific and Technical
Information Branch**

1982

SUMMARY

A transfer function method for predicting the dynamic responses of gear systems with more than one gear mesh is developed and applied to the NASA Lewis four-square gear fatigue test apparatus. Methods for computing bearing-support force spectra and temporal histories of the total force transmitted by a gear mesh, the force transmitted by a single pair of teeth, and the maximum root stress in a single tooth are developed. Dynamic effects arising from other gear meshes in the system are included.

It is shown that the above response metrics depend fundamentally on the dynamic transmission error of the mesh under consideration. The Fourier transform of the dynamic transmission error of a mesh is expressed as a linear combination of the Fourier transforms of the static transmission errors of all meshes in the system. The complex frequency-dependent coefficients in this expression, which we call transmission error dynamic increment functions, characterize the dynamic properties of the gearing system. Expressions for these functions are derived and plotted for the NASA Lewis gear fatigue test apparatus.

A profile modification design method to minimize the vibration excitation arising from a pair of meshing gears is reviewed and extended. Families of tooth loading functions required for such designs are developed and examined for potential excitation of individual tooth vibrations. The profile modification design method is applied to a pair of test gears in the NASA Lewis fatigue test apparatus using an approximate tooth stiffness calculation provided by NASA.

The above described methods are used to compute the bearing-support force spectra and temporal histories of the force transmitted by a pair of teeth and the tooth root stresses for two sets of profile modifications – a conventional modification consisting of linear tip relief, and the above mentioned profile modification for minimum vibration excitation. Significant differences in the dynamic forces transmitted by the teeth and in the tooth root stresses are predicted for these two cases. These differences are discussed and are related to the gear system dynamic properties.

The above computational methods are carried out, for the most part, in the frequency domain using the fast Fourier transform computational algorithm. The required computer programming was carried out by Mr. Robert Fabrizio with supplementary programming by Ms. Caroline Buchman and Mr. Edward Campbell.

THE EXCITATION

A time varying component of vibratory excitation arises from each meshing pinion-gear pair in a gearing system. For each gear element — i.e., pinion or gear — the principal source of this excitation component is the deviations of the active tooth surfaces of that gear element, under loading, from perfect involute surfaces with uniform spacing. Thus, this principal source of excitation is most naturally described as a *displacement* type of excitation as opposed to a force type of excitation. This displacement excitation gives rise to a time varying component in the total force transmitted normal to the tooth surfaces which is also dependent on the dynamic parameters of the gearing system — i.e., on the overall configuration and the mass and interial properties of the system.

In addition, there are time varying tangential forces between meshing pairs of teeth that arise from the friction and sliding action of the teeth. The component of vibratory excitation caused by these frictional forces is generally believed to be small in comparison with the component due to deviations of the loaded teeth from perfect involute surfaces. These frictional forces therefore will be neglected in this report.

Gear elements with perfect, rigid, uniformly spaced involute teeth transmit exactly uniform angular velocities. Thus, to predict the response of a gearing system to deviations of the loaded teeth from perfect involute surfaces, we require the deviations of the angular positions of individual gear elements under loading from the positions of their perfect, rigid, involute counterparts. In this report, we shall use the static transmission error [1-3] to describe this component of the vibratory excitation, where *the static transmission error of a meshing gear pair can be defined* [4,5] *as the deviation* $\delta\theta$ *from linearity of the angular position* θ *of a gear measured as a function of the angular position of the gear it meshes with when the gear pair is transmitting a constant torque at low enough speed so that inertial effects are negligible.* Our analysis to follow will use the lineal static transmission error,

$$\zeta = R_b \delta\theta \ , \tag{1.1}$$

where R_b is the base circle radius [6] of the gear whose angular transmission error is $\delta\theta$. When the equations of motion of the gearing system are written later in this report, we shall see how the lineal transmission error ζ is used to predict the vibratory response of points of interest within the system.

The static transmission error of a pair of meshing gears is made up of contributions from each of the two gears. For each

gear, there is a contribution from the elastic deformations of the teeth and gear body, and a contribution from the geometric deviations of the unloaded teeth from perfect uniformly spaced involute surfaces. Furthermore, in References 4 and 5, we have found it useful to further decompose these geometric deviations into a mean component and a random component. The *mean* geometric deviation component for a pinion or gear is defined as the *tooth surface* formed by taking the average of all tooth surfaces on the pinion or gear under consideration. The *random* component of the geometric deviation of a tooth surface is defined as the deviation of that tooth surface from the mean tooth surface. Thus, every tooth surface on a pinion or gear has the same mean deviation component; however, the random deviation component generally will differ from one tooth to the next. It is shown in References 4 and 5 that the elastic deformations and the mean component of the geometric deviations of the teeth give rise to the tooth meshing harmonics of vibratory excitation and response, whereas the random component of the geometric deviations gives rise to the rotational harmonics, and especially, to the so-called sideband components of the spectrum which occur at the tooth meshing harmonic frequencies plus and minus one or a few rotational harmonic frequencies. The random component of the deviations provides no contribution to the tooth meshing harmonics. Proofs and full discussion of these facts can be found in References 4 and 5.

In high quality, highly loaded, ground aerospace gearing, the random component of the deviations of the tooth faces from perfect, uniformly spaced involute surfaces is generally small in comparison with the mean component of the deviations and the component due to elastic deformations. Hence, in the analysis to follow, we shall mainly concentrate on the mean deviation of the tooth surfaces and the component caused by elastic deformations. A full discussion of the random component of the deviations and its effects on the excitation spectrum can be found in References 4 and 5.

Fourier Series Representation of Tooth-Meshing Harmonic Components of the Excitation

Computation of the response of vibratory systems to dynamic inputs generally is most easily carried out in the frequency domain, where temporal convolution or Duhamel integrals are replaced by simple multiplications. Since the excitation components of most interest are the mean component of the deviations of the tooth surfaces from perfect involute surfaces and the component due to elastic deformations, each of which gives rise to a periodic excitation with period equal to the tooth spacing interval, the appropriate description of the static transmission error of

these components for later use in the equations of motion is their Fourier series representation. To generate the Fourier series representation of these static transmission error components, we shall use for our independent variable the quantity

$$x = R_b \theta \ , \tag{1.2}$$

where θ is the nominal angular position in radians of one gear of the pair whose base circle radius is R_b. Thus, the same lineal variable x describes the nominal positions of both gears in a meshing pair, since the *product* $R_b\theta$ is the same for both of the gears.

A thorough analysis and discussion of the Fourier series representation of the static transmission error can be found in References 4 and 5. Thus, in this section, we shall summarize the formulas required for computations of the Fourier series representation of the mean or deterministic component $\zeta_m(x)$ of the static transmission error of a generic meshing pair of *spur* gears with appropriate reference to the derivations of these formulas. We shall then provide a brief treatment of the contribution from tooth-spacing errors.

From Eqs. (60) and (61) of Reference 4, we see that when the random component $\zeta_r(x)$ of the static transmission error is neglected, we can express the resulting mean component of the static transmission error as

$$\zeta_m(x) = \zeta_W(x)_0 + \zeta_m^{(1)}(x) + \zeta_m^{(2)}(x) \ , \tag{1.3}$$

where $\zeta_W(x)_0$ is the (loading dependent) component resulting from elastic deformations of the teeth and gear bodies, and $\zeta_m^{(1)}(x)$ and $\zeta_m^{(2)}(x)$ each represents the contribution to the static transmission error arising from the mean tooth face deviations on gear $(\cdot)$. Numbered superscripts in parentheses designate one gear or the other in a meshing pair. Superscript W on the loading dependent component represents dependence of that component on force W transmitted by the mesh, and subscript 0 designates that the transmitted load is assumed to be the constant value W_0.

Following Eqs. (64) through (67) of Reference 4, we can express the Fourier series representation of the mean component of the static transmission error as

$$\zeta_m(x) = \sum_{n=-\infty}^{\infty}{}' \alpha_{mn} \exp(i2\pi nx/\Delta) \ , \tag{1.4}$$

where, from the linear relationship on the right-hand side of Eq. (1.3), the Fourier series coefficients α_{mn} of $\zeta_m(x)$ may be expressed as

$$\alpha_{mn} = \frac{1}{\Delta} \int_{-\Delta/2}^{\Delta/2} \zeta_m(x) \exp(-i2\pi nx/\Delta) \, dx$$

$$= \alpha_{Wn} + \alpha_{mn}^{(1)} + \alpha_{mn}^{(2)} \tag{1.5}$$

and where α_{Wn}, $\alpha_{mn}^{(1)}$, and $\alpha_{mn}^{(2)}$ are, respectively, the Fourier expansion coefficients of the load-dependent component $\zeta_W(x)_0$ and the mean deviation components $\zeta_m^{(1)}(x)$ and $\zeta_m^{(2)}(x)$ from the teeth of gears (1) and (2) of the pair — i.e.,

$$\alpha_{Wn} = \frac{1}{\Delta} \int_{-\Delta/2}^{\Delta/2} \zeta_W(x)_0 \exp(-i2\pi nx/\Delta) \, dx \tag{1.6}$$

$$\alpha_{mn}^{(\cdot)} = \frac{1}{\Delta} \int_{-\Delta/2}^{\Delta/2} \zeta_m^{(\cdot)}(x) \exp(-i2\pi nx/\Delta) \, dx. \tag{1.7}$$

Let us concentrate now on determining a useful set of expressions for computing the Fourier series coefficients α_{Wn} of the loading dependent component of the static transmission error. From Eq. (68) of Reference 4, we see that α_{Wn} can be expressed as

$$\alpha_{Wn} = W_0 \alpha_{(1/K)n}, \ n = 0, \pm 1, \pm 2, \cdots \tag{1.8}$$

where the constant force W_0 transmitted by the mesh is defined in the direction determined by the intersection of the base plane and axial plane, and $\alpha_{(1/K)n}$ are the Fourier series coefficients of the reciprocal of the total mesh stiffness. According to Eqs. (77) and (87) of Reference 4, these latter Fourier series coefficients can be computed to any desired degree of accuracy from the expression

$$\alpha_{(1/K)n} \approx \frac{1}{\overline{K}_T} \sum_{\ell=0}^{M} \binom{M+1}{\ell+1} (-1)^{\ell} \left(\frac{\alpha_{Kn}}{\overline{K}_T}\right)^{[\ell]} , \tag{1.9}$$

where the accuracy of this expression increases with increasing M. According to Table I on p. 1761 of Reference 5, M should be taken at least equal to M = 3 for accurate calculations of $\alpha_{(1/K)n}$ for spur gears. The quantities $\binom{M+1}{\ell+1}$ are the binomial coefficients

$$\binom{M+1}{\ell+1} \triangleq \frac{(M+1)!}{(\ell+1)!(M-\ell)!} , \tag{1.10}$$

whereas, in Eq. (1.9), we have also used the definition

$$\left(\frac{\alpha_{Kn}}{\overline{K}_T}\right)^{[\ell]} \triangleq \begin{cases} \left(\frac{\alpha_{Kn}}{\overline{K}_T}\right)^{1} * \left(\frac{\alpha_{Kn}}{\overline{K}_T}\right)^{2} * \cdots * \left(\frac{\alpha_{Kn}}{\overline{K}_T}\right)^{\ell-1} * \left(\frac{\alpha_{Kn}}{\overline{K}_T}\right), & \ell > 1 \\ \left(\frac{\alpha_{Kn}}{\overline{K}_T}\right) & \ell = 1 \\ \delta_{n,0} & \ell = 0 , \end{cases} \tag{1.11}$$

where $\delta_{n,0}$ is Kronecker's delta

$$\delta_{i,j} \triangleq \begin{cases} 1 , & i = j \\ 0 , & \text{otherwise,} \end{cases} \tag{1.12}$$

and where the vertically centered asterisks in Eq. (1.11) denote discrete convolutions defined by the right-hand equality in Eq. (G12) on p. 1428 of Reference 4. Notice that for $\ell = 1,2,3, \ldots,$ we have

$$\left(\frac{\alpha_{Kn}}{\overline{K}_T}\right)^{[\ell]} = \left(\frac{\alpha_{Kn}}{\overline{K}_T}\right)^{[\ell-1]} * \left(\frac{\alpha_{Kn}}{\overline{K}_T}\right) . \tag{1.13}$$

The quantities α_{Kn} are the Fourier series coefficients of the total mesh stiffness as defined by Eq. (75) of Reference 4 for $\ell=1$, and $\bar{K}_T$ is the mean value of the total mesh stiffness as defined by Eq. (F.2) on p. 1427 of Reference 4. These latter two quantities can be computed from the spur gear local tooth pair stiffness $K_S(z)$ which is described in detail in Appendix A of this report. Since we are considering here only spur gears, which have zero helix angles, we have in these cases from Eq. (C4) of Reference 4, (L/A) = 0. For spur gears, we therefore have from Eq. (86) of Reference 4,

$$\frac{\alpha_{Kn}}{\bar{K}_T} = \frac{\hat{K}_{TC}[0,(nL/D\Delta)]}{\hat{K}_{TC}(0,0)} , \tag{1.14}$$

whereas, from Eq. (85) of Ref. 4, we have

$$\bar{K}_T = \frac{L}{D\Delta} \hat{K}_{TC}(0,0) , \tag{1.15}$$

which reduces our problem to determination of $\hat{K}_{TC}[0,(nL/D\Delta)]$. Let us define the spur gear local tooth pair stiffness $K_S(z)$ as

$$K_S(z) \triangleq \int_{-F/2}^{F/2} K_{TC}(y,z)dy , \tag{1.16}$$

where F is the face width of the gear and $K_{TC}(y,z)$ is the local tooth pair stiffness per unit length of line of contact expressed in the tooth coordinates defined by Eqs. (15), (16), and (19) of Reference 4. From Eq. (82) of Reference 4 and Eq. (1.16) above, we then have

$$\hat{K}_{TC}[0,(nL/D\Delta)] = \int_{-D/2}^{D/2} K_S(z)e^{-i2\pi(nL/D\Delta)z}dz \tag{1.17}$$

and

$$\hat{K}_{TC}(0,0) = \int_{-D/2}^{D/2} K_S(z)dz, \tag{1.18}$$

where D is the total height of the active tooth surface as illustrated in Fig. 4 of Reference 4. Coordinate z is defined in Appendix A, and L is the length of line of contact illustrated in Fig. 2 of Reference 4 which is related to D by

$$\frac{L}{D} = \csc\phi, \tag{1.19}$$

according to Eq. (C8) on p. 1426 of Reference 4 where ϕ is the pressure angle. According to Eqs. (A5) and (A6) on p. 1424 of Reference 4, Δ is the base pitch which is related to the circular pitch Δ_c by

$$\Delta = \Delta_c(R_b/R) = \Delta_c \cos\phi \tag{1.20}$$

where R_b is the base circle radius and R is the pitch circle radius. The overall parameter $L/D\Delta$ that appears repeatedly above therefore can be expressed in terms of the pressure angle ϕ and the circular pitch Δ_c by

$$\frac{L}{D\Delta} = \frac{\csc\phi \ \mathrm{ctn}\phi}{\Delta_c} . \tag{1.21}$$

Once a value of M (M≥3) *is chosen, Eqs. (1.8) through (1.21) determine the Fourier series coefficients* α_{Wn}, n=0, ±1, ±2,··· *of the load dependent component of the static transmission error in terms of the loading* W_0 *carried by the mesh, the local tooth pair stiffness* $K_S(z)$ *over the range* $-D/2 \leq z \leq D/2$, *and the design parameters* ϕ *and* Δ_c.

We turn now to determining an analogous set of expressions useful for computing the Fourier series coefficients $\alpha_{mn}^{(\cdot)}$ of the mean deviation components of the static transmission error for either gear (·) = (1) or (2) of a meshing pair. According to Eq. (94) of Reference 4, the mean deviation Fourier series coefficients can be expressed as

$$\alpha_{mn}^{(\cdot)} = \alpha_{(1/K)n} * \alpha_{m'n}^{(\cdot)} , \quad n = 0, \pm1, \pm2, \cdots \tag{1.22}$$

where the coefficients $\alpha_{(1/K)n}$ are given by Eqs. (1.9) through (1.21), and where the vertically centered asterisk again denotes the discrete convolution defined by the right-hand equality in Eq. (G12) on p. 1248 of Reference 4. The coefficients $\alpha_{m'n}^{(\cdot)}$ are determined from the mean profile modification of gear (·) by first using Eq. (92) of Reference 4 applied to the case of spur gears [where $\psi_b = 0$ and $(L/A) = 0$] – i.e.,

$$\alpha_{m'n}^{(\cdot)} = \frac{L}{D\Delta} \hat{m}_{KC}^{(\cdot)} [0, (nL/D\Delta)]. \tag{1.23}$$

Since our interest here is spur gearing, we shall now restrict the general theory presented in References 4 and 5 to the case where the mean tooth face modification $m_C^{(\cdot)}(y,z)$ of gear $(\cdot)$ (defined on p. 1417 of Reference 4) is independent of the axial coordinate y illustrated in Fig. 4 of Reference 4. That is, let us define for spur gears the mean profile modification of gear $(\cdot)$ as

$$m_S^{(\cdot)}(z) \triangleq m_C^{(\cdot)}(\cdot,z) \ , \tag{1.24}$$

where $m_C^{(\cdot)}(\cdot,z)$ is the tooth face modification $m_C^{(\cdot)}(y,z)$ that we here assume to be independent of axial location y. Let us further define for spur gears the stiffness weighted mean profile modification $m_{KS}^{(\cdot)}(z)$ as the axial integral of the stiffness weighted tooth face modification $m_{KC}^{(\cdot)}(y,z)$ expressed by Eq. (48) of Reference 4 — i.e.,

$$\begin{aligned} m_{KS}^{(\cdot)}(z) &\triangleq \int_{-F/2}^{F/2} m_{KC}^{(\cdot)}(y,z)dy \\ &= \int_{-F/2}^{F/2} K_{TC}(y,z)m_C^{(\cdot)}(\cdot,z)dy \\ &= K_S(z)m_S^{(\cdot)}(z) \ , \end{aligned} \tag{1.25}$$

where the last line follows from Eqs. (1.16) and (1.24). Setting $g_1 = 0$ in Eq. (91) of Reference 4, we see that $\hat{m}_{KC}^{(\cdot)}[0,(nL/D\Delta)]$ can be expressed using Eq. (1.25) as

$$\hat{m}_{KC}^{(\cdot)}[0,(nL/D\Delta)] = \int_{-D/2}^{D/2} K_S(z)m_S^{(\cdot)}(z)e^{-i2\pi(nL/D\Delta)z}dz. \tag{1.26}$$

Equations (1.22), (1.23), and (1.26) determine the Fourier series coefficients $\alpha_{mn}^{(\cdot)}$, $n = 0, \pm1, \pm2, \cdots$ *of the contribution to the static transmission error from the mean profile modification of gear* $(\cdot)$, $(\cdot) = (1)$ or (2), *in terms of the coefficients* $\alpha_{(1/K)n}$, $n = 0, \pm1, \pm2, \cdots$ *determined by Eq. (1.9), the local tooth pair*

stiffness $K_S(z)$ *described by Eq. (1.16), the mean profile modification* $m_S^{(\cdot)}(z)$ *of gear* $(\cdot)$, *and the design parameters given by Eq. (1.21).*

When the Fourier series coefficients of the load-dependent component of the static transmission error, Eq. (1.8), are added to the Fourier series coefficients of the mean profile modification component from each gear, Eq. (1.22), $(\cdot) = (1)$ or (2), *as shown in Eq. (1.5), we have a complete expression for the Fourier series coefficients of the tooth meshing harmonic components of the static transmission error of the meshing gear pair.* These formulas, and the ones to follow, take into full account the alternating numbers of teeth in contact as the gears rotate.

Fourier Series Coefficients of Rotational Harmonic Components Caused by Tooth-Spacing Errors

A thorough discussion of the contributions of manufacturing errors that cause variations in the running surfaces of gear teeth from one tooth to the next can be found in References 4 and 5. That treatment is capable of predicting the rotational harmonic contributions caused by any errors of this type. However, in high quality ground aerospace spur gears, we would expect the dominant manufacturing error component to be that associated with tooth spacing errors. Formulas for the rotational harmonic contributions caused by tooth spacing errors are summarized below.

The tooth spacing errors on gear $(\cdot)$ of a meshing pair, $(\cdot) = (1)$ or (2), give rise to a periodic contribution to the static transmission error, where the period is the base circle circumference of the gear. If $N^{(\cdot)}$ denotes the number of teeth on the gear and Δ the base pitch, then that period is $N^{(\cdot)}\Delta$. Thus, there are two sets of such rotational harmonics generated from each pair of meshing gears, one set from each gear, unless the numbers of teeth on the two gears is the same.

Let $\varepsilon_j^{(\cdot)}$ denote the accumulated tooth spacing error of tooth j of gear $(\cdot)$ as defined by Eq. (107) of Reference 5 with $\varepsilon_j^{(\cdot)} \equiv b_{j,00}^{(\cdot)}$. Let $B^{(\cdot)}(n)$ denote the finite discrete Fourier transform of the sequence $\varepsilon_j^{(\cdot)}$, $j = 0,1,\cdots,N-1$:

$$B^{(\cdot)}(n) \triangleq \frac{1}{N^{(\cdot)}} \sum_{j=0}^{N^{(\cdot)}-1} \varepsilon_j^{(\cdot)} e^{-i2\pi nj/N^{(\cdot)}}, \quad n=0,\pm1,\pm2,\cdots . \qquad (1.27)$$

Then, we see from Eqs. (52) and (53) of Reference 5 that the Fourier series coefficients $\alpha_{rn}^{(\cdot)}$ of the component of the static transmission

error caused by the tooth spacing errors of gear (•) can be expressed by the simple multiplicative relationship

$$\alpha_{rn}^{(\bullet)} = B^{(\bullet)}(n)\,\hat{\phi}_{00}\left(\frac{n}{N^{(\bullet)}\Delta}\right), \quad n = 0,\pm1,\pm2,\cdots \tag{1.28}$$

where, here, n denotes the rotational harmonic of gear (•) where the period of the fundamental component n = 1 is $N^{(\bullet)}\Delta$. From Eq. (110) of Reference 5, we see that the mesh transfer function for tooth spacing errors $\hat{\phi}_{00}\left(\frac{n}{N^{(\bullet)}\Delta}\right)$ appearing in Eq. (1.28) can be expressed as

$$\hat{\phi}_{00}\left(\frac{n}{N^{(\bullet)}\Delta}\right) = \frac{\sin[(n/N^{(\bullet)})\pi L/\Delta]}{(n/N^{(\bullet)})\pi L/\Delta}$$

$$- \sum_{\substack{n'=-\infty \\ \text{except} \\ n'=0}}^{\infty} w_{00}\left(\frac{n}{N^{(\bullet)}}, n'\right) \frac{\sin(n'\pi L/\Delta)}{n'\pi L/\Delta} \frac{\sin\{[(n/N^{(\bullet)})-n']\pi L/\Delta\}}{[(n/N^{(\bullet)})-n']\pi L/\Delta} \tag{1.29}$$

where we have used $g = n/N^{(\bullet)}$ and the fact that $j_0(x) = \sin x/x$ as indicated by Eq. (126) of Reference 5. The function w_{00} in Eq. (1.29) is defined by Eqs. (93) and (94) of Reference 5 — i.e.,

$$w_{00}\left(\frac{n}{N^{(\bullet)}}, n'\right) = \frac{1}{2}\,\mathrm{rect}\left[\frac{1}{2}\left(\frac{n}{N^{(\bullet)}} - n'\right)\right]\left\{1+\cos\left[\pi\left(\frac{n}{N^{(\bullet)}} - n'\right)\right]\right\} \tag{1.30}$$

where from Eq. (90) of Reference 5, we see that

$$\mathrm{rect}[x] \triangleq \begin{cases} 1, & |x| < \frac{1}{2} \\ 0, & |x| \geqslant \frac{1}{2} \end{cases}. \tag{1.31}$$

In the above formulas, the quantity L/Δ is the transverse contact ratio which, from Eq. (148) of Reference 5, we see can be expressed in terms of fundamental design parameters by

$$\frac{L}{\Delta} = \frac{DN^{(\bullet)}\csc\phi}{2\pi R_b^{(\bullet)}}, \tag{1.32}$$

where, as before, D, $N^{(\cdot)}$, ϕ, and $R_b^{(\cdot)}$ are, respectively, the active depth of the teeth, the number of teeth on gear $(\cdot)$, the pressure angle, and the base circle radius of gear $(\cdot)$.

Use of the above formulas is illustrated on pp. 1774 through 1780 of Reference 5. A discussion of the general properties of the excitation spectra of spur and helical gears may be found on pp. 1781 through 1785 of that same reference.

THE EQUATIONS OF MOTION

We turn now to writing the system equations of motion in a form useful for computing the desired response metrics from the excitation characterization described in the preceding section. The system of interest is the "four-square" gear fatigue test apparatus located at the NASA Lewis Research Center. A schematic diagram of this system is shown in Fig. 1. The system contains two test gears and two slave gears as shown. The lightweight test gears are connected to the relatively massive slave gears by short very stiff shafts. Torque is applied between the shafting and one of the slave gears using a pressurized-oil torque-applier. There is no accumulator associated with the torque applier. The system is firmly supported.

A displacement type of excitation takes place at each of the two meshes I and II. Because of the relatively large stiffnesses of shafting, gear bodies, and bearing support structure we shall assume that the (displacement) excitation at the meshing points is "taken up" by tooth elastic deformations and relative motion between the shafting and slave gear at the fluid loaded torque applier. That is, shafting, gear bodies, and bearing supports shall be modeled as rigid members with gear bodies and shafting possessing inertia. Gear teeth shall be modeled as elastic members. The torque applier shall be assumed to apply constant torque τ_a plus a dissipation torque $c_a(\dot{\theta}_3-\dot{\theta}_2)$ proportional to the angular velocity difference between the slave gear and its shafting. Thus, the system is assumed to have three degrees of freedom, θ_1, θ_2, and θ_3 as shown in Fig. 1. Since some vibratory energy associated with motions θ_1 and θ_2 is necessarily dissipated in the bearings, viscous damping terms are directly associated with these two degrees of freedom. For completeness, a viscous damping term also will be associated with θ_3.

Because bearing supports are assumed to be rigid, each gear must move in pure (generally unsteady) rotation. Thus, the instantaneous forces W_I and W_{II} transmitted by meshes I and II must have equal and opposite reactions at the bearing supports as illustrated by the test gear supports in Fig. 1. Since we are dealing with gears of nominal involute design, the *directions* of mesh forces W_I and W_{II}, and their bearing reactions, remain fixed and parallel to their respective planes of contact. However, the magnitudes of these forces generally will possess temporal variations.

All gears in the system have the same base circle radius R, which is the radius instrumental in generation of the gear torques by forces W_I and W_{II}. I_1 designates the moment of inertia of the left-hand slave/test gear pair and shafting whose angular position

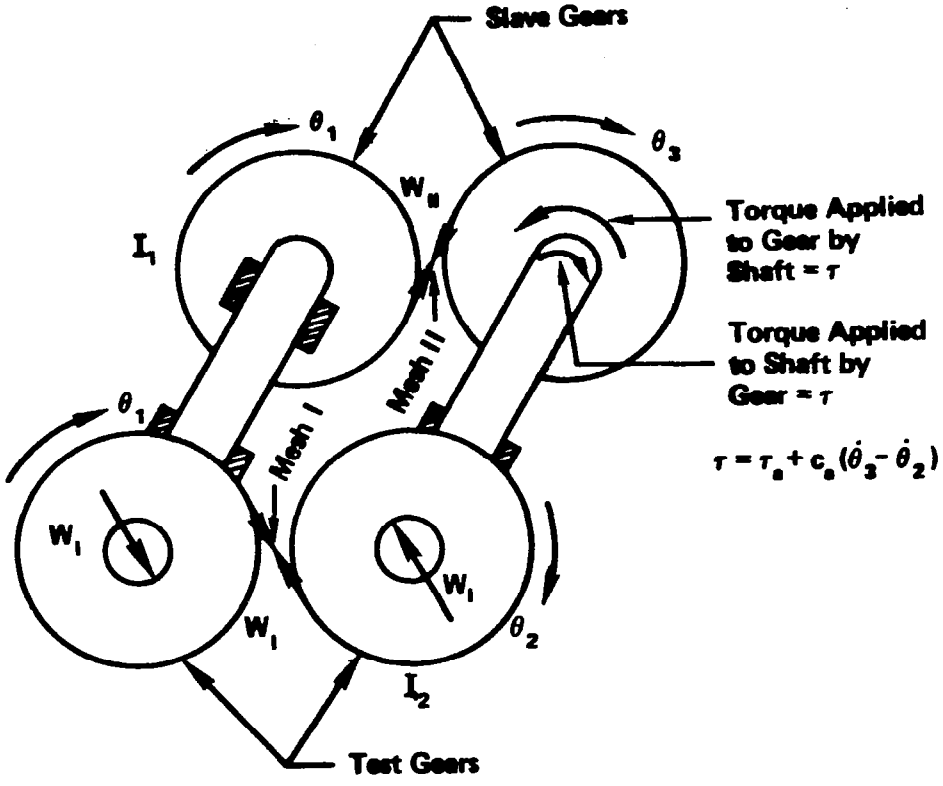

FIG. 1. SCHEMATIC OF NASA LEWIS GEAR FATIGUE TEST APPARATUS.

is θ_1. I_2 designates the moment of inertia of the test gear and shafting whose angular position is θ_2, and I_3 designates the moment of inertia of the slave gear whose angular position is θ_3. Dissipation (dashpot) constants c_1, c_2, and c_3 are associated with θ_1, θ_2, and θ_3 respectively.

Thus, the differential equations of motion of the three rotational elements are

$$I_1\ddot{\theta}_1 + c_1\dot{\theta}_1 = RW_{II} - RW_I = R(W_{II}-W_I) \tag{2.1}$$

$$I_2\ddot{\theta}_2 + c_2\dot{\theta}_2 = -RW_I + \tau_a + c_a(\dot{\theta}_3-\dot{\theta}_2) \tag{2.2}$$

$$I_3\ddot{\theta}_3 + c_3\dot{\theta}_3 = RW_{II} - \tau_a - c_a(\dot{\theta}_3-\dot{\theta}_2)\ . \tag{2.3}$$

The moments of inertia I_1, I_2, and I_3, radii R, applied torque τ_a, and dissipation constants c_1, c_2, c_3, and c_a all are assumed to be independent of time, whereas, angular positions θ_1, θ_2, and θ_3 and forces W_I and W_{II}, are assumed to be generally time dependent. Angular positions θ_1, θ_2, and θ_3 are the *vibratory components* of the true angular positions of the gears.

Let us now relate the instantaneous mesh forces W_I and W_{II} to the transmission errors of the appropriate gear pairs and the angular positions θ of the gears. The transmission error is measured in the axial plane in a direction parallel to the plane of contact of the gear teeth, and is defined as positive when it is "equivalent" to removal of material from the tooth surfaces [p. 1410 of Reference 4]. Thus, if we denote the (dynamic) transmission error of meshes I and II by ζ_I and ζ_{II} respectively, then for the teeth to be in continuous contact we require the following two compatibility relations to be satisfied [p. 1410 of Reference 4] as may be seen from Fig. 1:

$$R\theta_1 + R\theta_2 = \zeta_I \tag{2.4}$$

$$-R\theta_1 - R\theta_3 = \zeta_{II}. \tag{2.5}$$

Let ζ_D denote the (dynamic) transmission error ζ_I or ζ_{II} associated with either of the two meshes illustrated in Fig. 1, and let C_T denote the total compliance of the teeth in the same mesh. C_T varies periodically with time due to variations in tooth-pair stiffness and the numbers of teeth in contact. Let W denote the

force transmitted by the mesh which also can vary with time. Then ζ_D can be expressed [p. 1410 of Reference 4] as

$$\zeta_D = C_T W + \zeta^{(1)} + \zeta^{(2)} \tag{2.6}$$

where $\zeta^{(1)}$ and $\zeta^{(2)}$ each denotes the component of the transmission error from one gear in the mesh due to *geometric* deviations of the active tooth surfaces from perfect involute surfaces [p. 1410 of Reference 4]. The average value of $\zeta^{(1)}$ and $\zeta^{(2)}$, where each value is an average over all teeth on the appropriate gear (1) or (2), yields the mean transmission error components $\zeta_m^{(1)}$ and $\zeta_m^{(2)}$ contained earlier in Eq. (1.3) and described in Reference 4.

To enable us to use a transfer function approach to effect a solution to the gear system dynamic problem, let us now decompose C_T and W into their time average components $\overline{C}_T$ and W_0, and their fluctuating components δC_T and δW — i.e.,

$$C_T = \overline{C}_T + \delta C_T \tag{2.7}$$

$$W = W_0 + \delta W. \tag{2.8}$$

We then have

$$C_T W = \overline{C}_T W + \delta C_T W_0 + \delta C_T \delta W \tag{2.9a}$$

$$\approx \overline{C}_T W + W_0 \delta C_T , \tag{2.9b}$$

where, in the second line, we have neglected the product $\delta C_T \delta W$ of fluctuating quantities. If we now define a loading dependent component of the *static* transmission error as

$$\zeta'_{W_0} \triangleq W_0 \delta C_T , \tag{2.10}$$

we see that since $(1/K) \equiv C_T$, this definition is the same as that of $\zeta_W(x)_0$ in Eq. (1.3) whose Fourier coefficients are given by Eq. (1.8) — except that the dc component $W_0 \overline{C}_T$ of $\zeta_W(x)_0$ described by the term n = 0 in Eq. (1.8) is *not* included in the definition, Eq. (2.10). Using the approximation given by Eq. (2.9), we may now combine Eqs. (2.6), (2.9), and (2.10) to give

$$\zeta_D \approx \bar{C}_T W + \zeta'_{W_0} + \zeta^{(1)} + \zeta^{(2)}$$

$$\equiv \bar{C}_T W + \zeta' \ , \qquad (2.11)$$

where in the second line we have defined

$$\zeta' \triangleq \zeta'_{W_0} + \zeta^{(1)} + \zeta^{(2)} \ , \qquad (2.12)$$

which is the static transmission error discussed in the first section of this report *except for the dc component* $W_0\bar{C}_T$ *not included in Eq. (2.12).* Equation (2.11) provides an approximate relationship between the dynamic and static transmission errors that would be exact if the product $\delta C_T \delta W$ were added to its right-hand side.

Using the approximation given by Eq. (2.11), we therefore can express the dynamic transmission errors of each of the two meshes illustrated in Fig. 1 by

$$\zeta_I \approx \bar{C}_I W_I + \zeta'_I \qquad (2.13)$$

and

$$\zeta_{II} \approx \bar{C}_{II} W_{II} + \zeta'_{II} \ , \qquad (2.14)$$

where $\bar{C}_I$ and $\bar{C}_{II}$ denote respectively the time-average values of the compliances C_I and C_{II} of meshes I and II, W_I and W_{II} denote the time-varying forces transmitted by these meshes, and ζ'_I and ζ'_{II} denote the static transmission errors of these meshes as defined by Eq. (2.12). Combining Eqs. (2.4) and (2.13), and then Eqs. (2.5) and (2.14), gives

$$R(\theta_1+\theta_2) = \bar{C}_I W_I + \zeta'_I \qquad (2.15)$$

and

$$-R(\theta_1+\theta_3) = \bar{C}_{II} W_{II} + \zeta'_{II} \ , \qquad (2.16)$$

which we can solve algebraically for W_I and W_{II} to give

$$W_I = (\bar{C}_I)^{-1}[R(\theta_1+\theta_2)-\zeta'_I] \qquad (2.17)$$

and

$$W_{II} = -(\bar{C}_{II})^{-1}[R(\theta_1+\theta_3)+\zeta'_{II}]. \tag{2.18}$$

Mesh forces W_I and W_{II}, system displacements θ_1, θ_2, and θ_3, and transmission errors ζ'_I and ζ'_{II} in Eqs. (2.17) and (2.18) are all assumed to be time-varying quantities. Finally, by substituting the expressions for W_I and W_{II} given by Eqs. (2.17) and (2.18) into Eqs. (2.1) through (2.3), we obtain after minor rearrangements

$$I_1\ddot{\theta}_1+c_1\dot{\theta}_1+R^2[(\bar{C}_I)^{-1}+(\bar{C}_{II})^{-1}]\theta_1+R^2(\bar{C}_I)^{-1}\theta_2$$

$$+R^2(\bar{C}_{II})^{-1}\theta_3 = R(\bar{C}_I)^{-1}\zeta'_I-R(\bar{C}_{II})^{-1}\zeta'_{II} \tag{2.19}$$

$$R^2(\bar{C}_I)^{-1}\theta_1+I_2\ddot{\theta}_2+(c_2+c_a)\dot{\theta}_2+R^2(\bar{C}_I)^{-1}\theta_2-c_a\dot{\theta}_3$$

$$= \tau_a+R(\bar{C}_I)^{-1}\zeta'_I \tag{2.20}$$

$$R^2(\bar{C}_{II})^{-1}\theta_1-c_a\dot{\theta}_2+I_3\ddot{\theta}_3+(c_3+c_a)\dot{\theta}_3+R^2(\bar{C}_{II})^{-1}\theta_3$$

$$= -\tau_a-R(\bar{C}_{II})^{-1}\zeta'_{II} \quad . \tag{2.21}$$

Equations (2.19) through (2.21) are the desired differential equations of motion for the system (displacement) responses θ_1, θ_2, and θ_3 with the (time-varying) static transmission errors ζ'_I and ζ'_{II} of meshes I and II as the excitation. ζ'_I and ζ'_{II} are defined by Eqs. (2.12) and (2.10), and may be written explicitly as

$$\zeta'_I = (\tau_a/R)\delta C_I + \zeta_I^{(1)} + \zeta_I^{(2)} \tag{2.22}$$

and

$$\zeta'_{II} = (\tau_a/R)\delta C_{II} + \zeta_{II}^{(1)} + \zeta_{II}^{(3)} \quad , \tag{2.23}$$

where τ_a/R is the time-average force W_0 transmitted by the two meshes, δC_I and δC_{II} are, respectively, the fluctuating components δC_T of the compliances of meshes I and II, $\zeta_I^{(1)}$ and $\zeta_I^{(2)}$ are the geometric

components of the transmission errors of gears (1) and (2) of mesh I, and $\zeta_{II}^{(1)}$ and $\zeta_{II}^{(3)}$ are the geometric components of the transmission errors of gears (1) and (3) of mesh II. See Fig. 1. The derivation of Eqs. (2.19) through (2.21) illustrates a specific application of the general methodology described on p. 1410 of Reference 4.

Solution Using Transfer Functions

We shall now solve the set of Equations (2.17) through (2.21) to yield algebraic expressions for the Fourier transforms of the time-dependent mesh forces W_I and W_{II} in terms of the Fourier transforms of the static transmission errors ζ_I' and ζ_{II}' (or, equivalently, their Fourier series coefficients). We shall begin by taking the Fourier transforms of each of the five Equations (2.17) through (2.21). In general, we denote the Fourier transform of a variable by placing caret over that variable — e.g., for $\theta_1(t)$, $\theta_2(t)$, or $\theta_3(t)$, we define

$$\hat{\theta}(\omega) \triangleq \int_{-\infty}^{\infty} \theta(t) e^{-i\omega t}\, dt \,, \tag{2.24}$$

for $W_I(t)$ and $W_{II}(t)$, we define

$$\hat{W}(\omega) \triangleq \int_{-\infty}^{\infty} W(t) e^{-i\omega t}\, dt \,, \tag{2.25}$$

for $\zeta_I'(t)$ and $\zeta_{II}'(t)$, we define

$$\hat{\zeta}'(\omega) \triangleq \int_{-\infty}^{\infty} \zeta'(t) e^{-i\omega t}\, dt \,, \tag{2.26}$$

and, finally, for our applied dc torque τ_a, we define

$$\hat{\tau}_a(\omega) \triangleq \int_{-\infty}^{\infty} \tau_a e^{-i\omega t}\, dt. \tag{2.27}$$

The Fourier mates to Eqs. (2.24) through (2.27) are

$$\theta(t) = \frac{1}{2\pi} \int_{-\infty}^{\infty} \hat{\theta}(\omega) e^{i\omega t}\, d\omega \tag{2.28}$$

$$W(t) = \frac{1}{2\pi} \int_{-\infty}^{\infty} \hat{W}(\omega) e^{i\omega t}\, d\omega \tag{2.29}$$

$$\zeta'(t) = \frac{1}{2\pi}\int_{-\infty}^{\infty} \hat{\zeta}'(\omega)\, e^{i\omega t}\, d\omega \tag{2.30}$$

and

$$\tau_a = \frac{1}{2\pi}\int_{-\infty}^{\infty} \hat{\tau}_a(\omega) e^{i\omega t}\, d\omega, \tag{2.31}$$

where, from this last relation, we may conclude that

$$\hat{\tau}_a(\omega) = 2\pi\tau_a\delta(\omega) \tag{2.32}$$

since τ_a is a constant torque. In Eq. (2.32), $\delta(\omega)$ denotes the Dirac delta function, which is zero everywhere except at $\omega = 0$, and whose integral over ω is unity. From Eq. (2.28), we may also conclude that

$$\dot{\theta}(t) = \frac{1}{2\pi}\int_{-\infty}^{\infty} i\omega\hat{\theta}(\omega)e^{i\omega t}\, d\omega \tag{2.33}$$

and

$$\ddot{\theta}(t) = \frac{1}{2\pi}\int_{-\infty}^{\infty} -\omega^2\hat{\theta}(\omega)e^{i\omega t}\, d\omega, \tag{2.34}$$

from which it follows that $i\omega\hat{\theta}(\omega)$ and $-\omega^2\hat{\theta}(\omega)$ are, respectively, the Fourier transforms of $\dot{\theta}(t)$ and $\ddot{\theta}(t)$.

Utilizing Eqs. (2.24), (2.26), (2.27), (2.33), and (2.34), we may now write the Fourier transforms of Eqs. (2.19) through (2.21) as

$$\left\{-I_1\omega^2+ic_1\omega+R^2[(\bar{C}_I)^{-1}+(\bar{C}_{II})^{-1}]\right\}\hat{\theta}_1+R^2(\bar{C}_I)^{-1}\hat{\theta}_2$$

$$+ R^2(\bar{C}_{II})^{-1}\hat{\theta}_3 = R(\bar{C}_I)^{-1}\hat{\zeta}_I'-R(\bar{C}_{II})^{-1}\hat{\zeta}_{II}' \tag{2.35}$$

$$R^2(\bar{C}_I)^{-1}\hat{\theta}_1+[-I_2\omega^2+i(c_2+c_a)\omega+R^2(\bar{C}_I)^{-1}]\hat{\theta}_2$$

$$-ic_a\omega\hat{\theta}_3 = \hat{\tau}_a + R(\bar{C}_I)^{-1}\hat{\zeta}_I' \tag{2.36}$$

and

$$R^2(\bar{C}_{II})^{-1}\hat{\theta}_1 - ic_a\omega\hat{\theta}_2+[-I_3\omega^2+i(c_3+c_a)\omega+R^2(\bar{C}_{II})^{-1}]\hat{\theta}_3$$

$$= -\hat{\tau}_a - R(\bar{C}_{II})^{-1}\hat{\zeta}_{II}'. \tag{2.37}$$

Equations (2.35) through (2.37) are a set of linear algebraic equations for the Fourier transforms of the responses θ_1, θ_2, and θ_3 in terms of the Fourier transforms of the excitations τ_a, ζ_I' and ζ_{II}'. Let us define $H_{ij}(\omega)$ as the response $\hat{\theta}_i$ due to unit excitation $\hat{\zeta}_j' = 1$, where i = 1,2, or 3 and j = I or II. Then for $\omega \neq 0$, the set of Equations (2.35) through (2.37) can be written in matrix form,

$$[A_{ij}(\omega)]\,[H_{ij}(\omega)] = [U_{ij}(\omega)]\,, \qquad \omega \neq 0 \tag{2.38}$$

where the condition $\omega \neq 0$ arises from the fact that $\hat{\tau}_a(\omega)$ has a component only at $\omega = 0$. From Eqs. (2.35) through (2.37), we see that $[A_{ij}(\omega)]$ is a symmetric square matrix with elements

$$\begin{aligned}
A_{11} &= -I_1\omega^2+ic_1\omega+R^2[(\bar{C}_I)^{-1}+(\bar{C}_{II})^{-1}]\\
A_{12} &= R^2(\bar{C}_I)^{-1}\\
A_{13} &= R^2(\bar{C}_{II})^{-1}\\
A_{21} &= A_{12}\\
A_{22} &= -I_2\omega^2+i(c_2+c_a)\omega+R^2(\bar{C}_I)^{-1}\\
A_{23} &= -ic_a\omega\\
A_{31} &= A_{13}\\
A_{32} &= A_{23}\\
A_{33} &= -I_3\omega^2+i(c_3+c_a)\omega+R^2(\bar{C}_{II})^{-1},
\end{aligned} \tag{2.39}$$

whereas the excitation matrix $[U_{ij}(\omega)]$ can be written as

$$[U_{ij}(\omega)] = \begin{bmatrix} R(\bar{C}_I)^{-1} & -R(\bar{C}_{II})^{-1} \\ R(\bar{C}_I)^{-1} & 0 \\ 0 & -R(\bar{C}_{II})^{-1} \end{bmatrix}. \tag{2.40}$$

We wish now to express the Fourier transforms of the mesh forces W_I and W_{II} in terms of the solutions $H_{ij}(\omega)$ of the matrix Eq. (2.38). Forming the Fourier transforms of Eqs. (2.17) and (2.18) and using the definitions, Eqs. (2.24) through (2.26), we have

$$\hat{W}_I = (\bar{C}_I)^{-1}\left[R(\hat{\theta}_1+\hat{\theta}_2)-\hat{\zeta}'_I\right] \tag{2.41}$$

and

$$\hat{W}_{II} = -(\bar{C}_{II})^{-1}\left[R(\hat{\theta}_1+\hat{\theta}_3)+\hat{\zeta}'_{II}\right]. \tag{2.42}$$

Recognizing that $H_{1I}(\omega)$ and $H_{2I}(\omega)$ are the responses $\hat{\theta}_1(\omega)$ and $\hat{\theta}_2(\omega)$ to a unit input $\hat{\zeta}'_I(\omega) = 1$ at mesh I, and that $H_{1II}(\omega)$ and $H_{2II}(\omega)$ are the responses $\hat{\theta}_1(\omega)$ and $\hat{\theta}_2(\omega)$ to a unit input $\hat{\zeta}'_{II}(\omega) = 1$ at mesh II, it follows from the linearity of the system of Eqs. (2.35) through (2.37) and the definitions of $H_{ij}(\omega)$, $i = 1$ and 2 and $j = I$ and II that from Eq. (2.41) we have for the Fourier transform of $W_I(t)$,

$$\hat{W}_I = (\bar{C}_I)^{-1}\Big(\{R[H_{1I}(\omega)+H_{2I}(\omega)]-1\}\hat{\zeta}'_I + R[H_{1II}(\omega)+H_{2II}(\omega)]\hat{\zeta}'_{II}\Big),\ \omega \neq 0. \tag{2.43}$$

Similarly, we may express $\hat{W}_{II}$ as

$$\hat{W}_{II} = -(\bar{C}_{II})^{-1}\Big(R[H_{1I}(\omega)+H_{3I}(\omega)]\hat{\zeta}'_I + \{R[H_{1II}(\omega)+H_{3II}(\omega)]+1\}\hat{\zeta}'_{II}\Big),\quad \omega \neq 0. \tag{2.44}$$

Equations (2.43) and (2.44) are valid for all ω except $\omega = 0$. Since our central interest is the force history in mesh I, we shall evaluate from here on only the Fourier transform $\hat{W}_I$ of that force history. From Eq. (2.43), we see that once $H_{1I}(\omega)$, $H_{2I}(\omega)$, $H_{1II}(\omega)$, and $H_{2II}(\omega)$ are evaluated, the computation of $\hat{W}_I(\omega)$ from $\hat{\zeta}'_I(\omega)$ and $\hat{\zeta}'_{II}(\omega)$ is a very simple matter.

Evaluation of Transfer Functions

Let us now proceed to evaluate the transfer functions $H_{ij}(\omega)$, $i = 1$ and 2, $j = I$ and II, which are solutions to the matrix equations defined by Eqs. (2.38) through (2.40). Using Cramer's rule [e.g., p. 12 of Reference 7], we recognize that any of the required $H_{ij}(\omega)$ can be expressed as

$$H_{ij}(\omega) = \frac{N_{ij}(\omega)}{D(\omega)} , \tag{2.45}$$

where $D(\omega)$ is the determinant of the coefficient matrix $[A_{ij}(\omega)]$ whose elements are given by Eq. (2.39). The determinant $D(\omega)$ is readily evaluated to give

$$D(\omega) \triangleq |A_{ij}| = \begin{vmatrix} A_{11} & A_{12} & A_{13} \\ A_{21} & A_{22} & A_{23} \\ A_{31} & A_{32} & A_{33} \end{vmatrix} \tag{2.46a}$$

$$= A_{11}(A_{22}A_{33}-A_{23}A_{32}) - A_{21}(A_{12}A_{33}-A_{13}A_{32}) + A_{31}(A_{12}A_{23}-A_{13}A_{22}) \tag{2.46b}$$

$$= A_{11}(A_{22}A_{33}-A_{23}^2) - A_{12}(A_{12}A_{33}-A_{13}A_{23}) + A_{13}(A_{12}A_{23}-A_{13}A_{22}) , \tag{2.46c}$$

where we have used the symmetry property $A_{ij} = A_{ji}$ in writing this last expression. Using Cramer's rule, it follows from Eqs. (2.38) and (2.40) that we may express $N_{1I}(\omega)$ as the determinant

$$N_{1I}(\omega) \triangleq \begin{vmatrix} R(\bar{C}_I)^{-1} & A_{12} & A_{13} \\ R(\bar{C}_I)^{-1} & A_{22} & A_{23} \\ 0 & A_{32} & A_{33} \end{vmatrix} \tag{2.47a}$$

$$= R(\bar{C}_I)^{-1}[(A_{22}A_{33}-A_{23}A_{32})-(A_{12}A_{33}-A_{13}A_{32})]$$

$$= R(\bar{C}_I)^{-1}[A_{33}(A_{22}-A_{12})+A_{32}(A_{13}-A_{23})] \tag{2.47b}$$

$$= R(\bar{C}_I)^{-1}[A_{33}(A_{22}-A_{12})+A_{23}(A_{13}-A_{23})], \tag{2.47c}$$

where we have again used $A_{ij} = A_{ji}$ in writing the last line. Similarly, we have

$$N_{2I}(\omega) \triangleq \begin{vmatrix} A_{11} & R(\bar{C}_I)^{-1} & A_{13} \\ A_{21} & R(\bar{C}_I)^{-1} & A_{23} \\ A_{31} & 0 & A_{33} \end{vmatrix} \tag{2.48a}$$

$$= R(\bar{C}_I)^{-1}[A_{33}(A_{11}-A_{21})+A_{31}(A_{23}-A_{13})] \tag{2.48b}$$

$$= R(\bar{C}_I)^{-1}[A_{33}(A_{11}-A_{12})+A_{13}(A_{23}-A_{13})], \tag{2.48c}$$

$$N_{1II}(\omega) \triangleq \begin{vmatrix} -R(\bar{C}_{II})^{-1}A_{12} & A_{13} \\ 0 \quad A_{22} & A_{23} \\ -R(\bar{C}_{II})^{-1}A_{32} & A_{33} \end{vmatrix} \tag{2.49a}$$

$$= R(\bar{C}_{II})^{-1}[A_{22}(A_{13}-A_{33})+A_{23}(A_{32}-A_{12})] \tag{2.49b}$$

$$= R(\bar{C}_{II})^{-1}[A_{22}(A_{13}-A_{33})+A_{23}(A_{23}-A_{12})], \tag{2.49c}$$

and

$$N_{2II}(\omega) = \begin{vmatrix} A_{11} & -R(\bar{C}_{II})^{-1} & A_{13} \\ A_{21} & 0 & A_{23} \\ A_{31} & -R(\bar{C}_{II})^{-1} & A_{33} \end{vmatrix} \tag{2.50a}$$

$$= R(\bar{C}_{II})^{-1}[A_{21}(A_{33}-A_{13})+A_{23}(A_{11}-A_{31})] \tag{2.50b}$$

$$= R(\bar{C}_{II})^{-1}[A_{12}(A_{33}-A_{13})+A_{23}(A_{11}-A_{13})]. \tag{2.50c}$$

The symmetry property $A_{ij} = A_{ji}$ has *not* been used in the "a and b" versions of Eqs. (2.46) through (2.50); however, this symmetry property has been used in the "c" version of Eqs. (2.46) through (2.50).

From Eq. (2.43), we see that we require the sums $H_{1I}(\omega) + H_{2I}(\omega)$ and $H_{1II}(\omega) + H_{2II}(\omega)$. According to Eq.(2.45), we can express these sums as

$$H_{1I}(\omega) + H_{2I}(\omega) = \frac{N_{1I}(\omega)+N_{2I}(\omega)}{D(\omega)} \tag{2.51}$$

and

$$H_{1II}(\omega) + H_{2II}(\omega) = \frac{N_{1II}(\omega)+N_{2II}(\omega)}{D(\omega)} \, . \tag{2.52}$$

From Eqs. (2.47) and (2.48), it follows that the numerator in Eq. (2.51) can be expressed as

$$N_{1I} + N_{2I} = R(\bar{C}_I)^{-1}[A_{33}(A_{11}+A_{22}-A_{12}-A_{21}) + (A_{13}-A_{23})(A_{32}-A_{31})] \tag{2.53a}$$

$$= R(\bar{C}_I)^{-1}[A_{33}(A_{11}+A_{22}-2A_{12})-(A_{13}-A_{23})^2], \tag{2.53b}$$

where $A_{ij} = A_{ji}$ has been used in the second line, but not in the first line. In an analogous manner, we have from Eqs. (2.49) and (2.50)

$$N_{1II}+N_{2II} = R(\bar{C}_{II})^{-1}[A_{23}(A_{11}+A_{32}-A_{12}-A_{31}) - (A_{33}-A_{13})(A_{22}-A_{21})] \tag{2.54a}$$

$$= R(\bar{C}_{II})^{-1}[A_{23}(A_{11}+A_{23}-A_{12}-A_{13}) - (A_{33}-A_{13})(A_{22}-A_{12})], \tag{2.54b}$$

where $A_{ij} = A_{ji}$ has again been used in obtaining Eq. (2.54b) from Eq. (2.54a).

Equations (2.46c), (2.53b), and (2.54b) are the relations required for evaluation of the sums $H_{1I}(\omega) + H_{2I}(\omega)$ and $H_{1II}(\omega) + H_{2II}(\omega)$, using Eqs. (2.51) and (2.52), for substitution into Eq. (2.43). The coefficients A_{ij} are given by Eq. (2.39). The results of these straightforward but tedious algebraic manipulations are

$$\begin{aligned} N_{1I}(\omega) + N_{2I}(\omega) = R(\bar{C}_I)^{-1}\Big(& (I_1+I_2)I_3\omega^4 \\ & - [(I_1+I_2+I_3)R^2(\bar{C}_{II})^{-1}+(c_1+c_2+c_3)c_a+(c_1+c_2)c_3]\omega^2 \\ & + i\{-[(I_1+I_2)(c_3+c_a)+I_3(c_1+c_2+c_a)]\omega^3 \\ & +(c_1+c_2+c_3)R^2(\bar{C}_{II})^{-1}\omega\}\Big) \, , \end{aligned} \tag{2.55}$$

$$N_{1II}(\omega) + N_{2II}(\omega) = R(\bar{C}_{II})^{-1}\Big\{-I_2 I_3\omega^4 + [(c_1+c_2+c_3)c_a+c_2c_3]\omega^2 + i[(I_1+I_2+I_3)c_a+I_2c_3+I_3c_2]\omega^3\Big\}\ , \tag{2.56}$$

and

$$\begin{aligned} D(\omega) = {} & -I_1I_2I_3\omega^6+\{I_1I_2R^2(\bar{C}_{II})^{-1}+I_1I_3R^2(\bar{C}_I)^{-1} \\ & +I_2I_3R^2[(\bar{C}_I)^{-1}+(\bar{C}_{II})^{-1}]+I_1(c_2c_3+c_2c_a+c_3c_a) \\ & +I_2c_1(c_3+c_a)+I_3c_1(c_2+c_a)\}\omega^4 \\ & -\{(I_1+I_2+I_3)R^4(\bar{C}_I)^{-1}(\bar{C}_{II})^{-1}+c_1(c_2+c_a)R^2(\bar{C}_{II})^{-1} \\ & +c_1(c_3+c_a)R^2(\bar{C}_I)^{-1}+[(c_2c_3+c_2c_a+c_3c_a)]R^2[(\bar{C}_I)^{-1}+(\bar{C}_{II})^{-1}]\}\omega^2 \\ & +i\Big([I_1I_2(c_3+c_a)+I_1I_3(c_2+c_a)+I_2I_3c_1]\omega^5 \\ & -\{I_1[(c_2+c_a)R^2(\bar{C}_{II})^{-1}+(c_3+c_a)R^2(\bar{C}_I)^{-1}] \\ & +I_2[c_1R^2(\bar{C}_{II})^{-1}+(c_3+c_a)R^2(\bar{C}_I^{-1}+\bar{C}_{II}^{-1})] \\ & +I_3[c_1R^2(\bar{C}_I)^{-1}+(c_2+c_a)R^2(\bar{C}_I^{-1}+\bar{C}_{II}^{-1})] \\ & +c_1(c_2c_3+c_2c_a+c_3c_a)\}\omega^3 \\ & +[(c_1+c_2+c_3)R^4(\bar{C}_I)^{-1}(\bar{C}_{II})^{-1}]\omega\Big)\ . \end{aligned} \tag{2.57}$$

Low and High Frequency Asymptotic Behavior

Returning to the expression for $\hat{W}_I$ given by Eq. (2.43), let us define

$$Q_{I\,I}(\omega) \triangleq R[H_{1I}(\omega)+H_{2I}(\omega)]-1 \tag{2.58}$$

and

$$Q_{I\,II}(\omega) \triangleq R[H_{1II}(\omega)+H_{2II}(\omega)] \tag{2.59}$$

which enable us to express $\hat{W}_I$ as

$$\hat{W}_I = (\bar{C}_I)^{-1}[Q_{II}(\omega)\hat{\zeta}_I'+Q_{I\,II}(\omega)\hat{\zeta}_{II}'],\ \omega \neq 0\ . \tag{2.60}$$

Since $\bar{C}_I\hat{W}_I$, $\hat{\zeta}'_I$, and $\hat{\zeta}'_{II}$ is each the Fourier transform of a displacement, we see from Eq. (2.60) that $Q_{II}(\omega)$ and $Q_{I\,II}(\omega)$ is each a dimensionless transfer function. In general, $Q_{ij}(\omega)$ represents the contribution to the complex displacement amplitude $\bar{C}_i\hat{W}_i$ from a unit sinusoidal transmission error amplitude $\hat{\zeta}'_j = 1$. An equation comparable to Eq. (2.60) can, of course, be written to replace and interpret Eq. (2.44).

It is instructive to examine the low and high frequency asymptotic behavior of the two transfer functions $Q_{II}(\omega)$ and $Q_{I\,II}(\omega)$ in Eq. (2.60). Let us consider first the low frequency behavior of $Q_{II}(\omega)$. Substituting Eq. (2.51) into Eq. (2.58) gives after minor rearrangement

$$Q_{II}(\omega) = \frac{R[N_{1I}(\omega)+N_{2I}(\omega)]-D(\omega)}{D(\omega)} \quad . \tag{2.61}$$

Retaining terms proportional to ω and ω^2 in $N_{1I}(\omega) + N_{2I}(\omega)$ and in $D(\omega)$ in the numerator of Eq. (2.61), and retaining the term proportional to ω in the denominator $D(\omega)$ of Eq. (2.61), we find that the terms proportional to ω in the numerator vanish identically leaving for our final asymptotic result as $\omega \to 0$,

$$Q_{II}(\omega) \sim -i\left[c_a+\frac{c_1c_2+c_2c_3}{c_1+c_2+c_3}\right]\frac{\omega}{R^2(\bar{C}_I)^{-1}} \quad , \ \omega \to 0 \tag{2.62}$$

which gives the low frequency asymptotic behavior of the transfer function $Q_{II}(\omega)$. Notice from Eq. (2.62) that $Q_{II}(\omega) \to 0$ as $\omega \to 0$, and that the strength of every term in Eq. (2.62) depends fundamentally on one or more of the system damping constants c_1, c_2, c_3 or c_a.

Turning now to the high-frequency asymptotic behavior of $Q_{II}(\omega)$, we have by retaining only the term proportional to ω^6 in $D(\omega)$ and the term proportional to ω^4 in $N_{1I}(\omega) + N_{2I}(\omega)$ in Eqs. (2.57) and (2.55) respectively as $\omega \to \infty$,

$$H_{1I}+H_{2I} \sim -\frac{R(\bar{C}_I)^{-1}(I_1+I_2)}{I_1I_2\omega^2} \tag{2.63}$$

where we have again used Eq. (2.51). From Eq. (2.58), we see that the asymptotic high frequency behavior of $Q_{II}(\omega)$ therefore can be expressed as

$$Q_{II}(\omega) \sim -\left[1+\frac{R^2(\bar{C}_I)^{-1}(I_1+I_2)}{I_1 I_2 \omega^2}\right], \quad \omega \to \infty \ . \tag{2.64}$$

Thus, as $\omega\to\infty$, the magnitude of the transfer function $Q_{II}(\omega)$ approaches unity. Moreover, for large enough ω, the deviation of $Q_{II}(\omega)$ from -1 is independent of system damping and, in our case, depends primarily on $R^2(\bar{C}_I)^{-1}/I_2$ since $I_1 >> I_2$. *Hence, referring to Eq. (2.60), we see that as $\omega\to 0$, no dynamic forces arise in the test gear mesh I from the static transmission error $\hat{\zeta}_I'$ of that same mesh, whereas as $\omega\to\infty$, the inertias I_1 and I_2 prevent all vibratory motion of degrees of freedom θ_1 and θ_2 in the test rig shown in Fig. 1 resulting in "full transfer" of the static transmission error $\hat{\zeta}_I'$ to dynamic forces in mesh I.*

Let us turn now to the transfer function $Q_{I\ II}(\omega)$ which controls the forces generated in mesh I by the static transmission error in mesh II. To examine the asymptotic low frequency behavior of $Q_{I\ II}(\omega)$, we retain the term proportional to ω in $D(\omega)$ as given by Eq. (2.57) and the term proportional to ω^2 in $N_{1II}(\omega) + N_{2II}(\omega)$ as given by Eq. (2.56). According to Eqs. (2.52) and (2.59), the retention of these two terms gives as $\omega\to 0$,

$$Q_{I\ II}(\omega) \sim \frac{R^2(\bar{C}_{II})^{-1}[(c_1+c_2+c_3)c_a+c_2c_3]\omega^2}{i(c_1+c_2+c_3)R^4(\bar{C}_I)^{-1}(\bar{C}_{II})^{-1}\omega}$$

$$= -i\left[c_a+\frac{c_2c_3}{c_1+c_2+c_3}\right]\frac{\omega}{R^2(\bar{C}_I)^{-1}}, \quad \omega \to 0 \ . \tag{2.65}$$

Thus, as $\omega\to 0$, $Q_{I\ II}(\omega)$ also tends to zero as did $Q_{II}(\omega)$. Moreover, the right-hand side of Eq. (2.65) depends fundamentally on the system damping constants c_1, c_2, c_3, and c_a, and is very similar to the right-hand side of Eq. (2.62) which governs the behavior of $Q_{II}(\omega)$ as $\omega\to 0$. For $c_3=0$, the second term in the right-hand side of Eq. (2.65) vanishes.

To study the high frequency asymptotic behavior of $Q_{I\ II}(\omega)$, we retain the term proportional to ω^6 in $D(\omega)$ and the term proportional to ω^4 in $N_{1II}(\omega) + N_{2II}(\omega)$. According to Eqs. (2.52), (2.56), (2.57), and (2.59), we then have for the asymptotic behavior of $Q_{I\ II}(\omega)$ as $\omega\to\infty$,

$$Q_{I\ II}(\omega) \sim \frac{R^2(\bar{C}_{II})^{-1}}{I_1\omega^2}, \quad \omega\to\infty \tag{2.66}$$

which depends on the parameter $R^2(\bar{C}_{II})^{-1}/I_1$ and tends to zero as $\omega\to\infty$. *Hence, referring to Eq. (2.60), we see that in both limiting cases as* $\omega\to 0$ *and* $\omega\to\infty$, *no dynamic forces arise in the test gear mesh I from the static transmission error* $\hat{\zeta}'_{II}$ *of the slave gear mesh II.* For intermediate frequencies $0<\omega<\infty$, however, finite forces will arise in mesh I from the static transmission error in mesh II.

THE RESPONSE

We shall now combine the excitation Fourier series representation with the system transfer functions to predict response metrics of interest.

Mesh and Bearing-Support Dynamic Load and Spectrum

Since the test gears shown in Fig. 1 are assumed to move in (unsteady) pure rotation, the time-varying force magnitudes $W_I(t)$ in the test gear mesh must equal the time-varying force magnitudes in the bearing supports, as illustrated in Fig. 1. Recalling from Eq. (2.22) that τ_a/R is the time-average force W_0 in mesh I, we can express $W_I(t)$ as

$$W_I(t) = \tau_a/R + \delta W_I(t) \ , \tag{3.1}$$

where $\delta W_I(t)$ represents the deviation of $W_I(t)$ from its time-average value τ_a/R. From Eq. (2.60) and the *linearity* of the Fourier transformation operation, we see that $\delta W_I(t)$ can be decomposed into two components — a component $\delta W_{II}(t)$ arising from the static transmission error excitation from the test gear mesh I, and a component $\delta W_{I\ II}(t)$ arising from the static transmission error excitation from the slave gear mesh II. Hence, we may write Eq. (3.1) as

$$W_I(t) = \tau_a/R + \delta W_{II}(t) + \delta W_{I\ II}(t). \tag{3.2}$$

Since in our predictions we are taking into account only the tooth meshing harmonics of the static transmissions error of meshes I and II, it follows from Eq. (2.60) that $\delta W_{II}(t)$ is a periodic function with period equal to the tooth meshing period of mesh I and $\delta W_{I\ II}(t)$ is periodic with period equal to the tooth meshing period of mesh II. Thus, $\delta W_{II}(t)$ and $\delta W_{I\ II}(t)$ may be represented by complex Fourier series,

$$\delta W_{II}(t) = \sum_{n=-\infty}^{\infty} \alpha_{WII}(n) e^{i2\pi n f_I t} \tag{3.3}$$

and

$$\delta W_{I\ II}(t) = \sum_{n=-\infty}^{\infty} \alpha_{WI\ II}(n) e^{i2\pi n f_{II} t} \tag{3.4}$$

where f_I and f_{II} are the tooth meshing fundamental frequencies of meshes I and II respectively, which can be expressed as

$$f_I = N_I(\text{rpm})/60 \tag{3.5}$$

and

$$f_{II} = N_{II}(\text{rpm})/60. \tag{3.6}$$

N_I and N_{II} are the numbers of teeth on the test and slave gears respectively, and rpm denotes the number of revolutions per minute of all shafts in the test rig. $\alpha_{WII}(n)$ and $\alpha_{WI\ II}(n)$ denote complex Fourier series coefficients.

It follows from the relationship between the Fourier transform and Fourier series delineated in Appendix G of Reference 4 [especially Eq. (G6)] that we may express the complex Fourier series coefficients of $\delta W_{II}(t)$ and $\delta W_{I\ II}(t)$ with the aid of Eqs. (2.60) and (3.2) through (3.4) as

$$\alpha_{WII}(n) = (\bar{C}_I)^{-1} Q_{II}(\omega_{nI})\alpha_{mnI} \tag{3.7}$$

and

$$\alpha_{WI\ II}(n) = (\bar{C}_I)^{-1} Q_{I\ II}(\omega_{nII})\alpha_{mnII}, \tag{3.8}$$

where

$$\omega_{nI} = 2\pi n f_I \tag{3.9}$$

$$\omega_{nII} = 2\pi n f_{II}, \tag{3.10}$$

and where α_{mnI} and α_{mnII} denote, respectively, the complex Fourier series coefficients α_{mn} given by Eq. (1.5) for the static transmission errors arising from meshes I and II. As Eq. (1.5) indicates, α_{mnI} and α_{mnII} is each the sum of three components that are the Fourier series coefficients of the three terms on the right-hand sides of Eqs. (2.22) and (2.23) respectively. The transfer functions $Q_{II}(\omega)$ and $Q_{I\ II}(\omega)$ are defined by Eqs. (2.58) and (2.59) respectively.

The temporal behavior of $\delta W_{II}(t)$ and $\delta W_{I\ II}(t)$ can be constructed from the Fourier series coefficients, Eqs. (3.7) and (3.8), using Eqs. (3.3) and (3.4). These quantities are then added to τ_a/R to yield the temporal behavior of the mesh and bearing support forces $W_I(t)$ as indicated by Eq. (3.2).

Finally, assuming that the "phase" between the teeth of meshes I and II is unknown, we may express the *one-sided* power spectral density of $W_I(t)$ as

$$\Phi_{WI}(f) = (\tau_a/R)^2\delta(f) + \sum_{n=0}^{\infty} 2|\alpha_{WII}(n)|^2\delta(f-nf_I) + \sum_{n=0}^{\infty} 2|\alpha_{WI\ II}(n)|^2\delta(f-nf_{II}) \ , \qquad (3.11)$$

where we have been aided by Eq. (109) of Reference 4. In Eq. (3.11), $\delta(\cdot)$ denotes the Dirac delta function; hence, Eq. (3.11) describes a line spectrum with a dc contribution arising from the mean force τ_a/R and additional contributions arising from the tooth meshing harmonics nf_I of the test gear mesh I and nf_{II} of the slave gear mesh II. Notice from Eqs. (2.62) and (2.65) that $Q_{II}(\omega)$ and $Q_{I\ II}(\omega)$ both vanish at $\omega=0$, so we see from Eqs. (3.7) and (3.8) that no dc contributions arise from the terms n=0 in the two sums in Eq. (3.11).

Dynamic Force on a Single Tooth

We turn now to obtaining an expression for the time-varying root stress on a typical tooth of the test gears. We first require the time-varying force on a typical tooth. Let us denote this force by $W^{\dagger}_{Ij}(t)$. Here, W denotes force, I denotes that the test gears have been designated as mesh I, j denotes tooth number used here as a reminder that $W^{\dagger}_{Ij}(t)$ represents the force on a *single* tooth only, and the dagger denotes that here we are considering time to be our independent variable rather than the lineal variable $x = R\theta$ used earlier – e.g., in Eqs. (1.2) and (1.3). For a fixed speed of rotation there is, of course, a one-to-one correspondence between x and t that is determined by $x(t) = R\theta(t) = R\dot{\theta}(t-t_0)$, where t_0 is a fixed reference time.

Let $K^{\dagger}_{Sj}(t)$ denote the stiffness of tooth pair j as defined by Eq. (1.16) except that here time is our independent variable. Stiffness $K^{\dagger}_{Sj}(t)$ varies with time because of the temporal variation of the line of contact on the tooth faces as the gears rotate. Let $u^{\dagger(1)}_j(t)$ and $u^{\dagger(2)}_j(t)$ denote the elastic deformations of tooth pair j of gears (1) and (2) of test gear mesh I. Then it follows directly from Eqs. (5) and (8b) of Reference 4 and Eq. (1.16) above that for spur gears with $u^{(1)}$ and $u^{(2)}$ independent of axial location y we have

$$W^{\dagger}_{Ij}(t) = K^{\dagger}_{Sj}(t)\left[u^{\dagger(1)}_{j}(t)+u^{\dagger(2)}_{j}(t)\right]. \tag{3.12}$$

Let $\zeta^{\dagger}_{mI}(t)$ denote the *dynamic* transmission error of test gear mesh I. Subscript m denotes that we are considering here only the effects of the *mean* profile modification as described in Reference 4 and Section 1 of the present report. The dynamic transmission error $\zeta^{\dagger}_{mI}(t)$ is identical with the quantities described by Eqs. (2.11) and (2.13) except that here t is the independent variable. Let $m^{\dagger(1)}_{Sj}(t)$ and $m^{\dagger(2)}_{Sj}(t)$ denote the mean profile modifications of teeth j on gears (1) and (2) of the test gear pair. These modifications are identical with the definition, Eq. (1.24), except that here time is again considered to be the independent variable as denoted by the dagger superscripts. Then, according to Eqs. (5) and (6) of Reference 4 when no random tooth face errors are present, we have

$$u^{\dagger(1)}_{j}(t) + u^{\dagger(2)}_{j}(t) = \zeta^{\dagger}_{mI}(t)-m^{\dagger(1)}_{Sj}(t)-m^{\dagger(2)}_{Sj}(t) , \tag{3.13}$$

which, when substituted into Eq. (3.12) gives

$$W^{\dagger}_{Ij}(t) = K^{\dagger}_{Sj}(t)\left[\zeta^{\dagger}_{mI}(t)-m^{\dagger(1)}_{Sj}(t)-m^{\dagger(2)}_{Sj}(t)\right]. \tag{3.14}$$

Equation (3.14) is the spur gear counterpart to Eq. (8c) of Reference 4 when no random tooth face errors are present.

Rewriting Eq. (2.13) using our present notation gives for the dynamic transmission error

$$\zeta^{\dagger}_{mI}(t) = \overline{C}_{I}W_{I}(t) + \zeta'_{I}(t) , \tag{3.15}$$

where we recall that $W_{I}(t)$ is the total force transmitted by the test gear mesh I and $\zeta'_{I}(t)$ is the *static* transmission error of mesh I as defined by Eq. (2.12). If we again denote Fourier transforms of quantities by placing a caret over the transformed variable, we have for the Fourier transform of Eq. (3.15)

$$\hat{\zeta}^{\dagger}_{mI} = \overline{C}_{I}\,\hat{W}_{I} + \hat{\zeta}'_{I} . \tag{3.16}$$

Multiplying both sides of Eq. (2.60) by $\overline{C}_{I}$ and substituting the resulting expression into Eq. (3.16) gives for the Fourier transform of the *dynamic* transmission error of mesh I

$$\hat{\zeta}^{\dagger}_{mI} = \left[1+Q_{II}(\omega)\right]\hat{\zeta}'_{I} + Q_{I\ II}(\omega)\hat{\zeta}'_{II} \ , \ \omega \neq 0, \qquad (3.17)$$

where $Q_{II}(\omega)$ and $Q_{I\ II}(\omega)$ are defined by Eqs. (2.58) and (2.59) respectively, and $\hat{\zeta}'_{II}$ is the Fourier transform of the *static* transmission error of mesh II as defined by Eq. (2.12).

Equation (3.17) shows that the *dynamic* transmission error of mesh I is made up of three components, a *direct* component $\hat{\zeta}'_{I}$ equal to the *static* transmission error of mesh I, an *indirect* component whose transform is $Q_{II}(\omega)\hat{\zeta}'_{I}$ that represents the contribution to $\zeta^{\dagger}_{mI}$ resulting from the system dynamic response to ζ'_{I}, and finally, a component whose transform is $Q_{I\ II}(\omega)\hat{\zeta}'_{II}$ resulting from the system dynamic response to the static transmission error ζ'_{II} of the slave gear mesh II. From Eqs. (2.62) and (2.65), we have found that $Q_{II}(\omega)$ and $Q_{I\ II}(\omega)$ both tend to zero as $\omega \to 0$ so that for sufficiently small ω it follows from Eq. (3.17) that $\hat{\zeta}^{\dagger}_{mI}$ and $\hat{\zeta}'_{I}$ coincide – that is, the dynamic and static transmission errors of mesh I become identical for very low frequencies of excitation (as expected). On the other hand, as $\omega \to \infty$, we have found from Eqs. (2.64) and (2.66) respectively that $Q_{II}(\omega) \to -1$ and $Q_{I\ II}(\omega) \to 0$, so that for sufficiently large ω it follows from Eq. (3.17) that the dynamic transmission error $\zeta^{\dagger}_{mI}$ of mesh I tends to vanish. This is the mathematical manifestation of the fact that, for sufficiently high frequencies of excitation, the inertia of the gears prevents the static transmission errors of meshes I and II from causing any substantial lack of uniformity in the rate of rotation of the test gears.

Let us now define

$$\hat{\zeta}^{\dagger}_{mII} \triangleq \left[1+Q_{II}(\omega)\right]\hat{\zeta}'_{I} \qquad (3.18)$$

and

$$\hat{\zeta}^{\dagger}_{mI\ II} \triangleq Q_{I\ II}(\omega)\hat{\zeta}'_{II} \ , \qquad (3.19)$$

which, respectively, are the Fourier transforms of the contributions of the static transmission errors of meshes I and II to the Fourier transform of the dynamic transmission error $\hat{\zeta}^{\dagger}_{mI}$ of mesh I – i.e.,

$$\hat{\zeta}^{\dagger}_{mI} = \hat{\zeta}^{\dagger}_{mII} + \hat{\zeta}^{\dagger}_{mI\ II} \ . \qquad (3.20)$$

Then, denoting the inverse Fourier transforms of $\hat{\zeta}^{\dagger}_{mII}$ and $\hat{\zeta}^{\dagger}_{mI\ II}$, respectively, by

$$\zeta^{\dagger}_{mII}(t) = F^{-1}[\hat{\zeta}^{\dagger}_{mII}]$$

$$= F^{-1}\left\{[1+Q_{II}(\omega)]\hat{\zeta}'_{I}\right\} \tag{3.21}$$

and

$$\zeta^{\dagger}_{mI\ II}(t) = F^{-1}[\zeta^{\dagger}_{mI\ II}]$$

$$= F^{-1}[Q_{I\ II}(\omega)\hat{\zeta}'_{II}], \tag{3.22}$$

where we have used Eqs. (3.18) and (3.19), we then have by substituting the inverse transform of Eq. (3.20) into Eq. (3.14)

$$W^{\dagger}_{Ij}(t) = K^{\dagger}_{Sj}(t)\left[\zeta^{\dagger}_{mII}(t)+\zeta^{\dagger}_{mI\ II}(t)-m^{\dagger(1)}_{Sj}(t)-m^{\dagger(2)}_{Sj}(t)\right] \tag{3.23}$$

Equation (3.23) expresses the dynamic force $W^{\dagger}_{Ij}(t)$ transmitted by a typical tooth pair j of the test gear mesh I in terms of the tooth pair stiffness $K^{\dagger}_{Sj}(t)$ of the same two teeth, the dynamic transmission error contributions $\zeta^{\dagger}_{mII}(t)$ and $\zeta^{\dagger}_{mI\ II}(t)$ to mesh I from the static transmission errors of meshes I and II respectively, and the profile modifications $m^{\dagger(1)}_{Sj}(t)$ and $m^{\dagger(2)}_{Sj}(t)$ of the two meshing teeth in contact. Quantities $m^{\dagger(1)}_{Sj}(t)$ and $m^{\dagger(2)}_{Sj}(t)$ are considered positive when they are "equivalent" to removal of material from perfect involute surfaces.

The dynamic transmission error components $\zeta^{\dagger}_{mII}(t)$ and $\zeta^{\dagger}_{mI\ II}(t)$ are to be evaluated using Eqs. (3.21) and (3.22). To carry out this evaluation we recognize that $\hat{\zeta}'_{I}$ contains only the tooth meshing harmonics of mesh I; hence, we can represent $\zeta^{\dagger}_{mII}(t)$ by the complex Fourier series

$$\zeta^{\dagger}_{mII}(t) = \sum_{n=-\infty}^{\infty} \alpha_{\zeta mII}(n)e^{i2\pi nf_I t}, \tag{3.24}$$

where f_I is the tooth meshing fundamental frequency of mesh I to be evaluated using Eq. (3.5). Similarly, $\hat{\zeta}'_{II}$ contains only tooth meshing harmonics of mesh II; hence, we can represent $\zeta^{\dagger}_{mI\ II}(t)$ by the Fourier series

$$\zeta^{\dagger}_{mI\ II}(t) = \sum_{n=-\infty}^{\infty} \alpha_{\zeta mI\ II}(n) e^{i2\pi n f_{II} t} , \tag{3.25}$$

where f_{II} is to be evaluated using Eq. (3.6). The complex Fourier series coefficients $\alpha_{\zeta mII}(n)$ and $\alpha_{\zeta mI\ II}(n)$ in Eqs. (3.24) and (3.25) are to be evaluated from the Fourier series coefficients of the static transmission errors ζ'_I and ζ'_{II} of meshes I and II with the help of Eqs. (3.18) and (3.19) — i.e.,

$$\alpha_{\zeta mII}(n) = [1+Q_{II}(\omega_{nI})]\alpha_{mnI} , \tag{3.26}$$

and

$$\alpha_{\zeta mI\ II}(n) = Q_{I\ II}(\omega_{nII})\alpha_{mnII}, \tag{3.27}$$

where ω_{nI} and ω_{nII} are defined by Eqs. (3.9) and (3.10) respectively, the α_{mnI}, $n=0,\pm1,\pm2,\cdots$ are the Fourier series coefficients defined by Eq. (1.5) of the static transmission error of mesh I, and the α_{mnII} are the Fourier series coefficients defined by Eq. (1.5) of the static transmission error of mesh II. Each of these Fourier series coefficients is the sum of three terms as indicated by Eq. (1.5).

The left-hand sides of Eqs. (3.26) and (3.27) are the complex harmonic amplitudes of the contributions to the dynamic transmission error of mesh I from the static transmission error harmonic amplitudes of meshes I and II respectively. The right-hand side of Eq. (3.26) exhibits a "direct self" contribution α_{mnI} from the static transmission error plus the dynamic increment contribution $Q_{II}(\omega_{nI})\alpha_{mnI}$, whereas the right-hand side of Eq. (3.27) $Q_{I\ II}(\omega_{nII})\alpha_{mnII}$ is the increment to mesh I from mesh II which arises from dynamic effects only. (We have shown earlier by Eqs. (2.62) and (2.65) that $Q_{II}(\omega)$ and $Q_{I\ II}(\omega)$ both tend to zero as $\omega\to0$. Hence, for i = I or II and j = I or II, $Q_{ij}(\omega)$ represents the *dynamic* contribution to the (dynamic) transmission error complex harmonic amplitude at mesh i from a unit amplitude harmonic component of the static transmission error at mesh j. This fact suggests that the term *"transmission error dynamic increment function"* or the more brief term *"dynamic increment function"* be applied to the transfer functions $Q_{ij}(\omega)$. This concept, and the foregoing analysis, readily generalizes to gearing systems with an arbitrary number of dynamically interacting meshes.

Equations (3.23) through (3.27) are one set of final expressions for evaluation of the temporal behavior of the forces $W^{\dagger}_{Ij}(t)$ transmitted by a typical pair of teeth on the test gears.

Decomposition of dynamic single tooth force into static and dynamic increment contributions. Instead of using the form of $W^{\dagger}_{Ij}(t)$ given by Eq. (3.23), we can again begin with Eq. (3.14) and decompose the dynamic transmission error $\zeta^{\dagger}_{mI}(t)$ of mesh I into the original static transmission error $\zeta_{mI}(t)$ of mesh I plus dynamic increment contributions to mesh I arising from meshes I and II — i.e.,

$$\zeta^{\dagger}_{mI}(t) = \zeta_{mI}(t) + \delta\zeta^{\dagger}_{mII}(t) + \delta\zeta^{\dagger}_{mI\ II}(t) , \tag{3.28}$$

where $\zeta_{mI}(t)$ is the static transmission error of mesh I defined by Eqs. (1.3) through (1.5), and $\delta\zeta^{\dagger}_{mII}$ and $\delta\zeta^{\dagger}_{mI\ II}(t)$ are the dynamic increments to the transmission error of mesh I arising from meshes I and II respectively. Then, by substituting Eq. (3.28) into Eq. (3.14), we see that the dynamic force $W^{\dagger}_{Ij}(t)$ can be decomposed into components $W^{\dagger}_{Ij_0}(t)$ and $\delta W^{\dagger}_{Ij}(t)$ arising, respectively from the static transmission error $\zeta_{mI}(t)$ and the dynamic increments $\delta\zeta^{\dagger}_{mII}(t) + \delta\zeta^{\dagger}_{mI\ II}(t)$ — i.e.,

$$W^{\dagger}_{Ij}(t) = W^{\dagger}_{Ij_0}(t) + \delta W^{\dagger}_{Ij}(t) , \tag{3.29}$$

where

$$W^{\dagger}_{Ij_0}(t) \triangleq K^{\dagger}_{Sj}(t)[\zeta_{mI}(t) - m^{\dagger(1)}_{Sj}(t) - m^{\dagger(2)}_{Sj}(t)], \tag{3.30}$$

and

$$\delta W^{\dagger}_{Ij}(t) \triangleq K^{\dagger}_{Sj}(t)[\delta\zeta^{\dagger}_{mII}(t) + \delta\zeta^{\dagger}_{mI\ II}(t)]. \tag{3.31}$$

The static transmission error $\zeta_{mI}(t)$ can be expressed in terms of its Fourier series coefficients α_{mnI} by

$$\zeta_{mI}(t) = \sum_{n=-\infty}^{\infty} \alpha_{mnI} e^{i2\pi n f_I t} , \tag{3.32}$$

where f_I is the tooth meshing fundamental frequency of mesh I to be evaluated using Eq. (3.5), and the α_{mnI} are the Fourier series coefficients of the static transmission error of mesh I defined by Eq. (1.5). The dynamic increment $\delta\zeta^{\dagger}_{mII}(t)$ can be represented in terms of its Fourier series coefficients $Q_{II}(\omega_{nI})\alpha_{mnI}$ by

$$\delta\zeta^{\dagger}_{mII}(t) = \sum_{n=-\infty}^{\infty} Q_{II}(\omega_{nI})\alpha_{mnI} e^{i2\pi n f_I t} , \tag{3.33}$$

and the other dynamic increment $\delta\zeta^{\dagger}_{mI\ II}(t)$ can be represented by

$$\delta\zeta^{\dagger}_{mI\ II}(t) = \sum_{n=-\infty}^{\infty} Q_{I\ II}(\omega_{nII})\alpha_{mnII} e^{i2\pi n f_{II} t} , \tag{3.34}$$

where ω_{nI} and ω_{nII} are defined by Eqs. (3.9) and (3.10) respectively, f_{II} is the tooth meshing fundamental frequency of mesh II to be evaluated using Eq. (3.6), and the α_{mnII} are the Fourier series coefficients of the static transmission error of mesh II defined by Eq. (1.5). The transmission error components in Eqs. (3.23) and (3.28) are related by

$$\zeta^{\dagger}_{mII}(t) = \zeta_{mI}(t) + \delta\zeta^{\dagger}_{mII}(t) , \tag{3.35}$$

and

$$\zeta^{\dagger}_{mI\ II}(t) \equiv \delta\zeta^{\dagger}_{mI\ II}(t) . \tag{3.36}$$

The representation of the dynamic force on a single tooth by Eqs. (3.29) through (3.34) has the advantage of separating out the force increment $\delta W^{\dagger}_{Ij}(t)$ arising from the dynamic response of the gearing system. Notice from Eqs. (3.33) and (3.34) that $Q_{II}(\omega_{nI})$ and $Q_{I\ II}(\omega_{nII})$ govern the dynamic response contributions from the static transmission errors of meshes I and II to the force increment $\delta W^{\dagger}_{Ij}(t)$. Furthermore, since $Q_{II}(0) = 0$ and $Q_{I\ II}(0) = 0$, we see from Eqs. (3.31), (3.33), and (3.34) that when all α_{mnI} and α_{mnII} are zero except for $n = 0$, we have $\delta W^{\dagger}_{Ij}(t) = 0$. *Hence, when the fluctuating components of the static transmission errors of meshes I and II are zero, Eqs. (3.31), (3.33), and (3.34) imply that no force increment* $\delta W^{\dagger}_{Ij}(t)$ *on a*

single tooth arises from the dynamic response of the gearing system.

Finally, we note that a somewhat more accurate expression for the total mesh force $W_I(t)$ than that given by Eqs. (3.2) through (3.10) can probably be obtained by summing the individual tooth forces $W_{Ij}^{+}(t)$ given by Eq. (3.29) over all teeth in contact at any given instant of time. However, in carrying out this summation, care must be exercised to take into account the appropriate "time delays" of the individual tooth forces.

Root Stress on a Single Tooth

Cornell [8] has modified a formula developed by Heywood [9] for the root fillet tensile stress in a gear tooth. Additional comments by Heywood and others on this problem appear in the discussion of the paper by Kelley and Pederson [10]. Cornell's modification of the Heywood formula is readily adapted to the geometry of gear teeth of nominal involute design — his modification can be expressed as

$$\sigma = \frac{W_j \cos\phi'_W}{t'} \left[1+0.26\left(\frac{h_s}{2r}\right)^{0.7}\right] \times \left[\frac{6\ell'_s}{h_s^2} + \left(\frac{0.72}{h_s \ell_s}\right)^{\frac{1}{2}} \left(1-\frac{h_W}{h_s}\nu\tan\phi'_W\right) - \frac{\tan\phi'_W}{h_s}\right] \qquad (3.37)$$

where σ is the root stress and W_j is the tooth loading denoted by W_{Ij} in the case of mesh I, and given by Eqs. (3.23) or (3.29). The remainder of the notation in Eq. (3.37), and expressions for the parameters contained therein, are contained in Appendix B of this report. The procedure developed by Cornell [8] for determination of the position of the maximum root fillet tensile stress also is described in Appendix B.

PROFILE DESIGN FOR MINIMUM EXCITATION

Profile Modification to Compensate for Tooth and Gear Body Deformations at the Design Loading

Let $\zeta(x)$ denote the (dynamic) transmission error as defined in Reference 4 and expressed by Eq. (2.6) of this report. Here, the transmission error is expressed as a function of the coordinate x, which can be related to the angular position θ of either gear of a meshing pair by Eq. (1.2). The requirement that the teeth of the gear pair remain in contact at each value of x dictates [4] that the tooth surfaces must move together relative to the tooth surfaces of rigid perfect involute gears by the distance

$$\zeta(x) = u_j^{(1)}(x) + u_j^{(2)}(x) + m_j^{(1)}(x) + m_j^{(2)}(x) \ , \qquad (4.1)$$

where $u_j^{(1)}(x)$ and $u_j^{(2)}(x)$ are the elastic deformations of the jth (meshing) teeth on gears (1) and (2), and $m_j^{(1)}(x)$ and $m_j^{(2)}(x)$ are the modifications of the profiles of the same teeth on gears (1) and (2) from perfect involute profiles. Quantities ζ, $u^{(\cdot)}$ and $m^{(\cdot)}$ are measured in a direction defined by the intersection of the plane of contact and the transverse plane. *Quantities* $u_j^{(\cdot)}(x)$ *and* $m_j^{(\cdot)}(x)$ *are defined as positive when they are "equivalent" to removal of material from the surfaces of unloaded, perfect, uniformly spaced involute teeth* [4]. Thus, a positive value of $\zeta(x)$ corresponds to tooth surfaces *coming together* relative to those of rigid perfect involute gears.

It follows from the definition of the static transmission error that if a real pair of meshing gears is to transmit exactly uniform angular motion then $\zeta(x)$ must be a constant [11-13]. In addition, however, if we wish to insure that the tooth faces under loading take on the form of perfect uniformly spaced involute teeth, we must require that the tooth faces from *each* gear be modified to compensate for their own elastic deformations — i.e., that the geometrical deviation of each tooth face take on the form

$$m_j^{(1)}(x) = -u_j^{(1)}(x) \qquad (4.2a)$$

$$m_j^{(2)}(x) = -u_j^{(2)}(x) \qquad (4.2b)$$

which will yield zero static transmission error, $\zeta(x) = 0$, when combined with Eq. (4.1). When Eqs. (4.2a) and (4.2b) are *both* satisfied, we are guaranteed that all tooth pair contact remains

in the plane of contact; however, satisfaction of the *single* condition

$$m_j^{(1)}(x) + m_j^{(2)}(x) = -\left[u_j^{(1)}(x)+u_j^{(2)}(x)\right] \tag{4.3}$$

will *not* guarantee this behavior, and therefore, will not guarantee the transmission of *exactly* uniform angular motion [14].

To evaluate the right-hand sides of Eqs. (4.2a) and (4.2b), we require the loading $W_j(x)$ carried by each tooth pair j in contact, as well as the appropriate stiffness characterizations. The tooth pair loadings $W_j(x)$ must be constrained by the relationship:

$$W_d = \sum_j W_j(x) \ , \tag{4.4}$$

where W_d is the total loading transmitted by the gear pair, where the summation over j in the right-hand side includes all tooth pairs in contact, and where all forces in Eq. (4.4) are in the direction defined by the intersection of the plane of contact and the transverse plane. The constant force W_d is the *design loading* of the gear pair for minimum vibration excitation. Following Harris [11, 12] and Remmers [13], our design approach will be to specify the individual forcing functions $W_j(x)$ so that the overall loading constraint, Eq. (4.4), is satisfied. In particular, this design approach permits us to control the individual tooth loading functions $W_j(x)$ at the initiation of tooth contact.

Let $c_{jj'}^{(\cdot)}(x)$ denote the influence function [15] that describes the surface deformation of the contact patch of tooth j on gear $(\cdot)$ due to a "unit" loading of the contact patch of tooth j' on the same gear, as illustrated in Fig. 2. The center positions of the contact patches are determined by the rotational position $\theta^{(\cdot)}$ of gear $(\cdot)$ as described by the lineal variable $x = R_b^{(\cdot)}\theta^{(\cdot)}$, where all superscripts $(\cdot)$ refer to the same gear of the pair. The direction of all such deformations and loadings is defined by the intersection of the plane of contact and the transverse plane. The width 2b of the contact patch on tooth j and the semi-elliptical pressure distribution under this contact patch are determined by the prescribed loading $W_j(x)$ transmitted by tooth pair j and the two *local* radii of curvature of the jth teeth on gears (1) and (2) at their contact point – as determined, e.g., from Eqs. (235) and (236) on p. 418 of Reference [16]. Thus, the influence functions $c_{jj'}^{(\cdot)}(x)$ include bending, shear, Hertzian contact, and gear

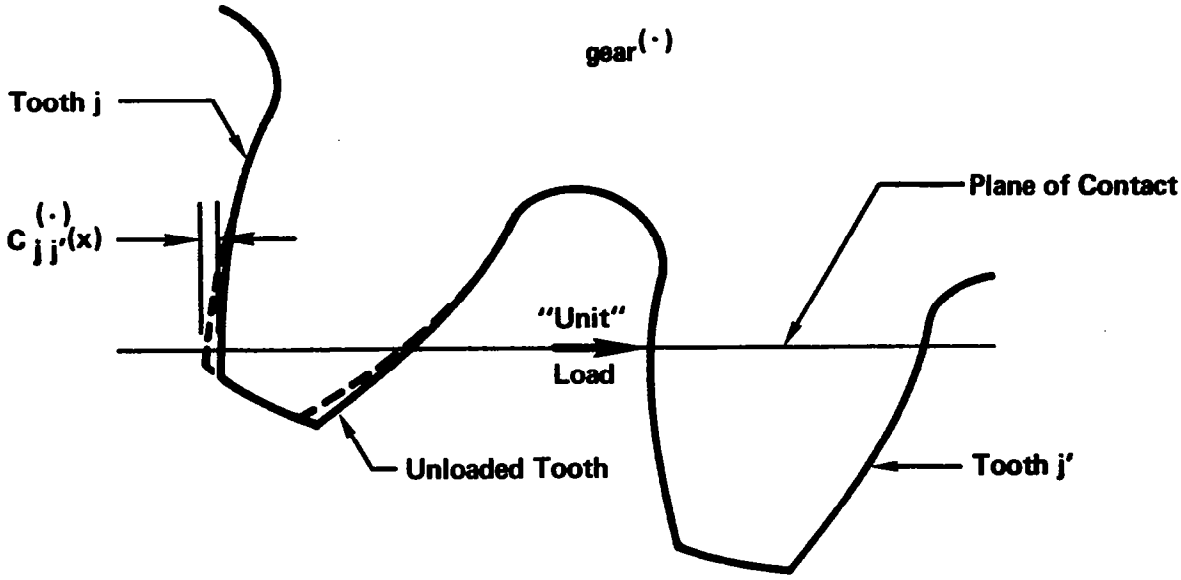

FIG. 2. ILLUSTRATION OF THE INFLUENCE FUNCTION $c_{jj'}^{(\cdot)}(x)$ FOR THE CASE $j \neq j'$.

body deformations, where these latter deformations are particularly important in determining the deformation of one tooth caused by loading on another tooth, which is the case $j' \neq j$ illustrated in Fig. 2. The influence functions $c_{jj'}^{(\cdot)}(x)$ can be computed using finite element techniques; however, particular care must be exercised to insure accurate computation of the contact deformation component.

From the influence functions and the prescribed loading functions, we can compute the deformation of tooth j on gear $(\cdot)$ as a function of x by superposition

$$u_j^{(\cdot)}(x) = \sum_{j'} c_{jj'}^{(\cdot)}(x)\, W_{j'}(x) \,, \tag{4.5}$$

where the summation over j' includes all teeth in contact at position $x = R_b^{(\cdot)}\theta^{(\cdot)}$. By combining Eq. (4.5) written for gears (1) and (2) of the meshing pair with Eqs. (4.2a) and (4.2b), we obtain our final *profile modification formulas for spur gears:*

$$m_j^{(1)}(x) = -\sum_{j'} c_{jj'}^{(1)}(x)\, W_{j'}(x) \tag{4.6a}$$

$$m_j^{(2)}(x) = -\sum_{j'} c_{jj'}^{(2)}(x)\, W_{j'}(x) \,, \tag{4.6b}$$

where the loads $W_j(x)$ transmitted by the individual pairs of teeth are subject to the constraint, Eq. (4.4), and where a positive value of $m_j^{(\cdot)}(x)$ corresponds to *"removal"* of material from a perfect involute profile. From Eqs. (4.6a), (4.6b), and (4.4), we see that it is possible to modify the profiles of both gears of a meshing pair to completely compensate for tooth deformations only at a single design loading W_d.

Thus far, we have ignored the thickness of the layer of lubricant between pairs of meshing teeth. These effects could be included, if known, by adding one-half of the local layer thickness to the right-hand sides of Eqs. (4.6a) and (4.6b).

Discussion: When the profile modifications $m_j^{(1)}(x)$ and $m_j^{(2)}(x)$ of all teeth on a pair of meshing gears are machined to exactly satisfy Eqs. (4.6a) and (4.6b), the static transmission error of that gear pair is set equal to zero when the gears are operating at the design loading W_d. For the present discussion, let us assume that the profile modifications of the test gears, shown as mesh I

in Fig. 1, have been machined so as to satisfy Eqs. (4.6a) and (4.6b). In this case, all Fourier series coefficients α_{mnI} $n = \pm 1, \pm 2, \cdots$ of the static transmission's error are identical to zero. It then follows from Eqs. (3.3) and (3.7) that the time varying component $\delta W_{II}(t)$ of the mesh and bearing force attributable to mesh I in Eq. (3.2) is identically zero. Similarly, if the teeth of the slave gears in mesh II were modified according to Eqs. (4.6a) and (4.6b), the time varying force component $\delta W_{I\ II}(t)$ in Eq. (3.2) attributable to the slave gears would be identically zero as can be seen from Eqs. (3.4) and (3.8).

Turning now to the dynamic force components on a single tooth, we recall that $\delta W^{\dagger}_{Ij}(t)$ given by Eq. (3.31) is the component of the force history on a single tooth of mesh I attributable to the *vibratory excitation* from meshes I and II. Examination of Eqs. (3.31), (3.33) and (3.34) shows that when the teeth of the gears in meshes I and II are designed according to Eqs. (4.6a) and (4.6b) to eliminate the static transmission errors of those meshes, their corresponding contributions to $\delta W^{\dagger}_{Ij}(t)$ vanish thereby eliminating $\delta W^{\dagger}_{Ij}(t)$. Furthermore, we see from Eq. (3.32) that $\zeta_{mI}(t)$ also vanishes in this case, thus leaving

$$W^{\dagger}_{Ij_0}(t) = -K^{\dagger}_{Sj}(t)\left[m^{\dagger(1)}_{Sj}(t)+m^{\dagger(2)}_{Sj}(t)\right] \tag{4.7}$$

as the time-varying force history on a typical tooth of mesh I.

Each of the single tooth loading components in Eqs. (3.29) through (3.31) gives rise to a corresponding component of root stress. Thus, when the static transmission errors of the mesh and slave gears are eliminated at a design loading W_d, the components of root stress arising from the single tooth loading component $\delta W^{\dagger}_{Ij}(t)$ of Eq. (3.31) are eliminated, and the resultant root stress is that resulting from the tooth loading component given by Eq. (4.7).

Families of Tooth Loading Functions

The design procedure suggested in the previous section is to modify the profiles on the teeth of two meshing gears as prescribed by Eqs. (4.6a) and (4.6b), where the loading histories $W_j(x)$ on the individual teeth must satisfy the constraint given by Eq. (4.4). This procedure is most easily carried out by specifying the loading histories W (x) subject to the constraint, Eq. (4.4), and then solving for the profile modifications given by Eqs. (4.6a)

and (4.6b). We recall according to Eq. (1.2) that independent variable x is the roll distance

$$x = R_b^{(1)}\theta^{(1)} = R_b^{(2)}\theta^{(2)} \tag{4.8}$$

which is common to both meshing teeth, and $R_b^{(\cdot)}$ and $\theta^{(\cdot)}$ are the base circle radius and the roll angle of each gear of the meshing pair where $(\cdot)$ designates the gear (1) or (2) of the pair as appropriate.

Initially, let us restrict our considerations to spur gear pairs with contact ratios between one and two. There exists an infinite number of individual tooth loading histories $W_j(x)$ that satisfy Eq. (4.4). Figure 3 illustrates the individual tooth loading histories $W_j(x)$ and the manner in which they add up to satisfy the constraint, Eq. (4.4). The ordinate of Fig. 3 is force transmitted between the teeth of driving and driven gear in the direction defined by the intersection of the plane of contact and the transverse plane. The abscissa in Fig. 3 is roll distance $x = R_b\theta$. Alternating intervals of single tooth pair contact and two tooth pair contact are shown in the figure. The heavy line represents the loading and unloading force history $W_j(x)$ on the jth tooth of one of the pair of meshing gears. The dashed lines illustrate the force histories on teeth j-1 and j+1 as indicated. The roll distance interval during contact of a particular tooth is L and the base pitch is Δ.

In order for the condition indicated by Eq. (4.4) to be satisfied during regions of single pair contact, the design loading W_d must be carried by that tooth pair as indicated in Fig. 3. On the other hand, during regions of two tooth pair contact, the total loading W_d must be shared by the two tooth pairs in contact. This requirement means that distances A and A' shown in Fig. 3 must be identical.

If the direction of rotation of the gear pair were to be reversed, and if in this reversed situation the former driving gear becomes the new driven gear and vice versa, the "loading side" of the teeth in the former situation also remains loaded in this reversed situation. This reversed situation in effect reverses the direction of the x-axis in Fig. 3. This reversal of the direction of the x-axis suggests that it is reasonable to require the tooth loading histories $W_j(x)$ to be symmetric about the midpoint x_0 of the tooth contact interval L — i.e., to require that

$$W_j(x-x_0) = W_j[-(x-x_0)]. \tag{4.9}$$

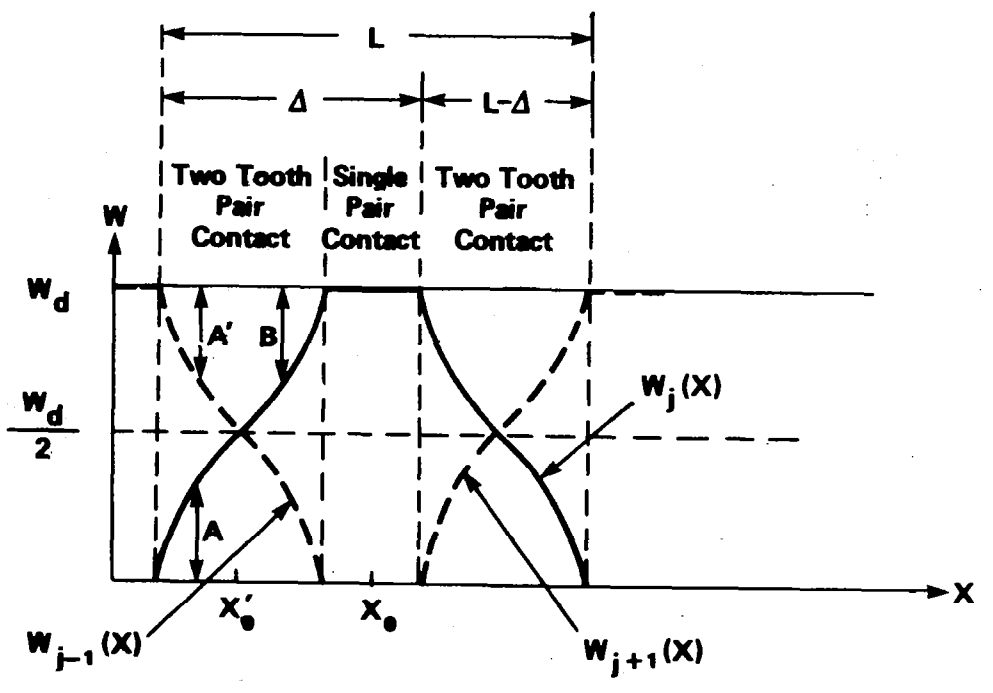

FIG. 3. TOOTH LOADING FUNCTION FOR CONTACT RATIO BETWEEN ONE AND TWO.

In particular, this condition implies that the abruptness of loading onset and loading release on a given tooth be the same. Whenever the condition of Eq. (4.9) is met, one can readily see from the periodicity of the individual loading curves in Fig. 3 that distances A' and B must the same; hence, the symmetry requirement Eq. (4.9) together with the loading constraint Eq. (4.4) jointly imply that distances A and B in Fig. 3 be the same. *In other words, the single tooth loading curve in a region of two tooth pair contact must be an odd function about the axis* $W = W_d/2$ *when Eqs. (4.4) and (4.9) are satisfied.* Finally, within each region of two tooth pair contact, we should like to require that practical tooth loading curves be *monotonic*, which implies that the slope of the tooth loading curve not change sign within that region. Sketches of tooth loading functions have appeared in References 11 and 13.

The non-constant portions of tooth loading functions satisfying the mirror image property, Eq. (4.9), are defined entirely by their behavior within a single two tooth pair contact region as is easily seen from Fig. 3. Let us define a new independent, dimensionless roll distance variable

$$\bar{x} \triangleq \frac{x-x_0'}{(L-\Delta)/2} \quad , \tag{4.10}$$

where x_0' is the center of the two tooth pair contact region as illustrated in Fig. 3. Thus, the new normalized roll distance variable ranges from $-1 \leq \bar{x} \leq 1$ within the two tooth pair contact region. Let us also define a dimensionless tooth loading variable

$$\bar{W}_j \triangleq \frac{W_j-(W_d/2)}{W_d/2} \tag{4.11}$$

which also ranges from $-1 < \bar{W}_j < 1$ when W_j ranges from 0 to W_d.

A simple family of tooth loading functions that satisfy all of the above mentioned criteria is the family

$$\bar{W}_j(\bar{x}) = \bar{x} + \left(\frac{1-\bar{s}}{\pi}\right)\sin(\pi\bar{x}) \quad , \qquad -1 \leq \bar{x} \leq 1 \tag{4.12}$$

where for $\bar{W}_j(\bar{x})$ to remain monotonic, we must have $0 \leq \bar{s} \leq 2$. The parameter $\bar{s}$ is the *slope* of $\bar{W}_j(\bar{x})$ at $\bar{x} = -1$, i.e.,

$$\bar{s} = \left.\frac{d\bar{W}_j}{d\bar{x}}\right|_{\bar{x}=-1}. \tag{4.13}$$

Figure 4 illustrates the behavior of Eq. (4.12) over the range of values of $\bar{s}$ for which $\bar{W}_j(\bar{x})$ is monotonic.

For tooth pairs with profile modifications designed using Eqs. (4.6a) and (4.6b), the sensitivity of the *actual* roll distance contact range L to variations of the actual mesh loading from the design loading W_d depends strongly on the slope of profile modification at the points of tooth contact initiation and termination. This profile modification slope, in turn, depends strongly on the slope of the tooth loading functions $W_j(x)$ at points of contact initiation and termination which is governed by the dimensionless slope $\bar{s}$ defined by Eq. (4.13). [Recall that $\bar{s}$ also controls the slope at contact termination because of the mirror image property Eq. (4.9)]. Thus, if it is desirable to minimize changes in the actual value of L over a wide range of mesh loadings, then a large value of $\bar{s}$ should be used in the profile modification design loading function $\bar{W}_j(\bar{x})$. We can see from Eq. (4.12) or Fig. 4 that the sinusoidal-based loading function is limited to initial dimensionless slopes $\bar{s}$ less than or equal to 2 if it is to remain monotonic.

A second family of tooth loading functions that does not have this limitation is the polynomial-based normalized family

$$\bar{W}_j(\bar{x}) = \frac{r-\bar{s}}{r-1}\,\bar{x} + \frac{\bar{s}-1}{r-1}\,\bar{x}^r \,, \qquad -1 \leqslant \bar{x} \leqslant 1 \tag{4.14}$$

where the parameter r is permitted to take on only the odd integer values $r = 3,5,7,\cdots$. This definition of $\bar{W}_j(\bar{x})$ remains monotonic provided that the initial (dimensionless) slope $\bar{s}$ remains within the range $0 \leqslant \bar{s} \leqslant r$. Thus, if a large value of $\bar{s}$ is desired, a correspondingly large value of r must be chosen in the loading function, Eq. (4.14).

Figures 5 and 6 illustrate the normalized families of tooth loading functions of Eq. (4.14) for values of r = 3 and 7 respectively. From these two figures, we see that as r is increased the loading function of Eq. (4.14) permits an ever increasing initial slope $\bar{s}$ of $\bar{W}_j(\bar{x})$ while retaining its monotonic increasing character. Figure 7 shows how the loading functions of Eq. (4.14) vary when the initial slope $\bar{s}$ is held to the constant value $\bar{s} = 3$, while r is varied from values of 3 to 9.

Figures 4 through 7 collectively illustrate the considerable flexibility of shapes available in the two families of loading functions described by Eqs. (4.12) and (4.14). Notice that Eqs. (4.12) and (4.14) both reduce to the same linear function $\bar{W}_j(\bar{x}) = \bar{x}$ when $\bar{s}$ is taken to be unity.

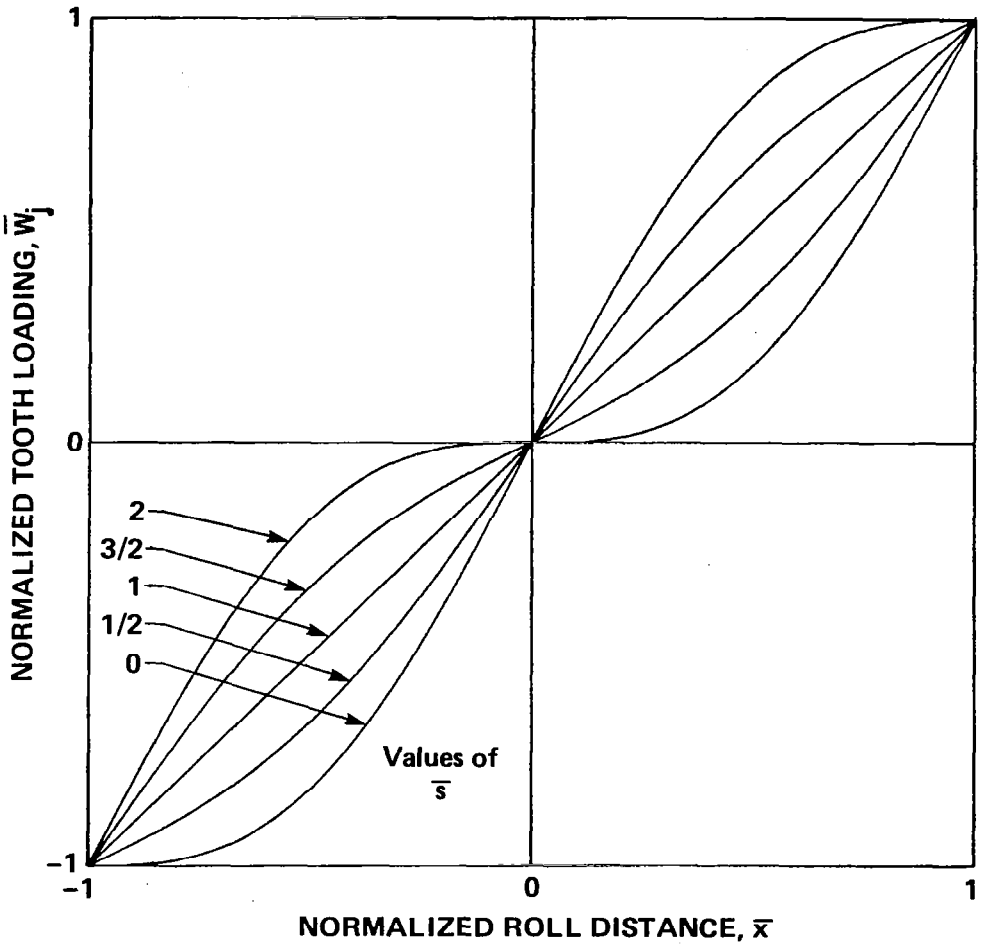

FIG. 4. NORMALIZED SINUSOIDAL-BASED FAMILY OF TOOTH LOADING FUNCTIONS.

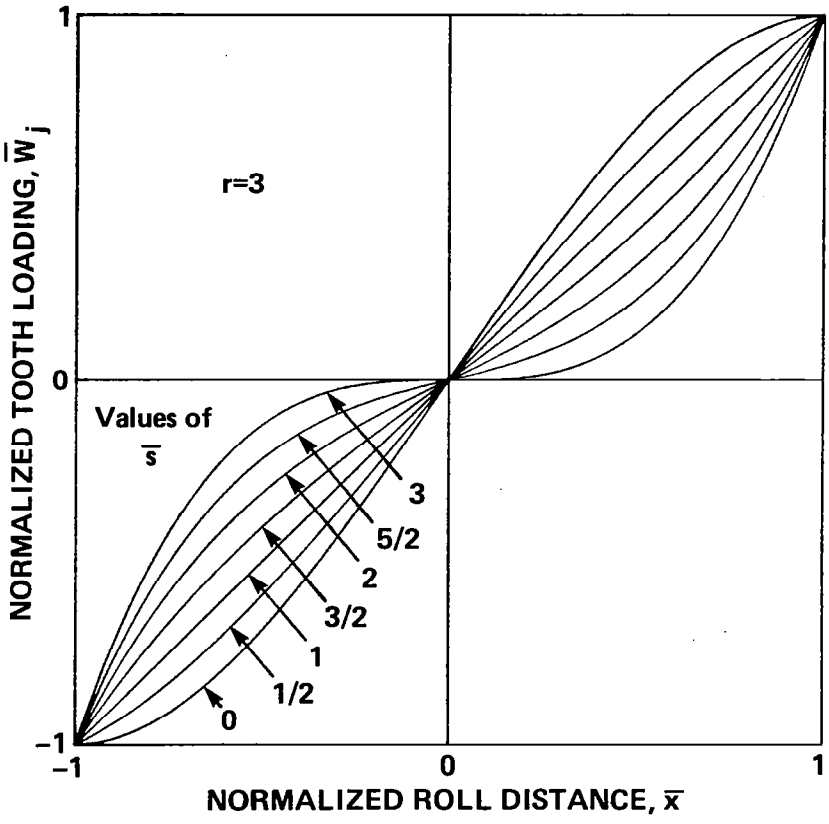

FIG. 5. NORMALIZED POLYNOMIAL-BASED FAMILY OF TOOTH LOADING FUNCTIONS FOR r = 3.

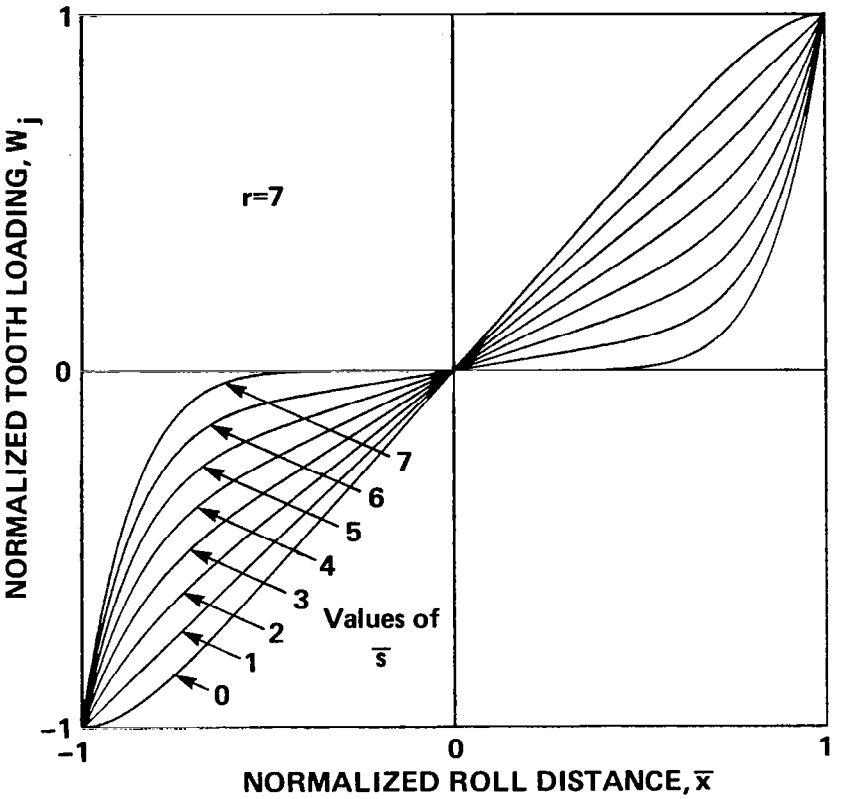

FIG. 6. NORMALIZED POLYNOMIAL-BASED FAMILY OF TOOTH LOADING FUNCTIONS FOR r=7.

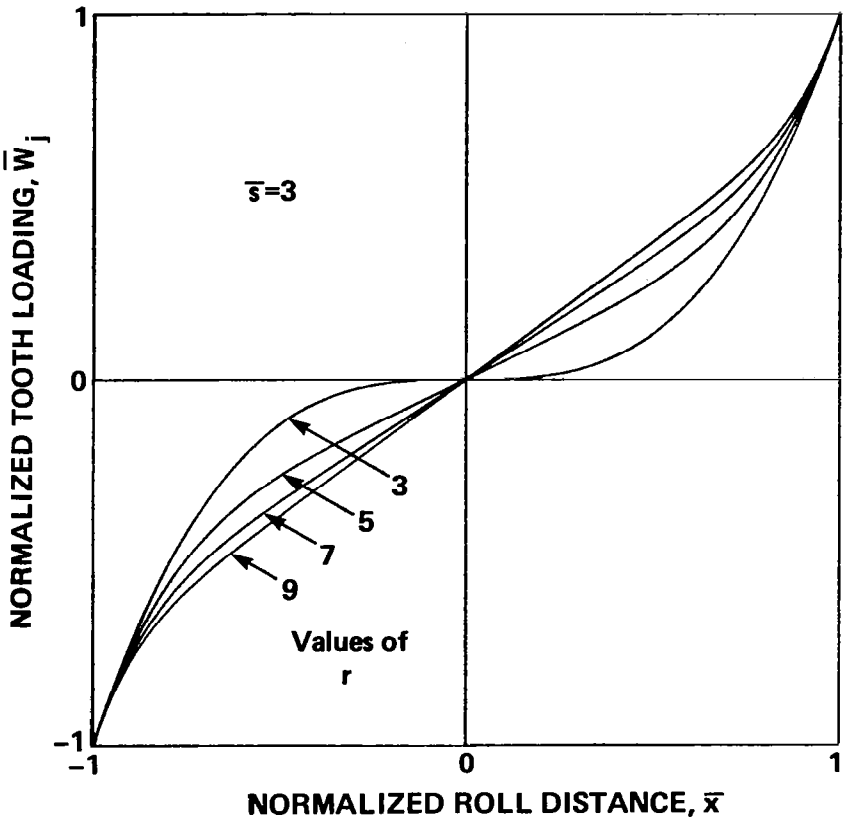

FIG. 7. NORMALIZED POLYNOMIAL-BASED FAMILY OF TOOTH LOADING FUNCTIONS FOR $\bar{s}$=3.

Families of tooth loading functions satisfying Eq. (4.4) for contact ratios larger than 2 can readily be generated. Figure 8 illustrates a linear tooth loading function $W_j(x)$ for a contact ratio between 2 and 3 that satisfies Eq. (4.4). Here, in addition to the parameters L and Δ, and the mesh loading W_d, we have an additional free parameter F, where FW_d is the maximum value of $W_j(x)$, as can be seen from Fig. 8. For the portion of the tooth loading curve $W_j(x)$ to remain monotonic in the region $x \leq x_0$, the parameter F must be chosen to lie within the range $1/2 \leq F \leq 1$. In practice, F can be chosen to be the value that minimizes the maximum root stress of a tooth.

Examination of each small, dashed, rectangular box in Fig. 8 shows that the sum of the two individual tooth loading curves within each box equals the height of the box. However, this is exactly the requirement placed on the tooth loading curves within each two-tooth contact region illustrated in Fig. 3. Thus, each straight line segment and its mirror image in Fig. 8 could be replaced by any of the loading curves shown in Figs. 4 through 7 and their respective mirror images to yield various families of curved tooth loading functions — all of which would satisfy the fundamental design constraint Eq. (4.4) and the symmetry property, Eq. (4.9). In particular, use of the polynomial-base family illustrated in Figs. 5 through 7 permits, for any choice of the parameter F shown in Fig. 8, a completely free choice of the slope of $W_j(x)$ at contact initiation and termination provided that r is chosen sufficiently large. For a given choice of contact initiation slope, minimization of the maximum root stress on a tooth might require simultaneous variations of the two parameters r and F in the stress minimization procedure. (Hertzian) contact stress minimization might also be taken into account in such a minimization procedure.

Excitation Spectra of Tooth Loading Functions

A tooth loading function, such as that illustrated by the heavy line in Fig. 3, has the potential for exciting vibratory motion of the *tooth* itself [17]. Such potential tooth vibrations are more likely to be a problem in high speed gearing, since an increase in gear rotational speed will reduce the total duration during which a tooth is loaded, thereby "shifting" the spectrum of the tooth loading function to the higher frequency range where tooth resonance frequencies are found. To assess the potential for such excitation of tooth resonant frequencies, the Fourier transforms of the tooth loading functions $W_j(x)$ are required. Each of the *dimensionless* loading functions, Eqs. (4.12) and (4.14), can be combined with its mirror image to determine a *dimensional* tooth loading function as illustrated in Fig. 3. The Fourier transform of the resulting *sinusoidal-based* loading function with origin at $x = x_0$ is

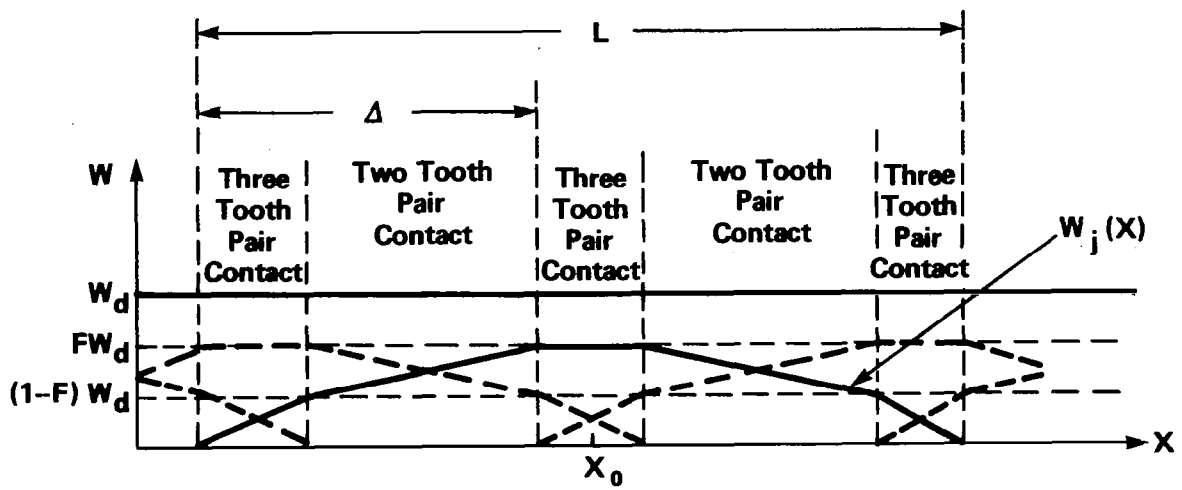

FIG. 8. TOOTH LOADING FUNCTION FOR CONTACT RATIO BETWEEN 2 AND 3.

$$F_x[W_j(x);g] \triangleq \int_{-\infty}^{\infty} W_j(x)e^{-i2\pi gx}dx \tag{4.15a}$$

$$= W_d\Delta \frac{\sin(\pi\Delta g)}{\pi\Delta g}\left\{\frac{\sin[\pi(L-\Delta)g]}{\pi(L-\Delta)g}\left[\frac{1-\bar{s}(L-\Delta)^2g^2}{1-(L-\Delta)^2g^2}\right]\right\} \tag{4.15b}$$

whereas, the Fourier transform of the resulting *polynomial-based loading* function with origin at $x = x_0$ is

$$F_x[W_j(x);g] = W_d\Delta \frac{\sin(\pi\Delta g)}{\pi\Delta g}\left\{\bar{s}\frac{\sin[\pi(L-\Delta)g]}{\pi(L-\Delta)g} + \left(\frac{1-\bar{s}}{r-1}\right)\sum_{k=2}^{r}\frac{r!}{(r-k)!}\frac{\cos[\pi(L-\Delta)g+\frac{1}{2}k\pi]}{[\pi(L-\Delta)g]^k}\right\},$$

$$r = 3,5,7,\cdots, \quad \bar{s} \leqslant r. \tag{4.16}$$

The right-hand sides of Eqs. (4.15b) and (4.16) both have the form of $W_d\Delta \sin(\pi\Delta g)/(\pi\Delta g)$ times a quantity within curly braces. Thus, we can study the effects of the dimensionless slope $\bar{s}$ at contact initiation and termination [Eq. (4.13)] by examination of the behavior of the quantities within the curly braces in Eqs. (4.15b) and (4.16). The magnitudes of these quantities are plotted on log-log coordinates for the sinusoidal-based loading function in Figs. 9a to 9d, and for the polynomial-based loading function in Figs. 10a to 10d and 11a to 11d. The ordinate in Figs. 9a through 11d is the (dimensionless) magnitude of the quantities within the curly braces in Eqs. (4.15b) and (4.16), and the abscissa is measured in units of

$$q = (L-\Delta)g = \left(\frac{L}{\Delta} - 1\right)\Delta g, \tag{4.17}$$

where g is the transform variable indicated by Eq. (4.15a).

To interpret the dimensionless frequency q, we note that since Δ is the base pitch, its reciprocal $1/\Delta$ is the tooth meshing fundamental frequency in the frequency units g, which we denote by $g_{\text{tooth-mesh}}$. Thus

$$\Delta g \equiv \frac{g}{\Delta^{-1}} = \frac{g}{g_{\text{tooth mesh}}} = p, \tag{4.18}$$

where p is the *tooth meshing harmonic number* which is unity at the tooth meshing fundamental frequency. Combining Eqs. (4.17) and (4.18) gives

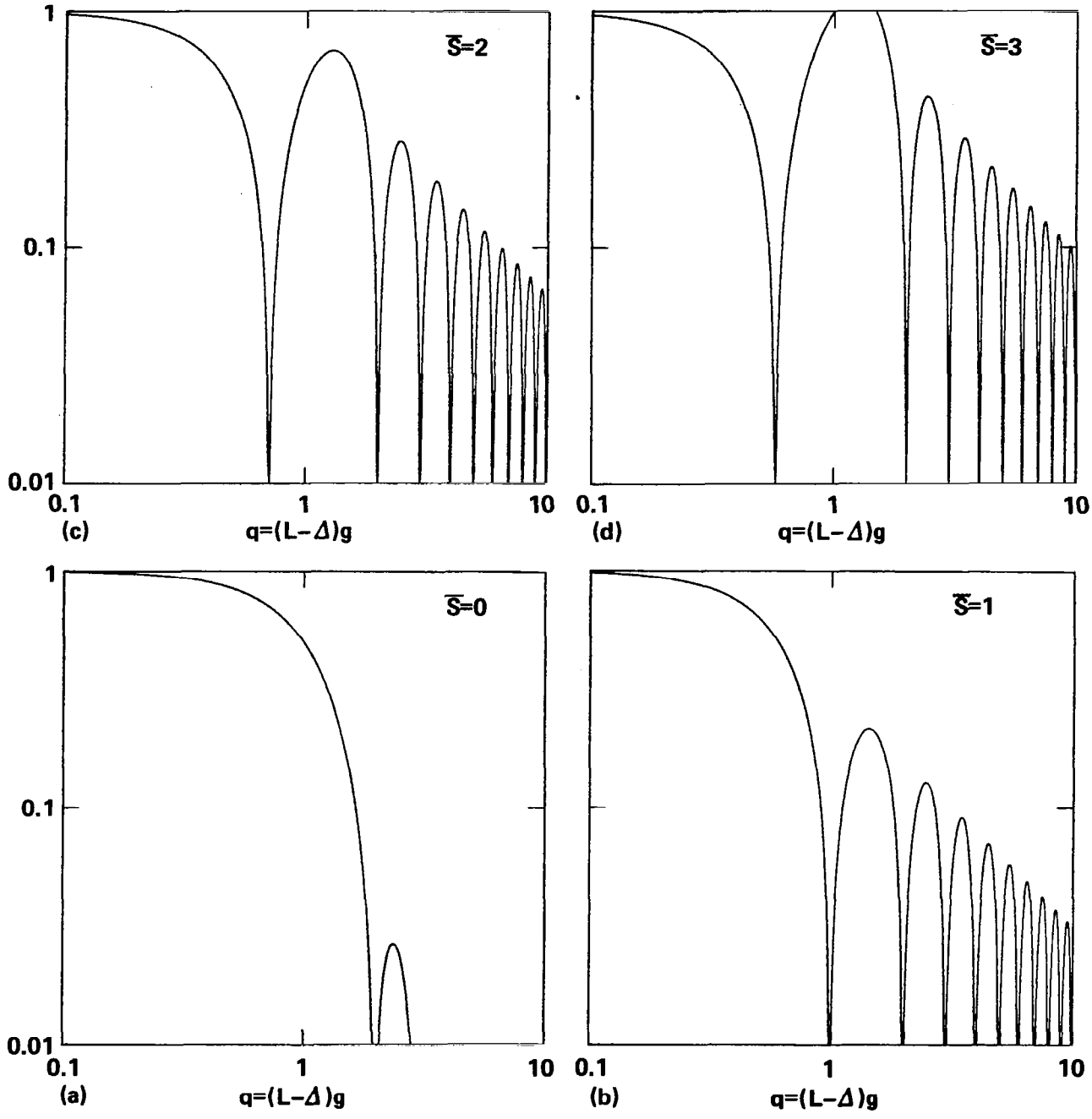

FIG. 9. SPECTRUM FACTOR WITHIN CURLY BRACES IN EQ. (4.15) ON LOG-LOG COORDINATES FOR SINUSOIDAL-BASED TOOTH LOADING FUNCTION.

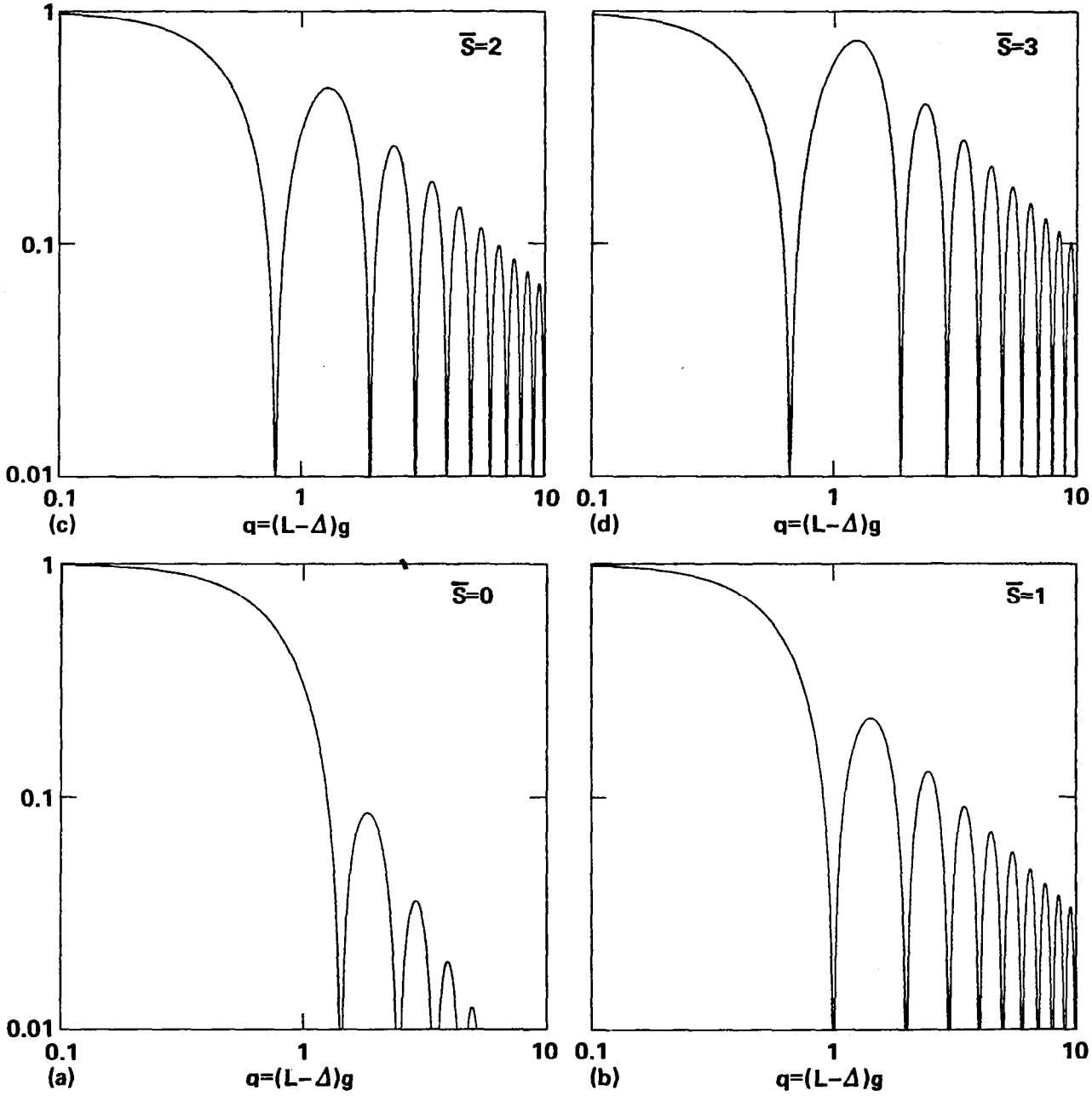

FIG. 10. SPECTRUM FACTOR WITHIN CURLY BRACES IN EQ. (4.16) ON LOG-LOG COORDINATES FOR POLYNOMIAL-BASED TOOTH LOADING FUNCTION FOR r=3.

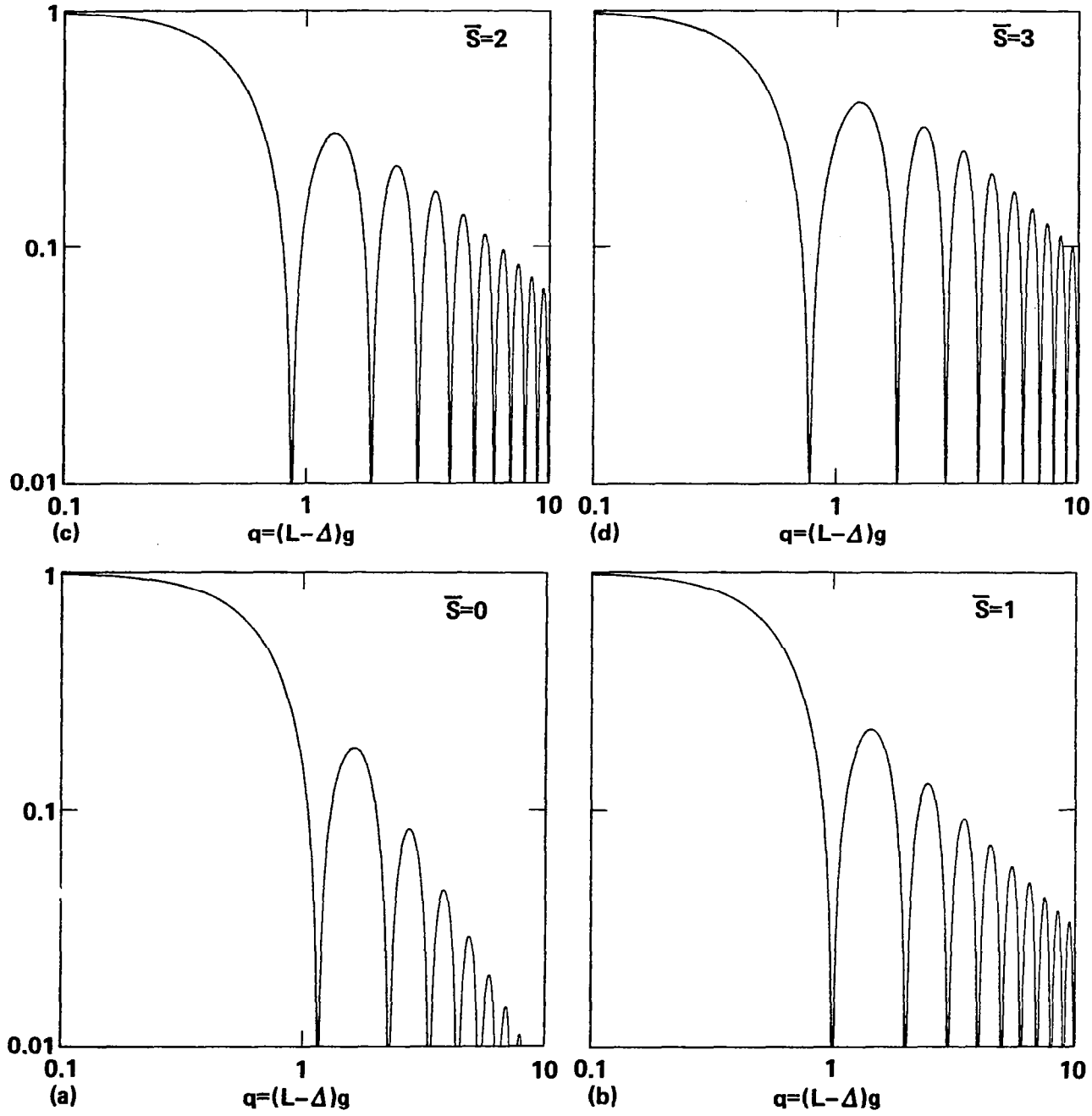

FIG. 11. SPECTRUM FACTOR WITHIN CURLY BRACES IN EQ. (4.16) ON LOG-LOG COORDINATES FOR POLYNOMIAL-BASED TOOTH LOADING FUNCTION FOR r=7.

$$q = \left(\frac{L}{\Delta}-1\right)\frac{g}{g_{\text{tooth mesh}}} = \left(\frac{L}{\Delta}-1\right)p \ , \tag{4.19}$$

where we recall that (L/Δ) is the transverse contact ratio which is generally in the approximate neighborhood of $(L/\Delta) \approx 1.5$

Examination of Eqs. (4.15b) and (4.16) shows that both equations have the same *high frequency asymptotic behavior:*

$$\begin{aligned} F_x[W_j(x);g] &\sim W_d\Delta\frac{\sin(\pi\Delta g)}{\pi\Delta g}\left\{\bar{s}\,\frac{\sin[\pi(L-\Delta)g]}{\pi(L-\Delta)g}\right\} \\ &= W_d\Delta\frac{\sin(\pi\Delta g)}{\pi\Delta g}\left\{\bar{s}\,\frac{\sin(\pi q)}{\pi q}\right\} . \end{aligned} \tag{4.20}$$

We see that the quantity within the curly braces in Eq. (4.20) is independent of r, from which it follows that provided $\bar{s} \neq 0$ the high frequency asymptotic behavior of all curves with the same value of $\bar{s}$ in Figs. 9 through 11 should be the same. The figures are in agreement with this behavior. Furthermore, from Eqs. (4.10), (4.11), and (4.13), we see that

$$\bar{s} = \left.\frac{d\bar{W}_j}{d\bar{x}}\right|_{\bar{x}=-1} = \left.\frac{(L-\Delta)}{W_d}\,\frac{dW_j}{dx}\right|_{\text{contact initiation}} \tag{4.21}$$

where the slope of the tooth loading function is evaluated at the point of contact initiation. Combining this result with the first form of Eq. (4.20) gives for the *high-frequency asymptotic behavior* of $F_x[W_j(x);g]$:

$$F_x[W_j(x);g] \sim \left.\frac{\sin(\pi\Delta g)\,\sin[\pi(L-\Delta)g]}{\pi^2 g^2}\,\frac{dW_j}{dx}\right|_{\text{contact initiation}} \tag{4.22}$$

whose envelope is $(\pi^2g^2)^{-1}(dW_j/dx)_{\text{contact initiation}}$. Thus, we see that the high frequency content of the Fourier transform of the tooth loading function is directly proportional to its slope at the point of contact initiation.

As a consequence of this fact, we have a trade-off in choosing the tooth loading functions $W_j(x)$ for high-speed gearing. On the one hand, a large value of the slope of $W_j(x)$ at points of contact initiation and termination will minimize variations in the tooth contact region for loadings other than the design loading. On the other hand, such large values of the slope of $W_j(x)$ will also give

rise to more energy in the high frequency portion of the spectrum of $W_j(x)$, and therefore will be more likely to excite tooth resonant vibrations. For tooth loading functions with the same slope magnitudes at points of contact initiation and termination, Eq. (4.22) provides a simple formula for estimating the high frequency region of the Fourier transform of $W_j(x)$ for investigating the importance of the resonant response of gear teeth.

APPLICATION

The theoretical results of the preceding sections of the report are applied to the NASA Lewis four-square test apparatus in this section.

Profile Modification for Minimum Vibration Excitation

The initial step in the profile modification design procedure is to specify the individual tooth loading function $W_j(x)$ illustrated in Fig. 3, where $W_j(x)$ is subject to the constraint given by Eq. (4.4). The simplest loading function to satisfy Eq. (4.4) is that characterized by the dimensionless function $\bar{W}_j(\bar{x})$ given either by Eq. (4.12) or Eq. (4.14) for the case where $\bar{s} = 1$. [For this value of $\bar{s}$, Eq. (4.12) and (4.14) both describe the *dimensionless* linear loading characterization $\bar{W}_j(\bar{x}) = \bar{x}$, $-1 \leqslant \bar{x} \leqslant 1$.] For this case, the full dimensional loading function $W_j(x)$ becomes the function with linear load sharing curves shown in Fig. 12, which is symmetric about the pitch point. The abscissa of Fig. 12 represents "roll distance" $\delta x = R_b \delta\theta$, where $\delta\theta$ is an increment of gear rotational angle in radians and R_b is the base circle radius of the same gear. The maximum potential roll distance over which a tooth can be loaded can be determined by Eqs. (D8), (D11), and (D12) of Ref. 4 from the addenda radii and pitch radii of the two meshing gears and the pressure angle. Both test gears in the NASA Lewis four-square apparatus have R_a = 4.7625 cm (1.875 in) and R = 4.445 cm (1.750 in) for their addenda radii and pitch radii respectively. Their pressure angle is 20°. Utilizing Eqs. (D8), (D11), and (D12) of Ref. 4, we find the maximum *potential* value of roll distance for these test gears to be $L_{nominal}$ = 1.53530 cm (.604450 in) as shown in Fig. 12. However, the tip rounding radius on the test gears reduces the *actual* maximum value of roll distance to a value of about L = 1.37450 cm (.5411406 in). Furthermore, it was our desire to allow for *at least* a 20% increase in loading of the test gears beyond the design loading, and to allow for tooth spacing errors without encountering tip interference. Thus, we have chosen the *design value* of roll distance to be L = 1.22971 cm (.48414 in). This value can be computed from the values shown in Fig. 12 — i.e., 1.53530 - (2x.152794) = 1.22971 cm. The values of roll distance increment during load sharing of .29235 cm are computed from the *design value* of L = 1.22971 cm and the base pitch Δ. The base pitch is computed from the pitch radius R = 4.445 cm, number of teeth N = 28, and pressure angle ϕ = 20° by the relation

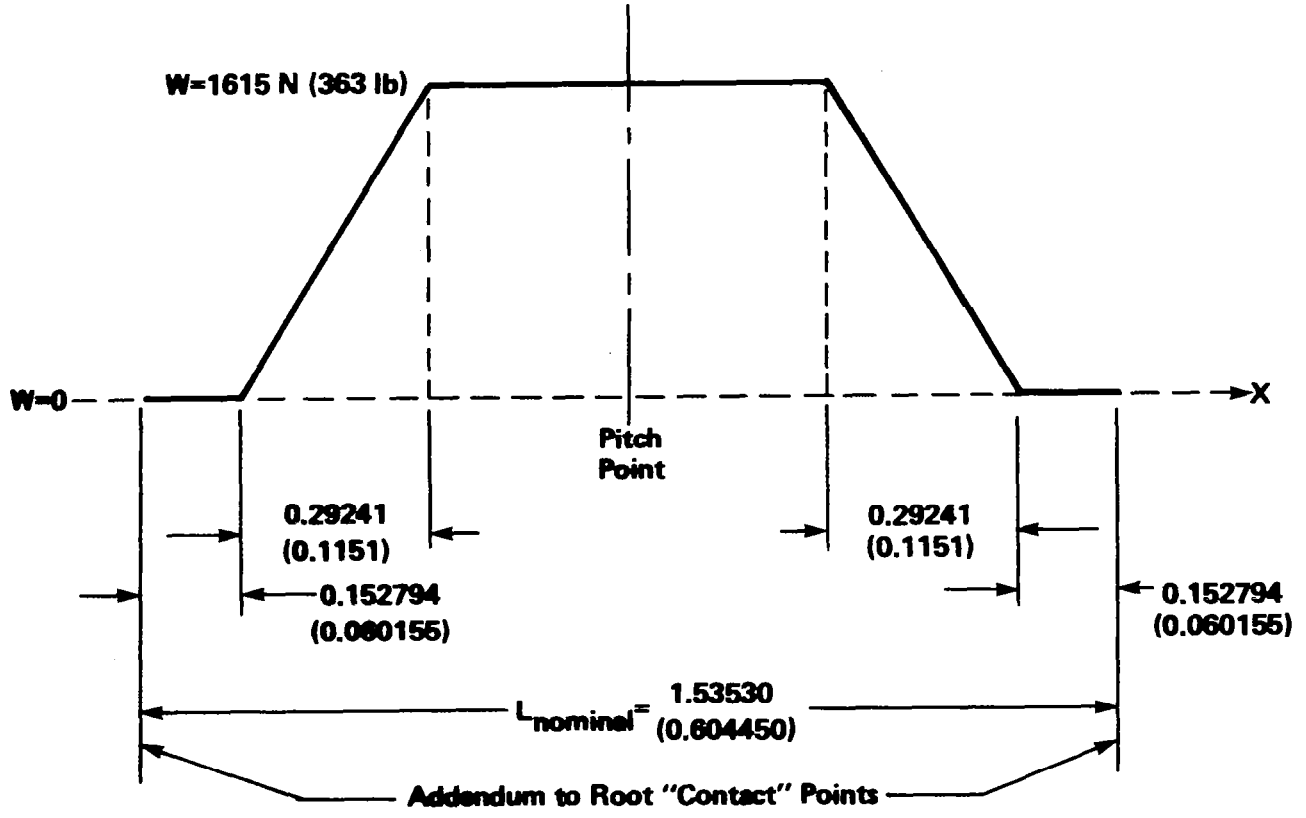

FIG. 12. TOOTH LOADING FUNCTION FOR COMPUTATION OF TOOTH STIFFNESS [LENGTH DIMENSIONS ARE IN CM (IN).].

$$\Delta = \frac{2\pi R}{N} \cos\phi = .93730 \text{ cm } (.36902 \text{ in}). \qquad (5.1)$$

The roll distance increment during load sharing is L-Δ (see Fig. 3.), which in the present case is

$$L-\Delta = 1.22971 - .93730 = .29241 \text{ cm } (.1151 \text{ in}) \qquad (5.2)$$

as is shown in Fig. 12. The tooth loading function shown in Fig. 12 was constructed in the above manner. These values result in a *design* contact ratio of (L/Δ) = (1.22971/.93730) = 1.312, which is a completely acceptable value.

The tooth loading diagram shown in Fig. 12 was transmitted to NASA Lewis and used there to compute the tooth deformations required to carry out the profile modification designs. See Fig. 4 of Ref. 18, where the roll angle increments δθ in degrees are obtained from the roll distances δx shown in Fig. 12 by the relation

$$\delta\theta_{deg} = \frac{360}{2\pi R_b} \delta x \ , \qquad (5.3)$$

where, for the test gears in question, the base circle radius is R_b = 4.17693 cm (1.64446 in).

Reference 18 computes the deformation under the loaded tooth, but not the component of deformation under neighboring teeth due to that loading. Thus, to illustrate the profile design method described in the preceding section, we shall *assume* here that when only one tooth is loaded, the deformations of all neighboring teeth are zero. That is, for the present approximate profile modification design, we shall assume that $c_{jj'}(x) = 0$ when $j \neq j'$, where the $c_{jj'}(x)$ are the influence functions in the profile design formulas given by Eqs. (4.6a) and (4.6b). Employing this assumption, and recognizing that, in the present application, both meshing test gears are identical, we see that both design equations (4.6a) and (4.6b) are reduced in this (approximate) application to

$$m_j(x) = -c_{jj}(x)\, W_j(x) \ , \qquad (5.4)$$

which is the negative of the tooth deformation due to application of the loading $W_j(x)$ illustrated in Fig. 12. However, according to our sign convention, a negative value of $m_j(x)$ is equivalent to an addition of material to the involute design. Thus, the *approximate* result of Eq. (5.4) states that an amount of material depth equal to the tooth deformation under the loading $W_j(x)$ must be added to the perfect involute tooth surface to minimize the vibration excitation. This depth is measured in a direction defined by the intersection of the base plane and a plane normal to the gear

axes. This is the direction normal to the perfect involute surfaces before modification.

The tooth deflections caused by the point loading function shown in Fig. 12 have been tabulated in Table III of Ref. 18, which has been reproduced as Table 1 of this report. Thus, the deflections listed in Table 1 are the depths of *addition* of material to the test gear pure involute profiles as described by the approximate result of Eq. (5.4).

Normally, profile modifications are thought of in terms of *removal of material* from perfect involute profiles. The amounts of material "removal" equivalent to the material "additions" listed as "Deflections" in Table 1 can be obtained by subtracting the deflection entries in Table 1 from the maximum deflection entry. The column entitled "Profile relief" (in) in Table 2 was computed in this manner by subtracting the corresponding "Deflections" (in) in Table 1 from 6.1733 E-4. The values of profile relief in mm were then computed by multiplying the (in) entries by 25.4.

Examination of the profile relief values given in Table 2 shows maximum values of profile relief at the two ends of the contact region (near tooth tip and root), with relief values monotonically decreasing to a value of zero in the center portion of the tooth. This general behavior is consistent with current industry practice, and is a consequence of the monotonically increasing and decreasing behavior of the tooth loading function shown in Fig. 12. Any of the sinusoidal or polynomial-based loading functions discussed in the preceding section would yield profile relief functions with the same general behavior as that tabulated in Table 2.

The teeth of *both* of the nominally identical test gears must be modified by the amounts indicated in Table 2 to compensate for their deflections under loading. The smaller values of roll angle designate the tooth regions nearer the tooth root, and the larger values of roll angle designate the tooth regions nearer the tip. The profile modification for approximate minimization of the vibratory excitation has the same shape as the tooth deflection function shown in Fig. 13. *The modifications of the root and tip regions beyond the design zone of contact are to be obtained by linear extrapolation of the profile relief values shown in Table 2. This procedure is equivalent to a linear extrapolation of the two ends of the curve shown in Fig. 13.* This increased relief in the tip and root regions will permit the application of mesh loadings at least 20% in excess of the 1615 N (363 lb) design loading without tip interference — including an allowance for modest tooth spacing errors.

Table 1. Tabulation of Single Tooth Loadings and Deflections as a Function of Roll Angle. Loadings were Obtained from Fig. 12. [From Ref. 18.]

Roll angle		Distance from pitch point along line of action		Load		Deflection	
rad	deg	mm	in.	N	lb	mm	in.
0.2208	12.65	-5.979	-0.2354	93.05	20.92	5.7412 E-4	2.2603 E-5
.2271	13.01	-5.718	-.2251	238.4	53.59	1.5026 E-3	5.9158 E-5
.2361	13.53	-5.342	-.2103	446.1	100.3	2.8184 E-3	1.1096 E-4
.2474	14.17	-4.867	-.1916	706.8	158.9	4.5072 E-3	1.7745 E-4
.2609	14.95	-4.308	-.1696	1018	228.9	6.5641 E-3	2.5843 E-4
.2760	15.81	-3.673	-.1446	1366	307.2	8.9797 E-3	3.5353 E-4
.2922	16.74	-2.997	-.1180	1615	363.0	1.0875 E-2	4.2813 E-4
.3084	17.67	-2.322	-.0914	1615	363.0	1 1200 E-2	4.4095 E-4
.3238	18.55	-1.676	-.0660	1615	363.0	1.1554 E-2	4.5488 E-4
.3386	19.40	-1.057	-.0416	1615	363.0	1.1930 E-2	4.6970 E-4
.3529	20.22	-.462	-.0182	1615	363.0	1.2345 E-2	4.8603 E-4
.3640	20.86	0	0	1615	363.0	1.2600 E-2	4.9605 E-4
.3747	21.47	.447	.0176	1615	363.0	1.3035 E-2	5.1320 E-4
.3876	22.21	.986	.0388	1615	363.0	1.3501 E-2	5.3155 E-4
.4000	22.92	1.506	.0593	1615	363.0	1.4004 E-2	5.5135 E-4
.4121	23.61	2.012	.0792	1615	363.0	1.4537 E-2	5.7233 E-4
.4237	24.28	2.497	.0983	1615	363.0	1.5090 E-2	5.9408 E-4
.4350	24.92	2.969	.1169	1615	363.0	1.5680 E-2	6.1733 E-4
.4458	25.54	3.419	.1346	1508	339.0	1.5132 E-2	5.9573 E-4
.4557	26.11	3.830	.1508	1280	287.7	1.3438 E-2	5.2905 E-4
.4645	26.61	4.199	.1653	1077	272.2	1.1713 E-2	4.6113 E-4
.4723	27.06	4.526	.1782	896.7	201.6	1.0058 E-2	3.9598 E-4
.4793	27.46	4.818	.1897	735.3	165.3	8.5060 E-3	3.3486 E-4
.4855	27.82	5.077	.1999	592.5	133.2	7.0455 E-3	2.7738 E-4
.4909	28.13	5.304	.2088	467.5	105.1	5.6937 E-3	2.2416 E-4
.4956	28.40	5.502	.2166	359.3	80.77	4.4691 E-3	1.7595 E-4
.4997	28.63	5.669	.2232	265.0	59.57	3.3726 E-3	1.3278 E-4
.5031	28.83	5.812	.2288	186.2	41.87	2.4210 E-3	9.5315 E-5
.5059	28.99	5.928	.2334	121.7	27.35	1.6135 E-3	6.3525 E-5
.5080	29.11	6.017	.2369	73.21	16.46	9.6342 E-4	3.7930 E-5

Table 2. Tabulation of Single Tooth Loadings and Profile Relief as a Function of Roll Angle for Approximate Minimization of Vibration Excitation.

Roll angle		Distance from pitch point along line of action		Load		Profile relief	
rad	deg	mm	in.	N	lb	mm	in.
0.2208	12.65	-5.979	-0.2354	93.05	20.92	1.5106 E-2	5.9473 E-4
.2271	13.01	-5.718	-.2251	238.4	53.59	1.4178 E-2	5.5817 E-4
.2361	13.53	-5.342	-.2103	446.1	100.3	1.2862 E-2	5.0637 E-4
.2474	14.17	-4.867	-.1916	706.8	158.9	1.1173 E-2	4.3988 E-4
.2609	14.95	-4.308	-.1696	1018	228.9	9.1161 E-3	3.5890 E-4
.2760	15.81	-3.673	-.1446	1366	307.2	6.7005 E-3	2.6380 E-4
.2922	16.74	-2.997	-.1180	1615	363.0	4.8057 E-3	1.8920 E-4
.3084	17.67	-2.322	-.0914	1615	363.0	4.4801 E-3	1.7638 E-4
.3238	18.55	-1.676	-.0660	1615	363.0	4.1262 E-3	1.6245 E-4
.3386	19.40	-1.057	-.0416	1615	363.0	3.7498 E-3	1.4763 E-4
.3529	20.22	-.462	-.0182	1615	363.0	3.3350 E-3	1.3130 E-4
.3640	20.86	0	0	1615	363.0	3.0805 E-3	1.2128 E-4
.3747	21.47	.447	.0176	1615	363.0	2.6449 E-3	1.0413 E-4
.3876	22.21	.986	.0388	1615	363.0	2.1788 E-3	.8578 E-4
.4000	22.92	1.506	.0593	1615	363.0	1.6759 E-3	.6598 E-4
.4121	23.61	2.012	.0792	1615	363.0	1.1430 E-3	.4500 E-4
.4237	24.28	2.497	.0983	1615	363.0	.5906 E-3	.2325 E-4
.4350	24.92	2.969	.1169	1615	363.0	0	0
.4458	25.54	3.419	.1346	1508	339.0	.5486 E-3	.2160 E-4
.4557	26.11	3.830	.1508	1280	287.7	2.2423 E-3	.8828 E-4
.4645	26.61	4.199	.1653	1077	272.2	3.9675 E-3	1.5620 E-4
.4723	27.06	4.526	.1782	896.7	201.6	5.6223 E-3	2.2135 E-4
.4793	27.46	4.818	.1897	735.3	165.3	7.1742 E-3	2.8245 E-4
.4855	27.82	5.077	.1999	592.5	133.2	8.6347 E-3	3.3995 E-4
.4909	28.13	5.304	.2088	467.5	105.1	9.9865 E-3	3.9317 E-4
.4956	28.40	5.502	.2166	359.3	80.77	1.1211 E-2	4.4138 E-4
.4997	28.63	5.669	.2232	265.0	59.57	1.2308 E-2	4.8455 E-4
.5031	28.83	5.812	.2288	186.2	41.87	1.3259 E-2	5.2201 E-4
.5059	28.99	5.928	.2334	121.7	27.35	1.4067 E-2	5.5380 E-4
.5080	29.11	6.017	.2369	73.21	16.46	1.4717 E-2	5.7940 E-4

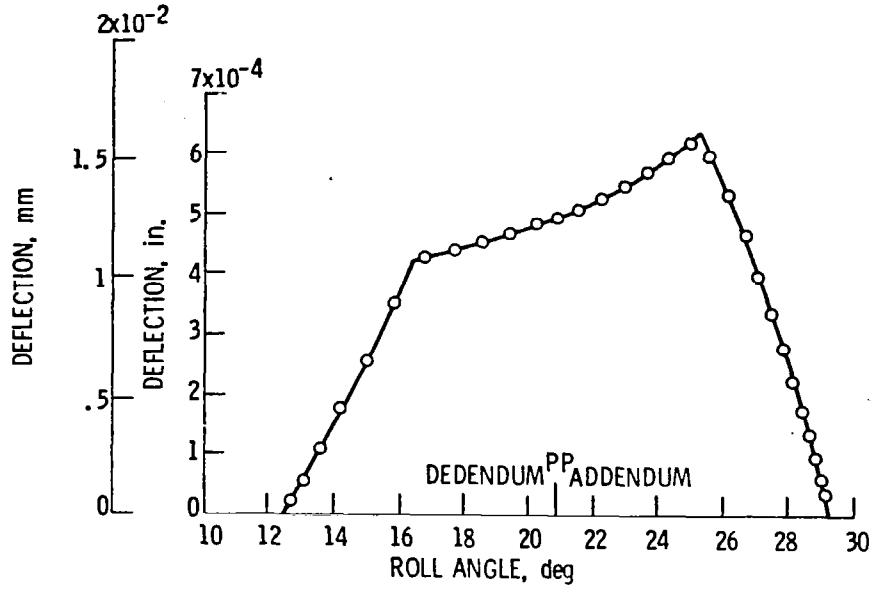

FIG. 13. PROFILE MODIFICATION FOR APPROXIMATE MINIMIZATION OF VIBRATION EXCITATION. [FROM TOOTH DEFLECTION CURVE GIVEN IN REF. 18.]

Transmission Error Dynamic Increment Functions

In the section devoted to the response, we found that the dynamic contributions of the static transmission error to the mesh and bearing support force spectrum, and to the force on a single tooth, all are governed by the functions $Q_{II}(\omega)$ and $Q_{I\ II}(\omega)$, where, in general, $Q_{ij}(\omega)$ represents the *dynamic* contribution to the transmission error complex harmonic amplitude at mesh i from a unit-amplitude harmonic component of the static transmission error at mesh j. Here, either subscript i or j can represent either mesh I or mesh II, where in the foregoing, we have been concerned mainly with the case i = I. See, for example, Eqs. (3.7), (3.8), and (3.11), and Eqs. (3.31), (3.33), and (3.34). The "transfer functions" $Q_{ij}(\omega)$ are properties only of the gearing structure — we have designated them "transmission error dynamic increment functions" since each function $Q_{ij}(\omega)$ tends to zero as $\omega \to 0$.

For the four-square test apparatus under study, expressions for $Q_{II}(\omega)$ in terms of basic system parameters are given by Eqs. (2.51), (2.55), (2.57), and (2.58), and expressions for $Q_{I\ II}(\omega)$ are given by Eqs. (2.52), (2.56), (2.57), and (2.59). Asymptotic low-frequency approximations for $Q_{II}(\omega)$ and $Q_{I\ II}(\omega)$ are given by Eqs. (2.62) and (2.65) respectively, and asymptotic high-frequency approximations for $Q_{II}(\omega)$ and $Q_{I\ II}(\omega)$ are given by Eqs. (2.64) and (2.66) respectively. Functions $Q_{II}(\omega)$ and $Q_{I\ II}(\omega)$ are, in general, complex.

The basic system parameters required to evaluate the above expressions have been carefully evaluated and are:

$$I_1 = .004112 \text{ N-m-sec}^2 \ (.0364 \text{ lb-in-sec}^2)$$

$$I_2 = .0008010 \text{ N-m-sec}^2 \ (.00709 \text{ lb-in-sec}^2)$$

$$I_3 = .002994 \text{ N-m-sec}^2 \ (.0265 \text{ lb-in-sec}^2)$$

$$R \equiv R_b = .0417693 \text{ m } (1.64446 \text{ in}).$$

$$\bar{C}_I = 1.26312 \times 10^{-8} \text{ m/N } (2.21195 \times 10^{-6} \text{ in/lb})$$

$$\bar{C}_{II} = 2.10520 \times 10^{-9} \text{ m/N } (3.68659 \times 10^{-7} \text{ in/lb}). \qquad (5.5)$$

Values of the damping constants c_1, c_2, c_3, and c_a have been chosen by assuming* that the damping coefficients of all four

*Private communication with Dr. John J. Coy.

bearings in the test rig are the same, where the mesh damping is included in the bearing damping coefficients. The bearing damping is then specified by the fraction of critical damping ζ_1 in the test gear-shaft-slave gear degree-of-freedom on the side of the unit opposite to the loading-vane; the loading-vane damping coefficient c_a is specified by assuming a value for the fraction of critical damping ζ_3 in the slave gear degree-of-freedom on the loading-vane side of the unit, which includes the slave gear bearing damping and the damping associated with relative motion in the loading-vane. Expressions for ζ_1 and ζ_3 are readily determined from Eqs. (2.19) and (2.21) as

$$\zeta_1 = \frac{c_1}{2\sqrt{k_1 I_1}} \quad , \quad \zeta_3 = \frac{c_3 + c_a}{2\sqrt{k_3 I_3}} \quad , \tag{5.6a,b}$$

where

$$k_1 = R^2[(\bar{C}_I)^{-1} + (\bar{C}_{II})^{-1}] \quad , \quad k_3 = R^2(\bar{C}_{II})^{-1} \quad , \tag{5.7a,b}$$

from which we obtain

$$c_1 = 2\zeta_1 \sqrt{k_1 I_1} \quad , \quad c_a = (2\zeta_3 \sqrt{k_3 I_3}) - c_3 \quad , \tag{5.8a,b}$$

and

$$c_2 = c_3 = \frac{1}{2}c \quad . \tag{5.9}$$

This last expression is a consequence of the assumption of equal bearing damping coefficients and the fact that c_1 represents the damping of two bearings, whereas c_2 and c_3 represent the damping of only a single bearing each. Assuming* values of $\zeta_1 = 0.1$ and $\zeta_3 = 0.5$ yields, from Eqs. (5.5) through (5.9), the following damping constants:

$$\begin{aligned} c_1 &= 12.6114 \text{ N-m-sec } (111.626 \text{ lb-in-sec}) \\ c_2 &= c_3 = 6.30571 \text{ N-m-sec } (55.8130 \text{ lb-in-sec}) \\ c_a &= 43.5062 \text{ N-m-sec } (385.081 \text{ lb-in-sec}). \end{aligned} \tag{5.10}$$

*Private communication with Dr. John J. Coy.

The above cited expressions for the two transmission error dynamic increment functions $Q_{II}(\omega)$ and $Q_{I\ II}(\omega)$ and their low- and high-frequency asymptotic approximations have been evaluated using the above cited numerical constants, and are plotted in Figs. 14 through 17. Figure 14 displays the magnitude of $Q_{II}(\omega)$ and the magnitude of the low- and high-frequency asymptotic approximations of $Q_{II}(\omega)$, Fig. 15 displays these same metrics for the magnitude of $Q_{I\ II}(\omega)$, Fig. 16 displays the real and imaginary parts of $Q_{II}(\omega)$ and its asymptotic approximations, and Fig. 17 displays the comparable quantities for $Q_{I\ II}(\omega)$.

The test apparatus shown in Fig. 1 has three degrees of freedom; however, one of these must be considered to be degenerate due to the absence of an elastic restraint on steady rotation of the system. Consequently, we would expect to see two resonant frequencies for such a system. Figures 14 and 15 show one resonant frequency in the neighborhood of about 3500 Hz, but no second resonance is apparent in these figures. This second resonance does not show up because of the relatively large value ($\zeta_3 = 0.5$) of damping assumed for relative motion in the loading-vane. Choice of a smaller value for ζ_3 shows a second resonance in the approximate neighborhood of 2000 Hz.

The nominal running speed of the test apparatus is 10,000 rpm. Thus, the tooth meshing frequency of the 28 tooth test gears is

$$f_I = \frac{10,000}{60} \times 28 = 4666.67 \text{ Hz}, \tag{5.11}$$

and the tooth meshing frequency of the 35 tooth slave gears is

$$f_{II} = \frac{10,000}{60} \times 35 = 5833.33 \text{ Hz} . \tag{5.12}$$

Examination of Fig. 14 shows that f_I is beyond both system resonant frequencies, and is in the region where the high-frequency asymptotic formula for $Q_{II}(\omega)$ given by Eq. (2.64) provides quite accurate results. Examination of Fig. 15 shows that f_{II} also is beyond both resonant frequencies, but the high-frequency asymptotic formula, Eq. (2.66), provides only marginal accuracy for $Q_{I\ II}(\omega)$ in the neighborhood of $f_{II} = 5833$ Hz.

Further examination of Fig. 14 shows that for $f_I = 4667$ Hz and all of its multiples, $|Q_{II}(\omega)|$ is approximately unity indicating that dynamic effects are playing an important part at all of the test gear tooth-meshing harmonic frequencies. On the other hand, examination of Fig. 15 shows that for $f_{II} = 5833$ Hz and

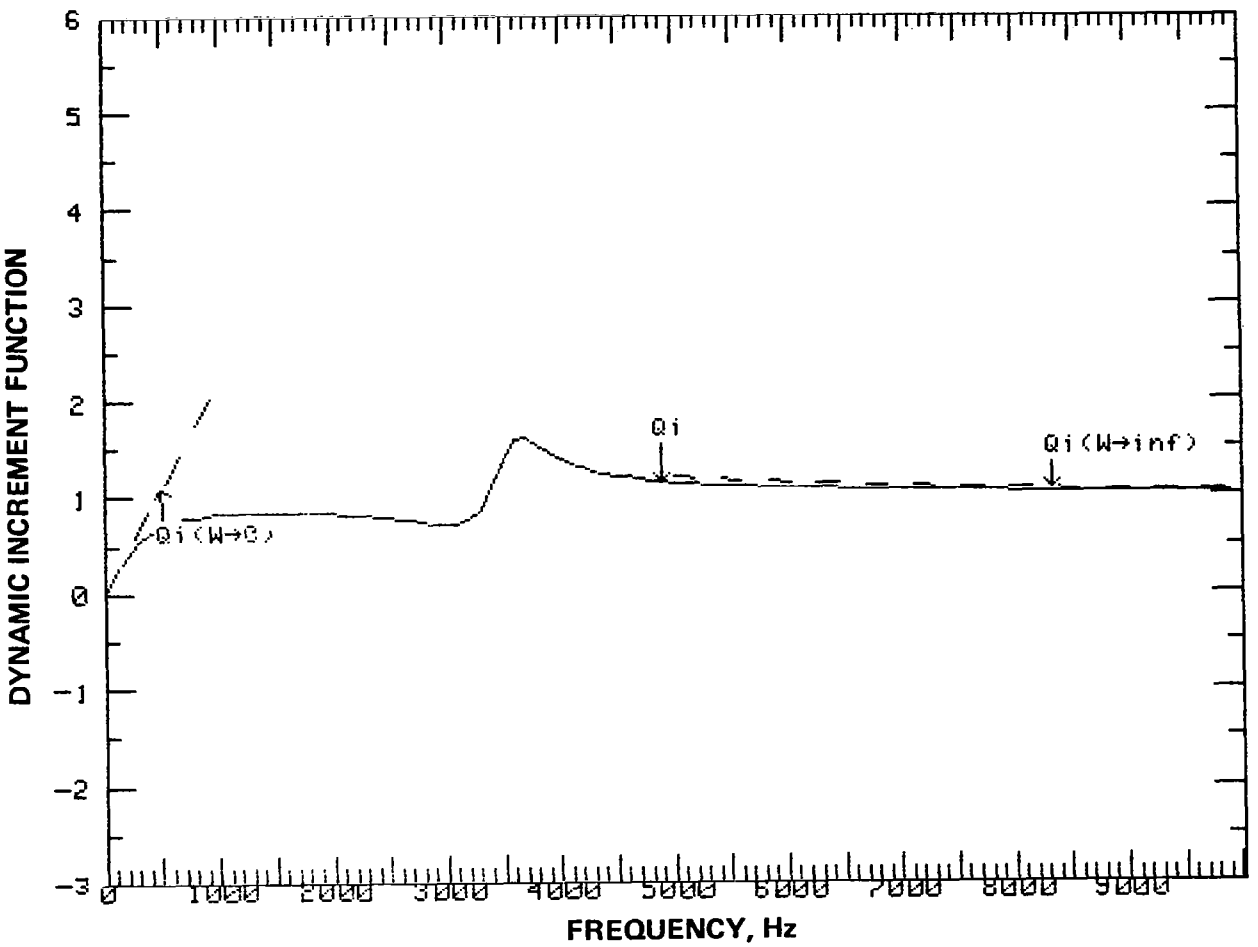

FIG. 14. MAGNITUDE OF TRANSMISSION ERROR "AUTO" DYNAMIC INCREMENT FUNCTION $Q_{II}(\omega)$ AND ITS ASYMPTOTIC FORMS.

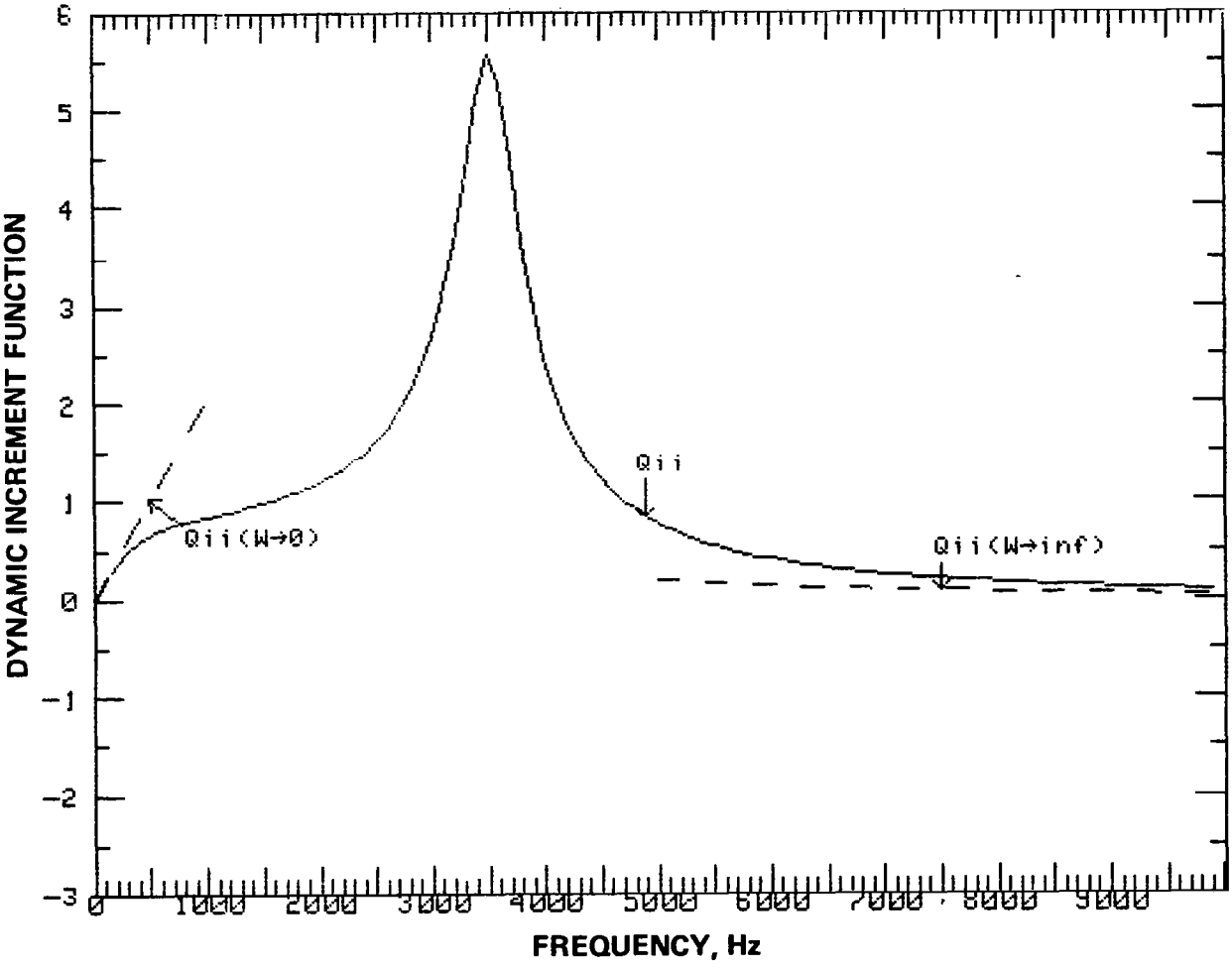

FIG. 15. MAGNITUDE OF TRANSMISSION ERROR "CROSS" DYNAMIC INCREMENT FUNCTION $Q_{I\ II}(\omega)$ AND ITS ASYMPTOTIC FORMS.

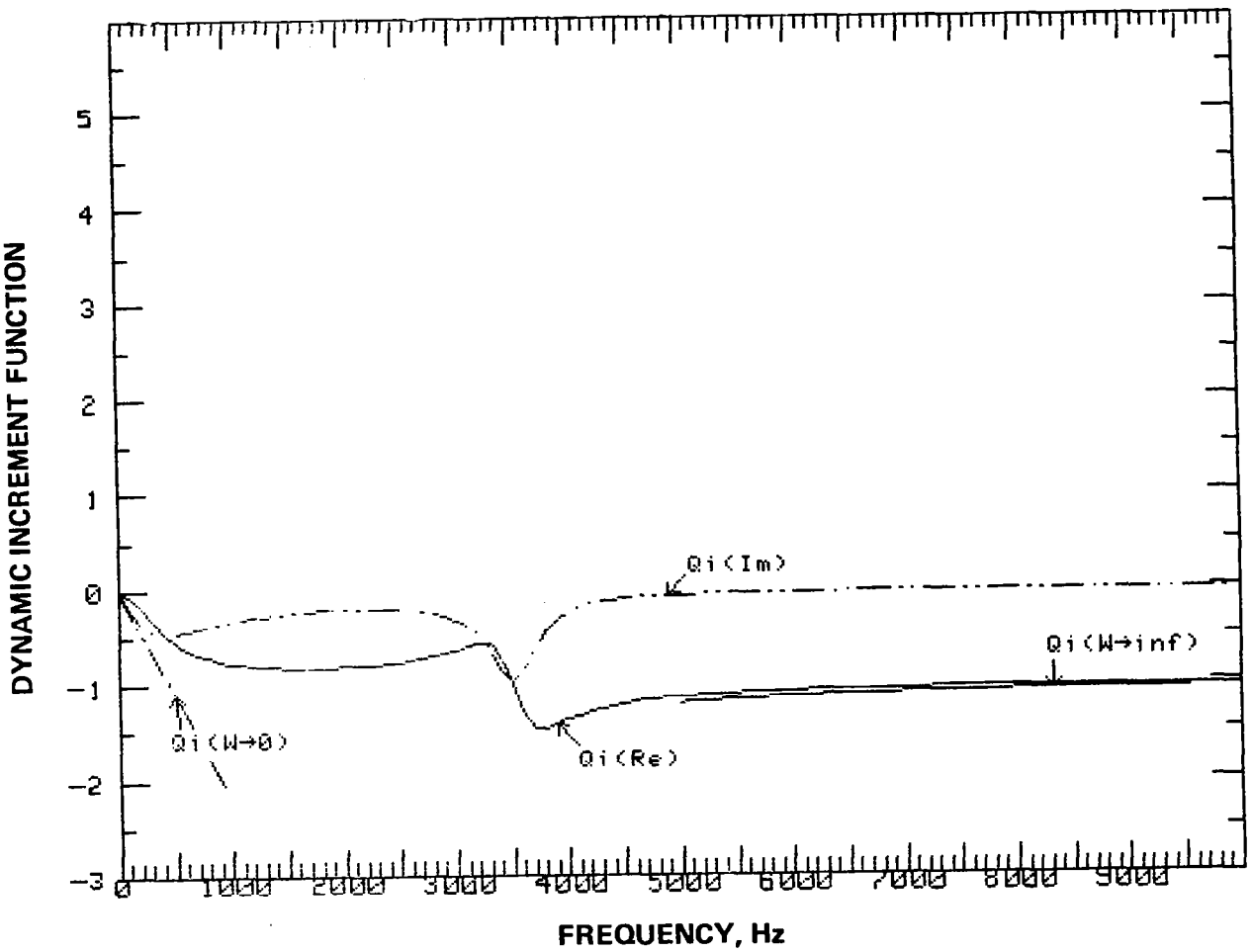

FIG. 16. REAL AND IMAGINARY PARTS OF TRANSMISSION ERROR "AUTO" DYNAMIC INCREMENT FUNCTION $Q_{II}(\omega)$ AND ITS ASYMPTOTIC FORMS.

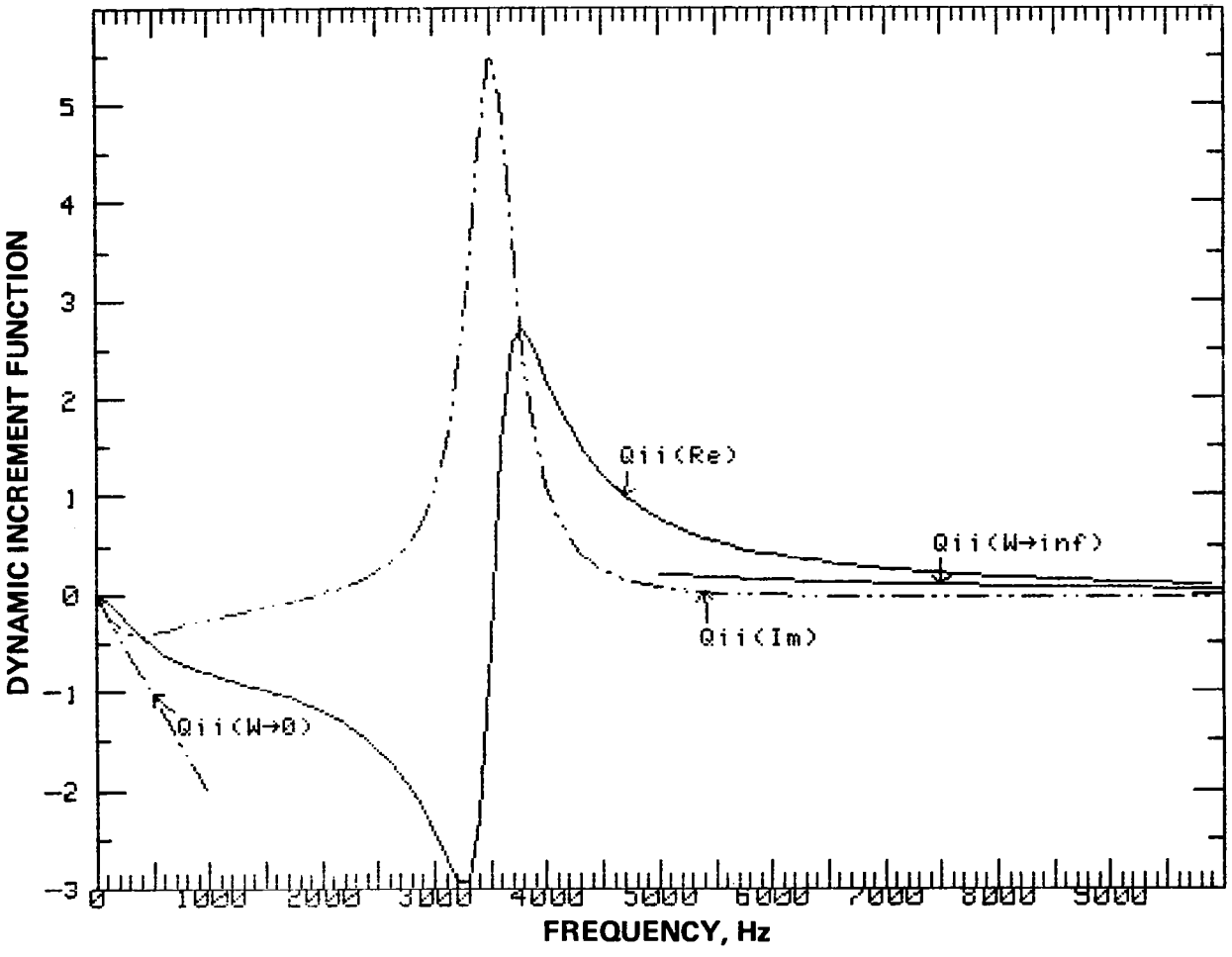

FIG. 17. REAL AND IMAGINARY PARTS OF TRANSMISSION ERROR "CROSS" DYNAMIC INCREMENT FUNCTION $Q_{I\ II}(\omega)$ AND ITS ASYMPTOTIC FORMS.

beyond, $|Q_{I\ II}(\omega)|$ is not very different from zero, indicating that at the 10,000 rpm testing speed, the tooth-meshing harmonics of the static transmission error of the slave gears have little effect on the dynamic transmission error of the test gears. However, if the test apparatus rpm were reduced to about 6000 rpm, Fig. 15 shows that a very substantial *magnification* of the *slave* gear static transmission error tooth meshing fundamental would be added to the *test* gear dynamic transmission error. See Eq. (3.17). *This magnification factor, which is about 5.6, provides dramatic illustration of the very substantial errors that can be introduced by the common practice of modeling gearing systems with more than one mesh by simple uncoupled single mesh systems.*

Mesh and Bearing-Support Force Spectrum

In the remaining portion of this report, we illustrate the theory developed in the preceding portions with computations made for two sets of test gears: one set possesses perfect involute profiles except for linear tip relief that starts at the highest point of single tooth contact and extends to the tip of the tooth; the second set possesses the approximately optimum profile modification defined by Eq. (5.4), where the tooth loading function $W_j(x)$ used is illustrated in Fig. 12. Thus, the teeth of this second gear set have additions of material to the perfect involute profiles, where the added depths are equal to the values of the deflections given in Table 1. Linear interpolation was used to define the values of these profile modifications between the values given in Table 1 – except for the points on either side of the slope discontinuities shown in Fig. 13. Additional points were added at the locations of these slope discontinuities that were computed by linear extrapolation of pairs of points on either side of the discontinuities shown in Fig. 13. These two additional points are:

Roll angle		"Deflection"	
rad	deg	mm	in
.2872	16.46	1.0772 E-2	4.2409 E-4
.4408	25.26	1.5984 E-2	6.2929 E-4.

The above values can be thought of as added entries to Table 1.

The amount of tip relief used in the linear tip relief test gear calculations was .01524 mm (.0006 in) which was specified at a radial position of the addendum radius minus the tip rounding radius of .381 mm (.015 in).

The first step in determining the mesh and bearing-support force spectrum, Eq. (3.11), is computation of the sets of Fourier series coefficients α_{mnI} and α_{mnII}, $n = \pm 1, \pm 2, \cdots$ of the static transmission errors of the test gears (mesh I) and those of the slave gears (mesh II) for use in Eqs. (3.7) and (3.8). The tooth profiles of the slave gears are *unmodified* involute profiles. The sets of static transmission error Fourier series coefficients, Eq. (1.5), were computed using the general methods outlined in Sec. 1 of this report. Each set of Fourier series coefficients was then multiplied by $(\overline{C}_I)^{-1}$ times the appropriate dynamic increment function as indicated by Eqs. (3.7) and (3.8) to yield the test gear mesh and bearing-support force Fourier series coefficients arising from the test gear and slave gear static transmission error excitations. The dynamic increment functions used were those illustrated in Figs. 14 through 17. The test gear mesh and bearing-support force Fourier series coefficients $\alpha_{WII}(n)$ and $\alpha_{WI\ II}(n)$ that arise from the static transmission errors of the test and slave gear meshes respectively were then combined as in Eq. (3.11) with the d-c torque τ_a and base circle radius R of the test gears to yield the test gear mesh and bearing-support force (line) spectrum. Frequencies f_I and f_{II} are the tooth meshing frequencies of the test and slave gears respectively.

Figure 18 shows the (one-sided) line spectrum of the dynamic loads experienced by the test gear mesh and bearings that arises from the test gear static transmission error, and that is expressed by the *first line* of Eq. (3.11). The spectrum shown in Fig. 18 is for the above-mentioned test gear set with linear tip relief. Figure 19 shows the comparable spectrum for the test gear set with the approximately optimum profile modification shown in Fig. 13. The line spacing in each of Figs. 18 and 19 is the frequency spacing of the test gear tooth meshing harmonics, which is 4666.67 Hz according to Eq. (5.11). Each plot shows a d-c component on the ordinate with strength marked by an × and 64 additional lines, which was the total number of harmonics computed by the computer program. The abscissa is measured in Hertz and the (logarithmic) ordinate is measured in $(lb)^2$.

The value of the d-c component indicated by the × is the same in each spectrum shown in Figs. 18 and 19. This value is $(\tau_a/R)^2 = (363)^2 = 131{,}769\ (lb)^2$. However, careful inspection of the remaining lines shows that those of Fig. 18 are typically about 10^3 stronger than those of Fig. 19 corresponding to (linear) forces in Fig. 19 of about $\sqrt{10^{-3}}$ or 3% to 4% of those in Fig. 18. In fact, since the tooth optimum profile modification is supposed to exactly compensate for the static transmission error, the strengths of all lines in Fig. 19 except the d-c component should theoretically be zero. This did not happen exactly because

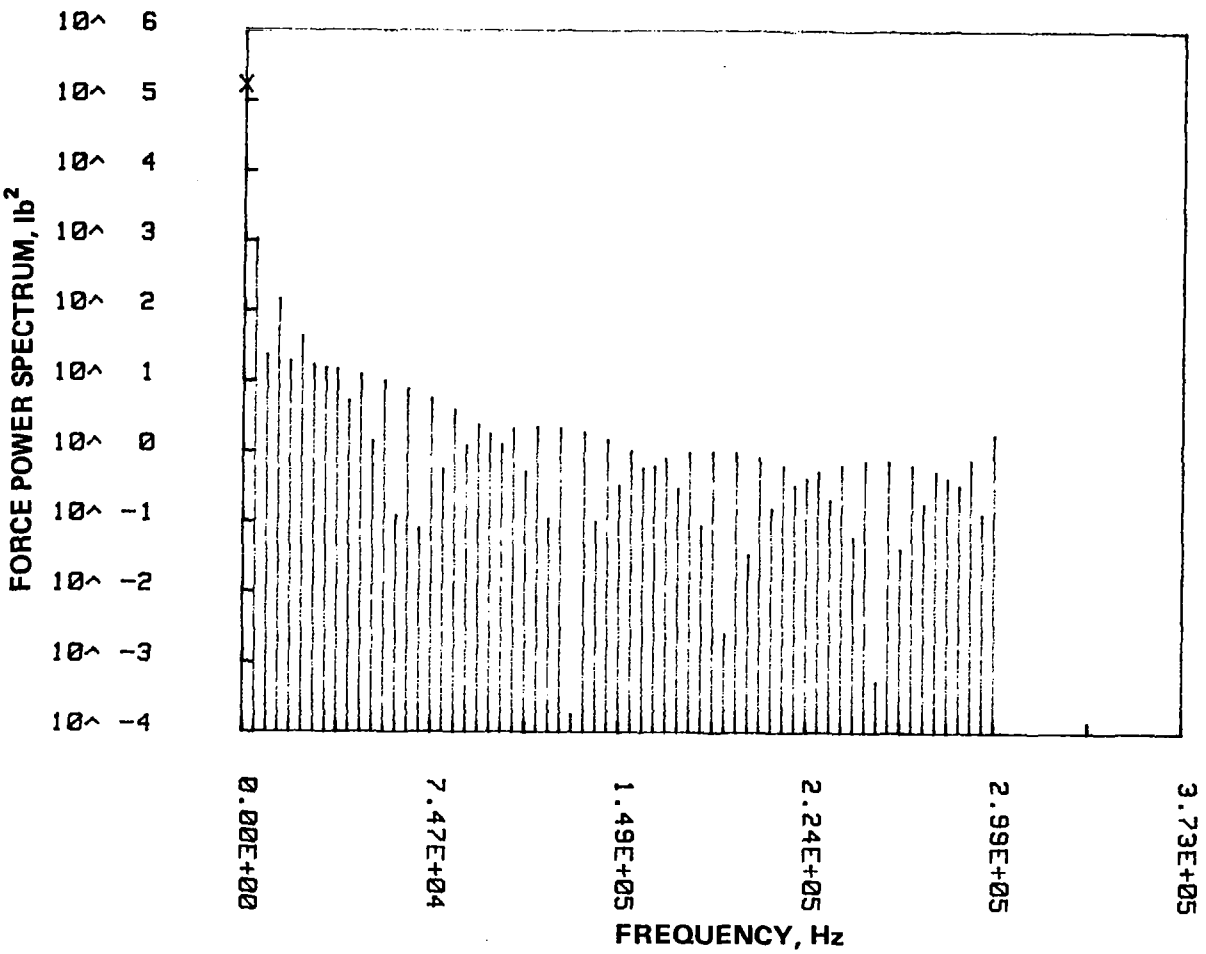

FIG. 18. PREDICTED CONTRIBUTION FROM TEST GEAR MESH STATIC TRANSMISSION ERROR TO (ONE-SIDED) FORCE POWER SPECTRUM OF TEST GEAR MESH AND BEARING SUPPORTS FOR CASE OF LINEAR TIP RELIEF OF TEST GEARS. [FIRST LINE OF EQ. (3.11).]

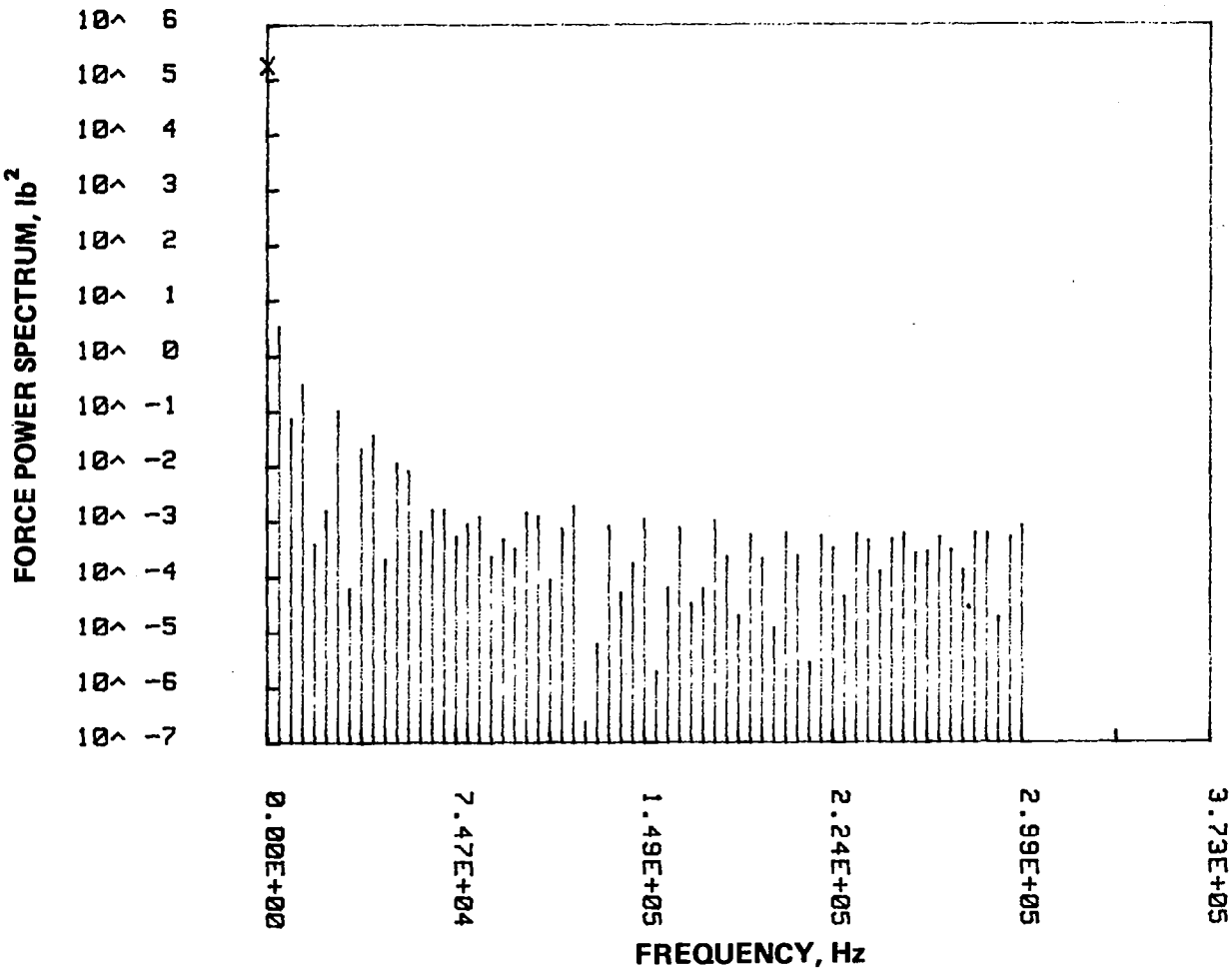

FIG. 19. PREDICTED CONTRIBUTION FROM TEST GEAR MESH STATIC TRANSMISSION ERROR TO (ONE-SIDED) FORCE POWER SPECTRUM OF TEST GEAR MESH AND BEARING SUPPORTS FOR CASE OF APPROXIMATELY OPTIMUM PROFILE MODIFICATION OF TEST GEARS. [FIRST LINE OF EQ. (3.11).]

we modeled the single tooth compliance by a *least-squares cubic polynomial fit* to the compliance values computed from the data shown in Table 1, whereas we took the profile modifications directly from the numerical values shown in Table 2 — giving rise to a small discrepancy between the compliance values and deflection values caused by the small "errors" in the cubic polynomial fit. However, such force spectrum reductions shown by comparison of Figs. 19 and 18 might be typical of what we could *hope* to achieve with the optimum design procedure indicated by Eqs. (4.6a) and (4.6b). We would not expect to do this well in practice with the approximate optimum design given by Eq. (5.4), which neglects deflections of all teeth except the loaded tooth.

Figures 20 and 21 are plots of the contributions of the second line in Eq. (3.11) to the mesh and bearing support force spectra. Figure 20 provides that contribution in the case of the test gears with linear tip relief, and Fig. 21 provides the comparable contribution in the case of the test gears with the approximately optimum profile modifications prescribed by Table 2. The line spacing in each of Figs. 20 and 21 is the frequency spacing of the slave gear tooth meshing harmonics which is 5833.33 Hz, according to Eq. (5.12). The abscissa of Figs. 20 and 21 is measured in units of Hertz and the (logarithmic) ordinate is measured in units of $(1b)^2$.

The line spectra shown in Figs. 20 and 21 possess no d-c component. This lack of a d-c component is a result of the fact that $Q_{I\ II}(\omega) = 0$ at $\omega = 0$ as can be seen from Fig. 15 — which results in $\alpha_{WI\ II}(0) = 0$ according to Eq. (3.8).

According to Eqs. (3.8) and (3.11), the strengths of the lines in Figs. 20 and 21 should depend on the time-average value of the compliance of mesh I, $\bar{C}_I$, the transmission error "cross" dynamic increment function $Q_{I\ II}(\omega)$ shown in Fig. 15, and the Fourier series coefficients α_{mnII} of the static transmission error of (slave) gear mesh II. Since the slave gears had no profile modifications, their static transmission error arises only from their elastic deformations. The Fourier series coefficients of the elastic deformation component of the static transmission error is given by Eq. (1.8) — they are determined essentially by the Fourier series coefficients $\alpha_{(1/K)n}$, $n = 0,\pm1,\pm2,\cdots$ of the instantaneous reciprocal of the total stiffness of mesh II. For the slave gears of mesh II, these Fourier series coefficients were taken to be one-sixth of those for the test gears of mesh I (because the width of the slave gears is six times that of the test gears). Since the roll distance L of the test gears with linear tip relief differs somewhat from the design roll distance L for the test gears with (approximately) optimum profile modifications, the temporal behavior of the test gear instantaneous total mesh stiffness differs slightly

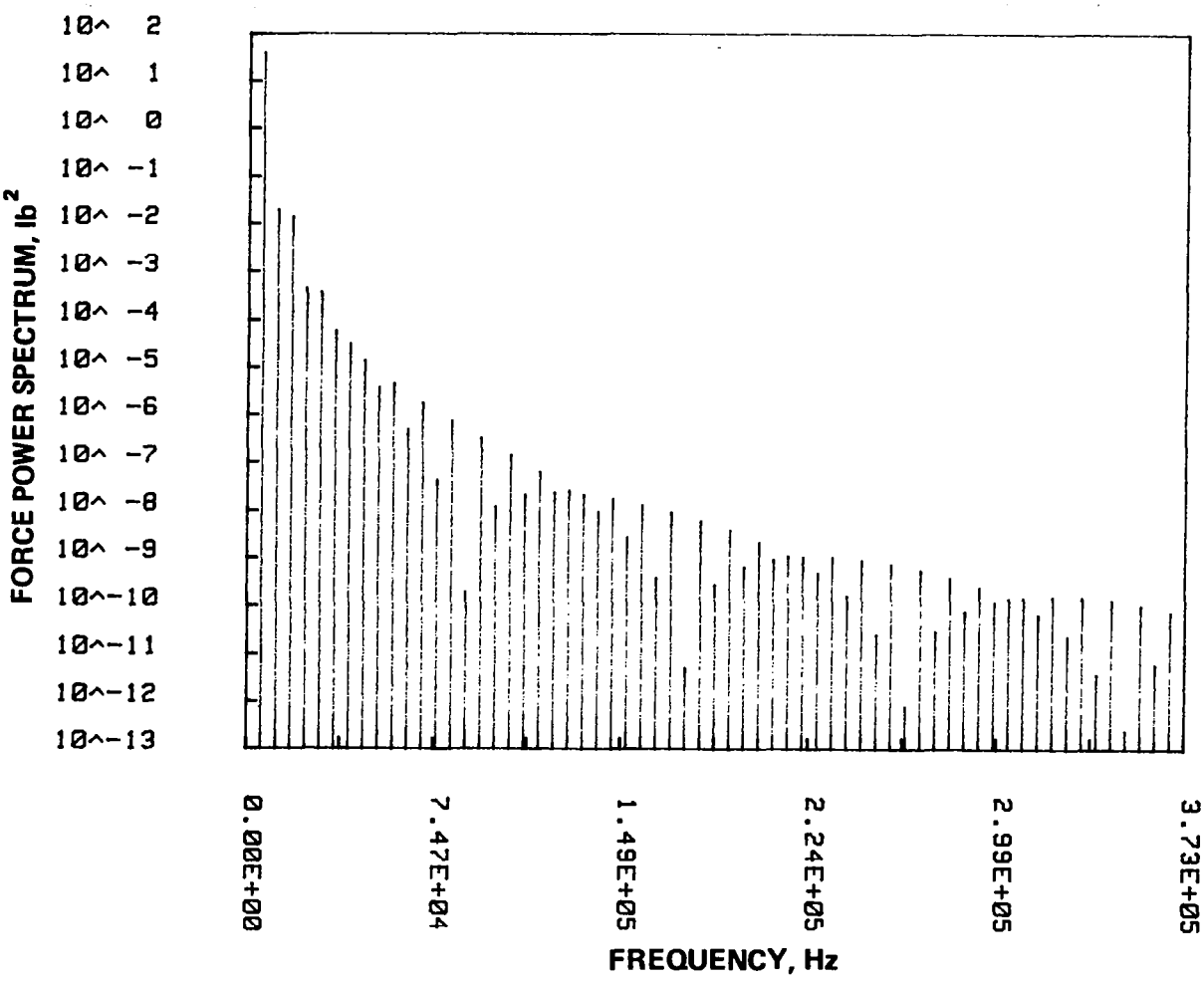

FIG. 20. PREDICTED CONTRIBUTION FROM SLAVE GEAR MESH STATIC TRANSMISSION ERROR TO (ONE-SIDED) FORCE POWER SPECTRUM OF TEST GEAR MESH AND BEARING SUPPORTS FOR CASE OF LINEAR TIP RELIEF OF TEST GEARS. [SECOND LINE OF EQ. (3.11).]

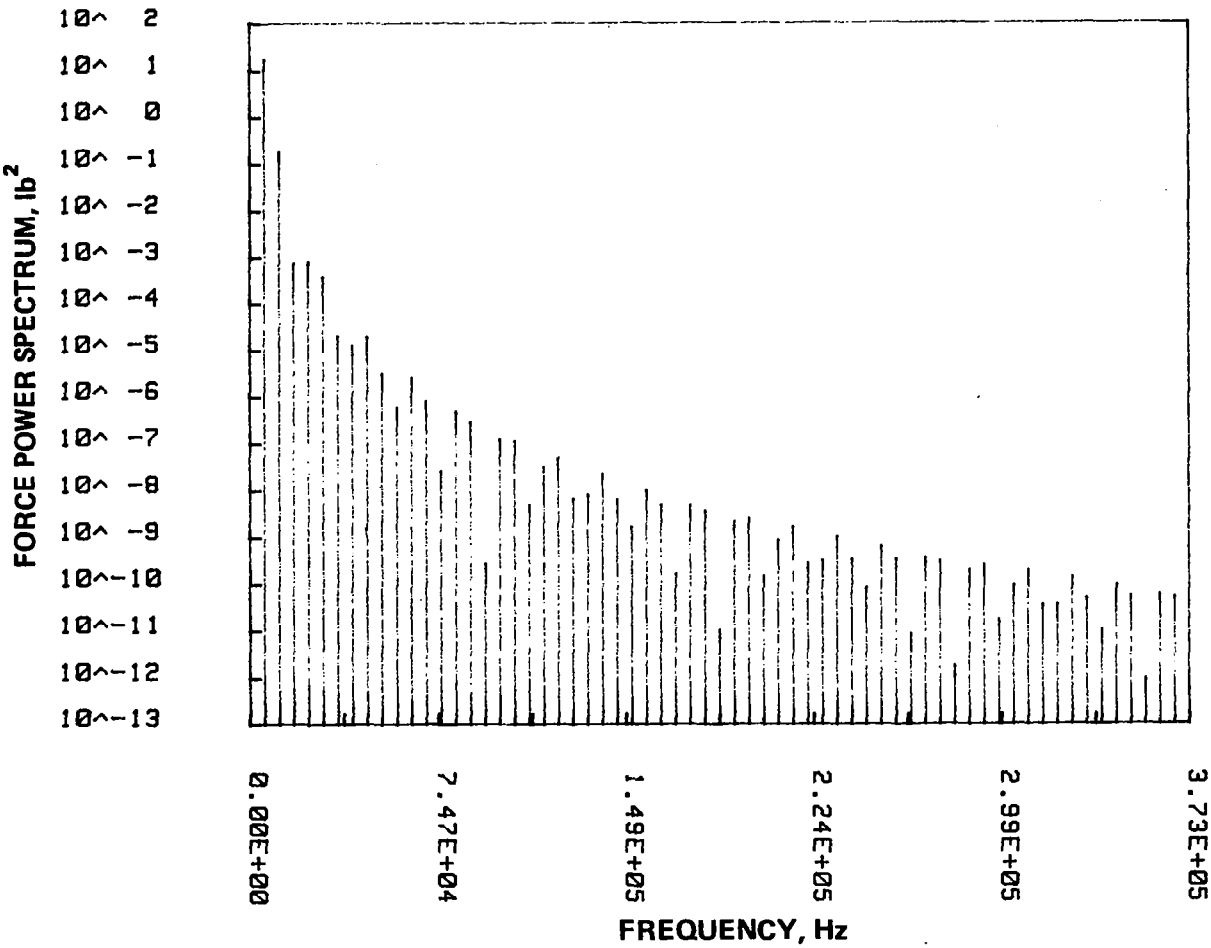

FIG. 21. PREDICTED CONTRIBUTION FROM SLAVE GEAR MESH STATIC TRANSMISSION ERROR TO (ONE-SIDED) FORCE POWER SPECTRUM OF TEST GEAR MESH AND BEARING SUPPORTS FOR CASE OF APPROXIMATELY OPTIMUM PROFILE MODIFICATION OF TEST GEARS. [SECOND LINE OF EQ. (3.11).]

for these two cases — hence, our predictions of the slave gear contributions to the test gear mesh and bearing-support force spectra shown in Figs. 20 and 21 also differ slightly for these two cases.

From Eqs. (3.7), (3.8), and (3.11), we see that the transmission error "auto" dynamic increment function $Q_{II}(\omega)$ of Fig. 14 is the structural transfer function that governs the force spectrum component given by the first line in Eq. (3.11), whereas the transmission error "cross" dynamic increment function $Q_{I\ II}(\omega)$ of Fig. 15 is the structural transfer function that governs the force spectrum component given by the second line in Eq. (3.11). In the frequency range beyond 4666 Hz where all test gear tooth-meshing harmonics fall, we see from Fig. 14 that $|Q_{II}(\omega)| \approx 1$, whereas in the frequency range beyond 5833 Hz where all slave gear tooth meshing harmonics fall, we see from Fig. 15 that $|Q_{I\ II}(\omega)| << 1$. This difference in the structural transfer functions is the main reason why the slave gear contribution of Fig. 20 to the test gear force spectrum is much less than the test gear "auto" contribution shown in Fig. 18 for the linear tip relief case. However, in the case of the approximately optimum profile modification, the first two slave gear tooth meshing harmonic contributions shown in Fig. 21 are stronger than those from the test gear shown in Fig. 19 because of the reduction of the test gear contributions arising from the approximately optimum profile modification.

Dynamic Force on a Single Tooth

The dynamic increment $\delta W^{\dagger}_{Ij}(t)$ of the force history on a single tooth given by Eq. (3.31) can be decomposed into two components

$$\delta W^{\dagger}_{Ij}(t) = \delta W^{\dagger}_{IjI}(t) + \delta W^{\dagger}_{IjII}(t) , \tag{5.13}$$

where we have defined

$$\delta W^{\dagger}_{IjI}(t) \triangleq K^{\dagger}_{Sj}(t)\ \delta\zeta^{\dagger}_{mII}(t) \tag{5.14}$$

and

$$\delta W^{\dagger}_{IjII}(t) \triangleq K^{\dagger}_{Sj}(t)\ \delta\zeta^{\dagger}_{mI\ II}(t) , \tag{5.15}$$

where the notation on the right-hand sides of Eqs. (5.14) and (5.15) is the same as that on the right-hand side of Eq. (3.31). That is, $K^{\dagger}_{Sj}(t)$ is the instantaneous stiffness of a typical pair of test gear teeth, and $\delta\zeta^{\dagger}_{mII}(t)$ and $\delta\zeta^{\dagger}_{mI\ II}(t)$ are the *dynamic* increments of the transmission error of the test gear mesh arising from the test gears and slave gears as given by Eqs. (3.33) and (3.34) respectively. From Eqs. (3.29), (3.31), and (5.13) through (5.15),

we can represent the dynamic force $W^{\dagger}_{Ij}(t)$ on a single tooth of the test gear mesh as

$$W^{\dagger}_{Ij}(t) = \left[W^{\dagger}_{Ij_0}(t) + \delta W^{\dagger}_{IjI}(t)\right] + \delta W^{\dagger}_{IjII}(t) \ . \qquad (5.16)$$

The first two terms within the brackets in the right-hand side of Eq. (5.16) constitute tht total contribution to the single tooth force $W^{\dagger}_{Ij}(t)$ arising from the static transmission error excitation by the *test* gear mesh, whereas the third term $\delta W^{\dagger}_{IjII}(t)$ in the right-hand side of Eq. (5.16) is the contribution to $W^{\dagger}_{Ij}(t)$ from the static transmission error excitation by the *slave* gear mesh.

Figure 22 shows the predicted total force contribution $[W^{\dagger}_{Ij_0}(t)+\delta W^{\dagger}_{IjI}(t)]$ on a typical tooth of the *driving* test gear arising from the static transmission error excitation by the test gear mesh. The rotational speed of the NASA Lewis four-square test apparatus used in the computation was 10,000 rpm. The test gear mesh carries a mean loading τ_a/R of 1615 N (363 lbs). The force history shown in Fig. 22 is for the test gears with linear tip relief of .01524 mm (.0006 in) as described earlier in this report.

The ordinate of Fig. 22 is force in units of pounds, and the abscissa is time in seconds. The time origin t = 0 is located at the pitch point which corresponds to the center position of the time axis. Contact initiation occurs at the base of the tooth at $t = -1.57\times10^{-4}$ sec and terminates at the tip at $t = 1.57 \times 10^{-4}$ sec.

At the instant of contact initiation, the tooth abruptly picks up a loading of 98.5 lb as is indicated in Fig. 22. This abrupt loading of the base occurs because the tip of the tooth of the mating gear has *too little modification* to allow a smooth onset of loading of the tooth base at contact initiation. The loading on the tooth thereupon increases in an approximately linear fashion from the instant of contact initiation through the interval of two-tooth contact until the instant where the discontinuity in slope occurs and where the rate of loading increase abruptly diminishes. Beyond this instant, where the force on the tooth is approximately a constant value of 338 lb, is the region of single tooth pair contact. The loading on the tooth thereupon decreases in an approximately linear fashion again until contact terminates at the tip at $t = 1.57 \times 10^{-4}$ sec. At this instant, the loading on the tooth drops abruptly from 98.5 lb to zero as contact is lost.

Figure 22 indicates that the maximum loading carried by the tooth is 338 lb. This value is 25 lb less than the *static* loading of 363 lb carried by the tooth within the region of single tooth pair contact under static loading conditions. The reason for this

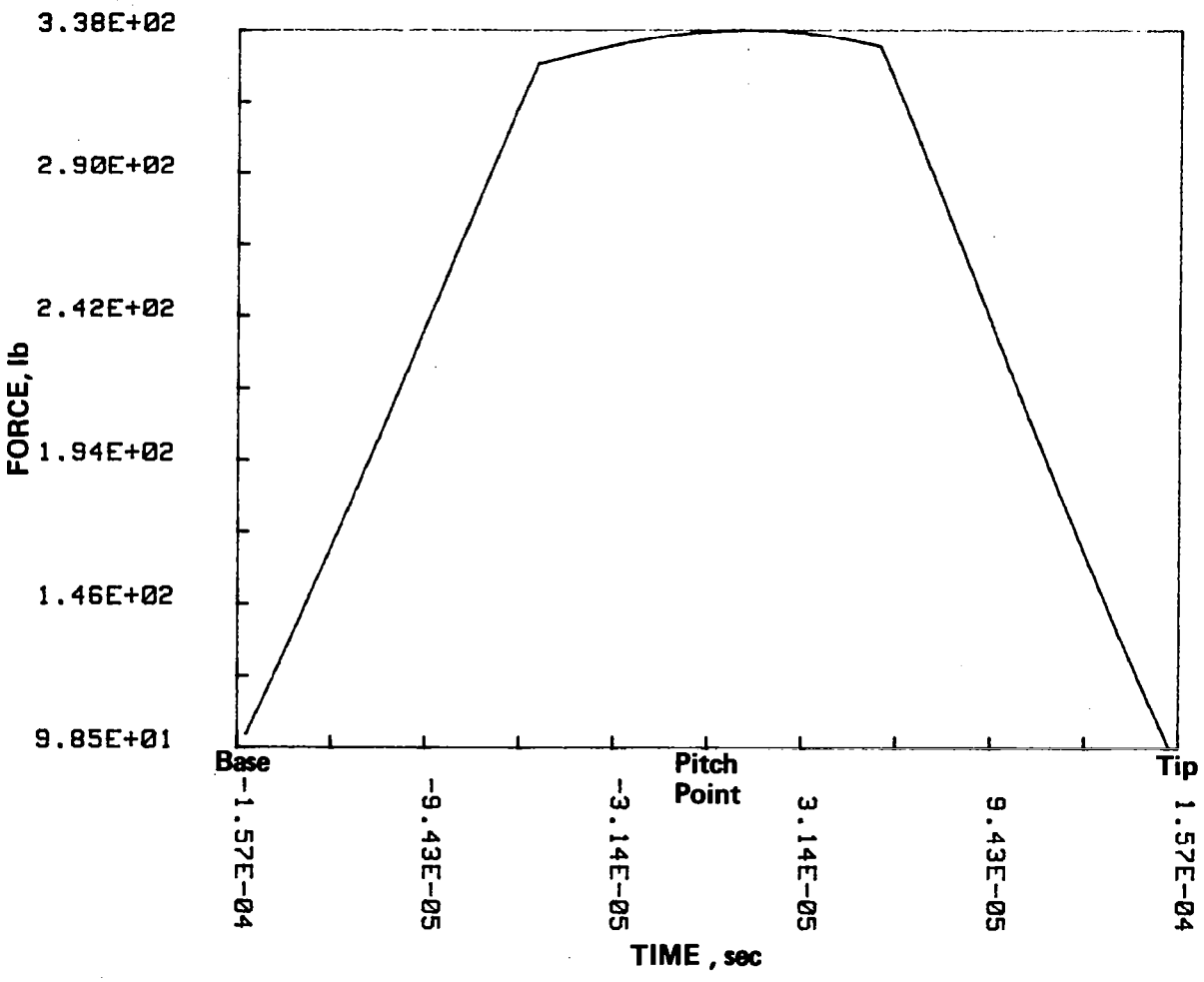

FIG. 22. PREDICTED FORCE HISTORY ON A TYPICAL DRIVING TEST GEAR TOOTH WITH LINEAR TIP RELIEF. ROTATIONAL SPEED IS 10,000 RPM. MESH CARRIES A NOMINAL LOADING OF 1615N (363 LB). TIP RELIEF IS .01524 MM (.0006 IN). FIGURE EXCLUDES EFFECTS OF DYNAMIC EXCITATION FROM SLAVE GEARS.

25 lb maximum loading decrease is that at the instant of maximum loading of 338 lb shown in Fig. 22, the dynamic loading increment $\delta W^{\dagger}_{IjI}(t)$ of Eq. (5.14) is -25 lb. This loading decrease arises from the dynamic transmission error increment $\delta\zeta^{\dagger}_{mII}(t)$ in Eq. (5.14) (which is negative in this case).

Physically, this decrease of 25 lb of maximum tooth loading arises from the undermodification of the tooth tips that results in the abrupt loading increments of 98.5 lb at contact initiation and termination as shown in Fig. 22. This "extra" loading carried in the two tooth-pair contact regions results in a reduced tooth loading within the region of single tooth-pair contact, which occurs because at a test speed of 10,000 rpm the inertia associated with the test gear masses prevents the teeth from picking up their full static loading of 363 lb within the single tooth-pair contact interval.

Figure 23 shows the force history $[W^{\dagger}_{Ij_0}(t)+\delta W^{\dagger}_{IjI}(t)]$ on a typical tooth of the *driving* test gear that is comparable to Fig. 22 – except that the force history shown in Fig. 23 was computed for test gears with the profile relief values shown in Table 2 (which was displayed earlier in this section). Force values $[W^{\dagger}_{Ij_0}(t)+\delta W^{\dagger}_{IjI}(t)]$ shown in Fig. 23 arise from the static transmission error excitation by the test gear mesh only, as can be seen from Eqs. (3.29), (3.30), (3.33), (5.13), and (5.14). For the case shown in Fig. 23, the rotational speed of the four-square test apparatus was 10,000 rpm and the mean loading τ_a/R carried by the test gears was 1615 N (363 lb), which are the same values as for the case shown in Fig. 22.

Contact initiation occurs at the base of the tooth at a value of $t = -1.41 \times 10^{-4}$ sec instead of $t = -1.57 \times 10^{-4}$ sec as in Fig. 22. This reduction in $|t|$ at contact initiation (and contact termination) shown in Fig. 23 occurs because of the slightly smaller *design value* of roll distance of L = 1.22971 cm (.48414 in) of the test gears of Fig. 23 [in comparison with L = 1.37450 cm (.5411406 in) for the test gears of Fig. 22]. In contrast to the case shown in Fig. 22, the tooth loading at the *instant* of contact initiation of $t = -1.41 \times 10^{-4}$ sec and contact termination $t = 1.41 \times 10^{-4}$ sec is zero for the case shown in Fig. 23. The initial value of 17.6 lb shown in Fig. 23 occurs at a value of $|t|$ somewhat smaller than $|t| = 1.41 \times 10^{-4}$ sec. The loading history between $|t| = 1.41 \times 10^{-4}$ sec and the first value of 17.6 lb shown in Fig. 23 is a linear extrapolation of the history shown in Fig. 23. This small region is missing from the figure because of an artifact of the computer plot routine used to plot Fig. 23.

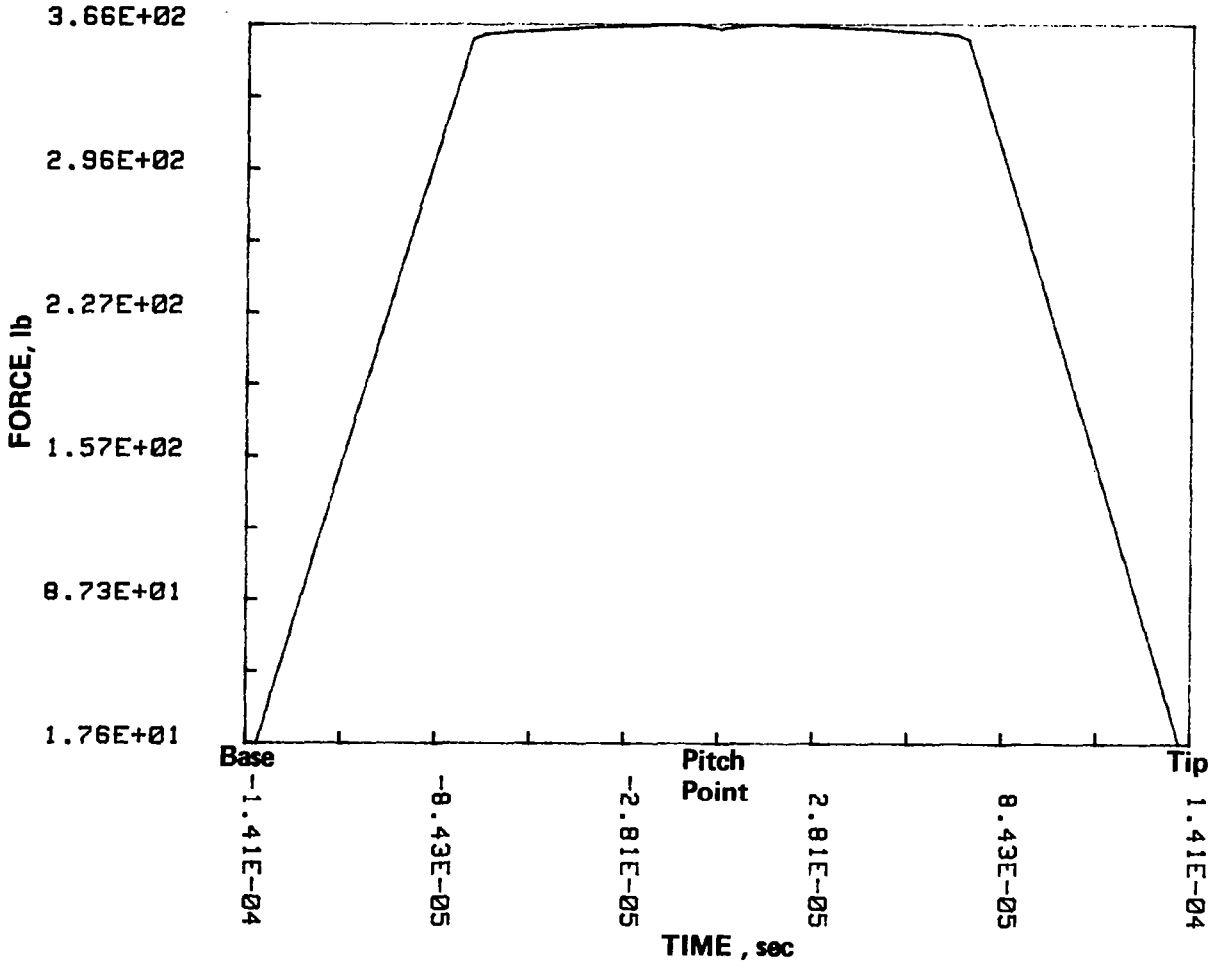

FIG. 23. PREDICTED FORCE HISTORY ON A TYPICAL DRIVING TEST GEAR TOOTH WITH "OPTIMUM" PROFILE RELIEF. ROTATIONAL SPEED IS 10,000 RPM. MESH CARRIES A NOMINAL LOADING OF 1615N (363 LB). PROFILE RELIEF VALUES ARE GIVEN IN TABLE 2. FIGURE EXCLUDES EFFECTS OF DYNAMIC EXCITATION FROM SLAVE GEARS.

For the case shown in Fig. 23, the single tooth loading progresses linearly from zero at $t = -1.41 \times 10^{-4}$ sec to a value of about 363 lb at the instant where the region of single tooth pair contact begins. The loading during the region of single tooth pair contact is almost a constant value growing from about 363 lb to 366 lb and back to 363 lb at the end of the region of single tooth pair contact. During the subsequent region of two tooth pair contact, the loading decreases linearly from 363 lb to zero where contact terminates at the tip. The fluctuation of about 3 lb within the region of single tooth pair contact occurs because the cubic polynomial representation of single tooth compliance that we have used in the computation does not agree *exactly* with the stiffness values computed from the deflections shown in Table 1 — which were used to compute the profile relief values shown in Table 2 (as noted earlier).

Exact implementation of the optimum design procedure results in zero static transmission error $\zeta_{mI}(t)$ for the optimally designed teeth. Thus, for such idealized cases, all Fourier series coefficients α_{mnI} of the static transmission error are zero; hence, the dynamic increment $\delta\zeta^{\dagger}_{mII}(t)$ also is identically zero for these cases, as we may see from Eq. (3.33). It then follows from Eq. (5.14) that the dynamic loading increment $\delta W^{\dagger}_{IjI}(t)$ also is identically zero in these idealized cases so that, for a perfectly designed profile modification, Fig. 23 should be a plot of $W^{\dagger}_{Ij_0}(t)$ which is the loading history experienced by a typical tooth under quasi-static running conditions when inertial effects are negligible. This loading history is the prescribed single-tooth loading function used in the optimal design process — which, for the present case, is shown in Fig. 12. Thus, except for the scaling of the independent variable from roll distance to time, the loading functions in Figs. 12 and 23 should be identical. Examination of the two figures shows that they are very nearly identical except for the approximately 3 lb fluctuation in Fig. 23 within the region of single tooth pair contact that arises from the "error" in the cubic polynomial representation of the single tooth compliance data computed from Table 1.

Comparison of the tooth loading histories shown in Figs. 22 and 23 shows that the maximum value of single tooth loading for the tooth designed for minimum vibration excitation is some 28 lbs larger than the maximum single tooth loading for the teeth designed with linear tip relief (with somewhat undercorrected tips). The reason for this result was implied earlier — namely, the abrupt (step) loading at contact initiation (and termination) of 98.5 lb in the linear tip relief case (that resulted from "undercorrection" of the tips) permits the region of two-tooth pair contact to effectively carry some of the loading that would normally be carried

within the single tooth-pair contact region at lower rotational speeds. This reduction in peak single tooth loading of 28 lbs is a consequence of the rotary inertias associated with the test gears, and would not be observed at substantially lower rotational speeds. *Furthermore, excitation of other parts of a gearing system arising from such undercorrected profiles could—and often will—result in loading increases of such other parts of the system as we shall next show.*

In order to obtain the total force $W^{\dagger}_{Ij}(t)$ on a typical test gear tooth, the dynamic force increment $\delta W^{\dagger}_{IjII}(t)$ must be added to the quantity $[W^{\dagger}_{Ij_0}(t)+\delta W^{\dagger}_{IjI}(t)]$ plotted in Figs. 22 and 23. This fact can be seen from Eq. (5.16), where $\delta W^{\dagger}_{IjII}(t)$ represents the dynamic force increment on a typical tooth j in the test gear mesh (I) from the static transmission error excitation arising from the slave gear mesh (II). The dynamic force increments $\delta W^{\dagger}_{IjII}(t)$ computed for the case of linear tip relief, and then for the case of the profile relief values of Table 2, are shown in Figs. 24 and 25 respectively. These two figures differ for the same reason that the spectra shown in Figs. 20 and 21 differ. That is, in each computation of $\delta W^{\dagger}_{IjII}(t)$, we require the dynamic transmission error increment $\delta\zeta^{\dagger}_{mI\ II}(t)$ according to Eq. (5.15), which in turn is determined from the Fourier series coefficients α_{mnII} of the static transmission error of the slave gears as is indicated by Eq. (3.34). These Fourier series coefficients α_{mnII} are determined essentially by the Fourier series coefficients $\alpha_{(1/K)n}$ of the instantaneous reciprocal of the total mesh stiffness of the slave gear mesh, which were taken to be one-sixth of those for the test gear as indicated earlier. However, the roll distance L over which tooth contact takes place differs for the linear tip relief case in comparison with the profile relief case tabulated in Table 2; hence, the temporal behavior of the instantaneous total mesh stiffness is different for the two cases, as are the Fourier series coefficients of the instantaneous reciprocal total mesh stiffness.

Figures 24 and 25 both are dominated by a single sinusoidal component with a period of about $T = 2\times8.4\times10^{-5}$ sec $\approx 17\times10^{-5}$ sec, as is readily apparent from the time-axis markings in Fig. 25. The frequency of this sinusoidal component is $(1/T) \approx (17\times10^{-5})^{-1} \approx 5880$ Hz. Since, according to Eq. (5.12), the slave gear tooth meshing fundamental frequency is 5833 Hz, it is clear from the above approximate calculation that the dominant sinusoidal component in Figs. 24 and 25 arises from the tooth meshing fundamental frequency of the slave gears. This conclusion is consistent with Eqs. (3.34) and (5.15), and the fact that the

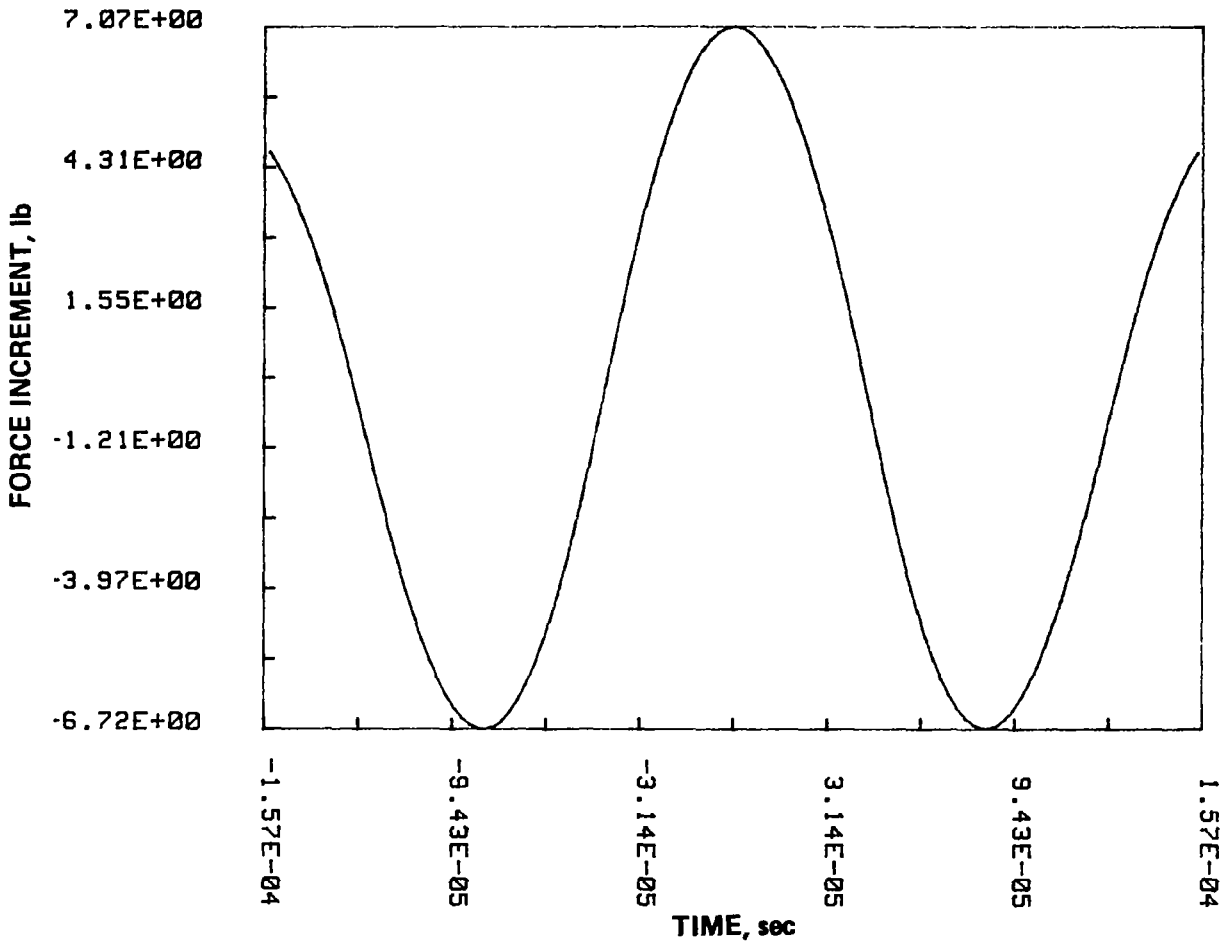

FIG. 24. PREDICTED FORCE INCREMENT ON A TYPICAL DRIVING TEST GEAR TOOTH WITH LINEAR TIP RELIEF THAT RESULTS FROM DYNAMIC EXCITATION PROVIDED BY THE SLAVE GEAR MESH. ROTATIONAL SPEED IS 10,000 RPM. TEST GEAR MESH CARRIES A NOMINAL LOADING OF 1615N (363 LB). ORIGIN OF TIME AXIS IS UNRELATED TO THAT OF FIG. 22.

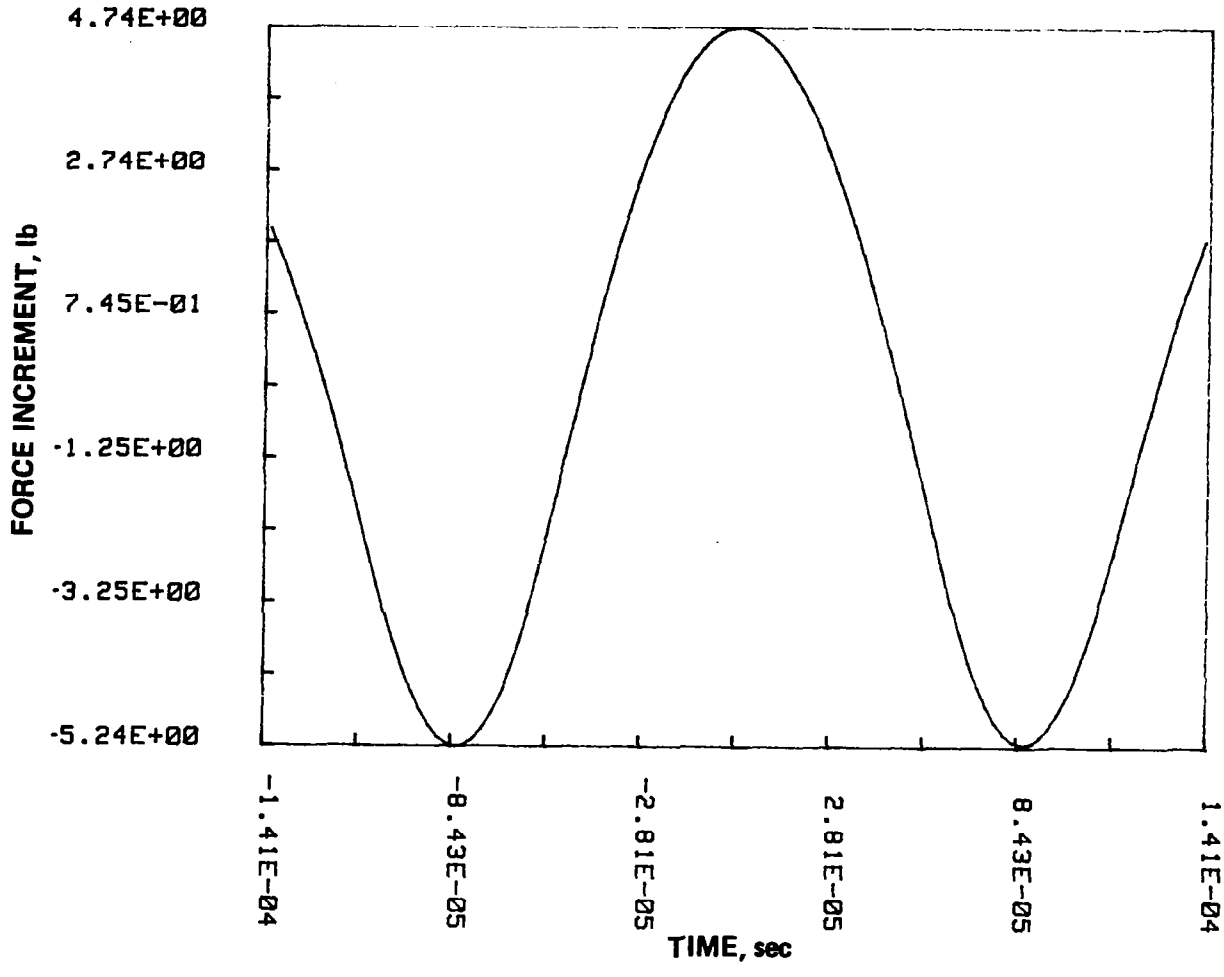

FIG. 25. PREDICTED FORCE INCREMENT ON A TYPICAL DRIVING TEST GEAR TOOTH WITH "OPTIMUM" PROFILE RELIEF THAT RESULTS FROM DYNAMIC EXCITATION PROVIDED BY THE SLAVE GEAR MESH. ROTATIONAL SPEED IS 10,000 RPM. TEST GEAR MESH CARRIES A NOMINAL LOADING OF 1615N (363 LB). ORIGIN OF TIME AXIS IS UNRELATED TO THAT OF FIG. 23.

transmission error "cross" dynamic increment function $Q_{I\ II}(\omega)$ is very nearly zero for all multiples of the slave gear tooth meshing fundamental frequency except for the first which occurs at 5833 Hz as we can see from Fig. 15.

The additional loading of about 5 to 7 lb added to the test gear teeth as a result of the slave gear mesh static transmission error excitation is clearly insignificant. However, this situation is not necessarily typical. For example, if the test apparatus rotational speed of 10,000 rpm were reduced to 6,000 rpm, then the slave gear tooth meshing fundamental frequency would be reduced to $0.6 \times 5833.33 = 3{,}500$ Hz according to Eq. (5.12). From Fig. 15, we see that for this speed reduction, $|Q_{I\ II}|$ would be increased from about $|Q_{I\ II}| \approx 0.43$, which is its approximate value at 5833 Hz to $|Q_{I\ II}| \approx 5.6$ which is its approximate value at 3500 Hz. The fractional increase in $|Q_{I\ II}|$ is $(5.6/0.43) \approx 13$. Consequently, at 6,000 rpm running speed, we could expect a maximum loading increment from the slave gear mesh of about $13 \times 6 = 78$ lb added to the test gear tooth loading from the dynamic excitation provided by the slave gears. This value of 78 lb is no longer an insignificant fraction of the 366 to 338 lb maximum loading seen in Figs. 22 and 23 that arises from the test gear dynamics alone. *The major conclusion to be drawn from this simple exercise is that a significant loading increment on the teeth of one mesh can occur as a result of the dynamic excitation arising from another coupled mesh — in this case the slave gear mesh at 6,000 rpm running speed. To avoid the potential for such effects, it is desirable to minimize the static transmission error excitation from every mesh in a system. Such minimization is accomplished using the profile modification design equations (4.6a) and (4.6b).*

Since there is no fixed phase relation between the teeth on the slave gears and those on the test gears, the time origin in Figs. 24 and 25 must be regarded as completely arbitrary relative to that in Figs. 22 and 23. Hence, the loading shown in Fig. 24 has not been superimposed on that shown in Fig. 22, and the loading shown in Fig. 25 has not been superimposed on that shown in Fig. 23.

Root Stresses on a Single Tooth

From the loading histories shown in Figs. 22 through 25, tooth root stresses can be calculated using Eq. (3.37) and the material derived in Appendix B of this report. Such computations were carried out for the test gears in Fig. 1 using the following parameters:

test gear tooth thickness, $t' = 0.635$ cm (0.25 in) (5.17)

test gear tooth root fillet radius, $r = 0.1016$ cm (0.04 in) (5.18)

Heywood parameter, $\nu = 0.25$ (5.19)

base radius included tooth angle, $\beta = 3.98222$ deg (5.20)

$\ell_m = 4.0909406$ cm (1.6106065 in) (5.21)

$h_0 = 0.56958151$ cm (0.22424469 in), (5.22)

where the last four parameters are defined in Appendix B.

The root stress histories were computed by Eqs. (3.37) and (B.1) (which are the same) using the methodology described in Appendix B. The stress histories computed from the loading history $W_j(t)$ in Fig. 22 are shown in Figs. 26 and 27, which display the root stress histories for the *driven* and *driving* gears respectively. These two stress histories are almost mirror images of each other — their lack of perfect symmetry arises from the lack of symmetry of the loading history in Fig. 22 about the pitch point. This latter lack of symmetry arises from the dynamic increment of the test gear pair response, which is not symmetric about the pitch point. The stress histories shown in Figs. 26 and 27 are for test gears with the linear tip relief as described earlier — these stress histories do not include the stress increments caused by the static transmission error excitation from the slave gears.

The root stress histories computed from the loading history $W_j(t)$ in Fig. 23 are shown in Figs. 28 and 29, which display the stress histories for the *driven* and *driving* gears respectively. These latter two stress histories are almost perfect mirror images of each other — their slight lack of symmetry arises from a very small lack of perfect symmetry about the pitch point of the loading history shown in Fig. 23. The stress histories shown in Figs. 28 and 29 are for test gears with the "optimum" profile relief described earlier. Stress increments caused by the static transmission error excitation from the slave gears are not included in Figs. 28 and 29. Since the tooth loadings (shown in Fig. 22) on the test gears with linear tip relief generally are less (for these particular running conditions) than the tooth loadings (shown in Fig. 23) on the test gears with "optimum" profile relief, we see that the root stresses shown in Figs. 26 and 27 generally run less than those shown in Figs. 28 and 29. In all four stress histories shown in Figs. 26 through 29, the maximum root stress occurs at the instant of the highest point of single tooth contact (nearest to the tooth tip), as expected.

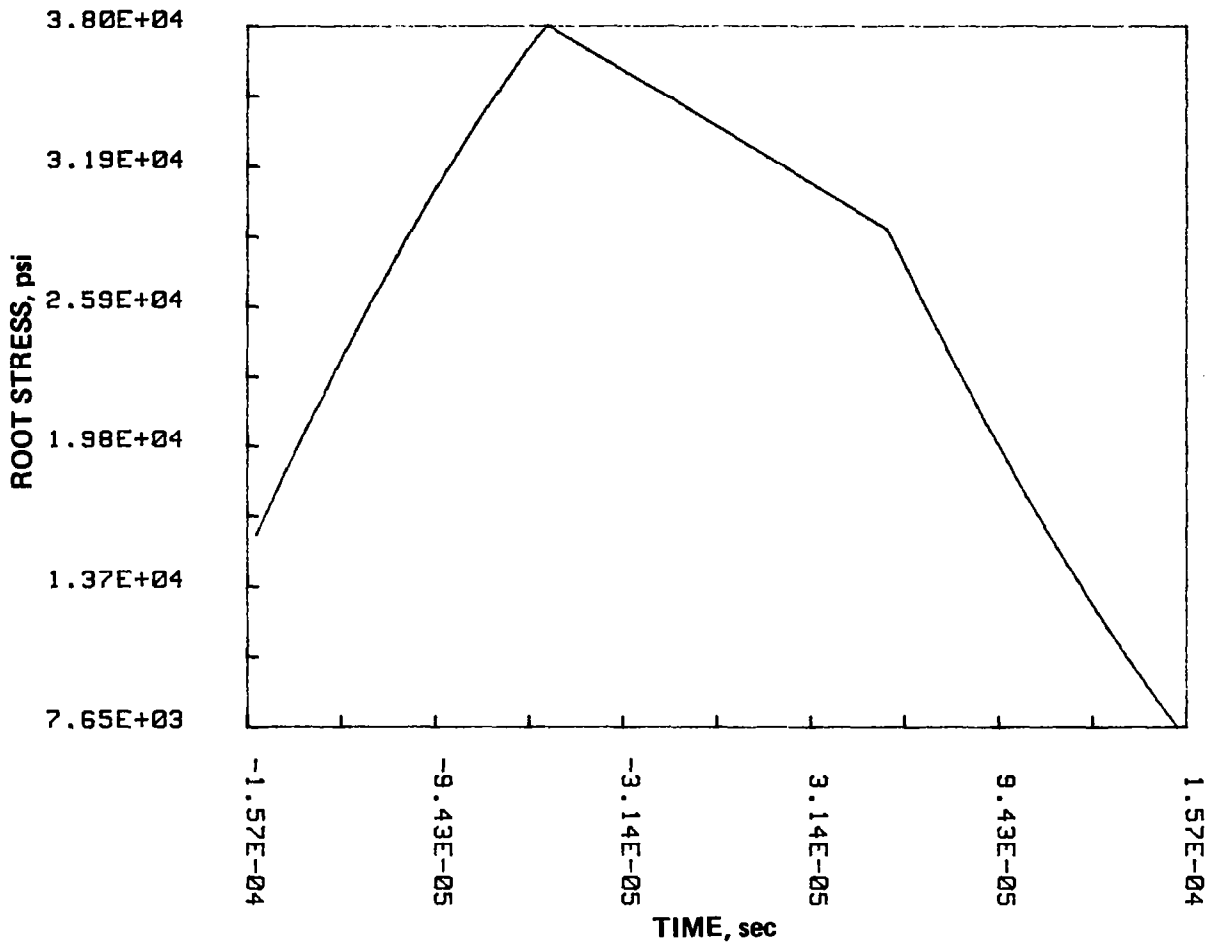

FIG. 26. PREDICTED ROOT STRESS HISTORY ON A TYPICAL TOOTH OF THE DRIVEN TEST GEAR. LINEAR TIP RELIEF CASE. STRESSES ARE PREDICTED FROM FORCE HISTORY SHOWN IN FIG. 22. FIGURE EXCLUDES STRESS INCREMENT ARISING FROM DYNAMIC EXCITATION BY SLAVE GEARS.

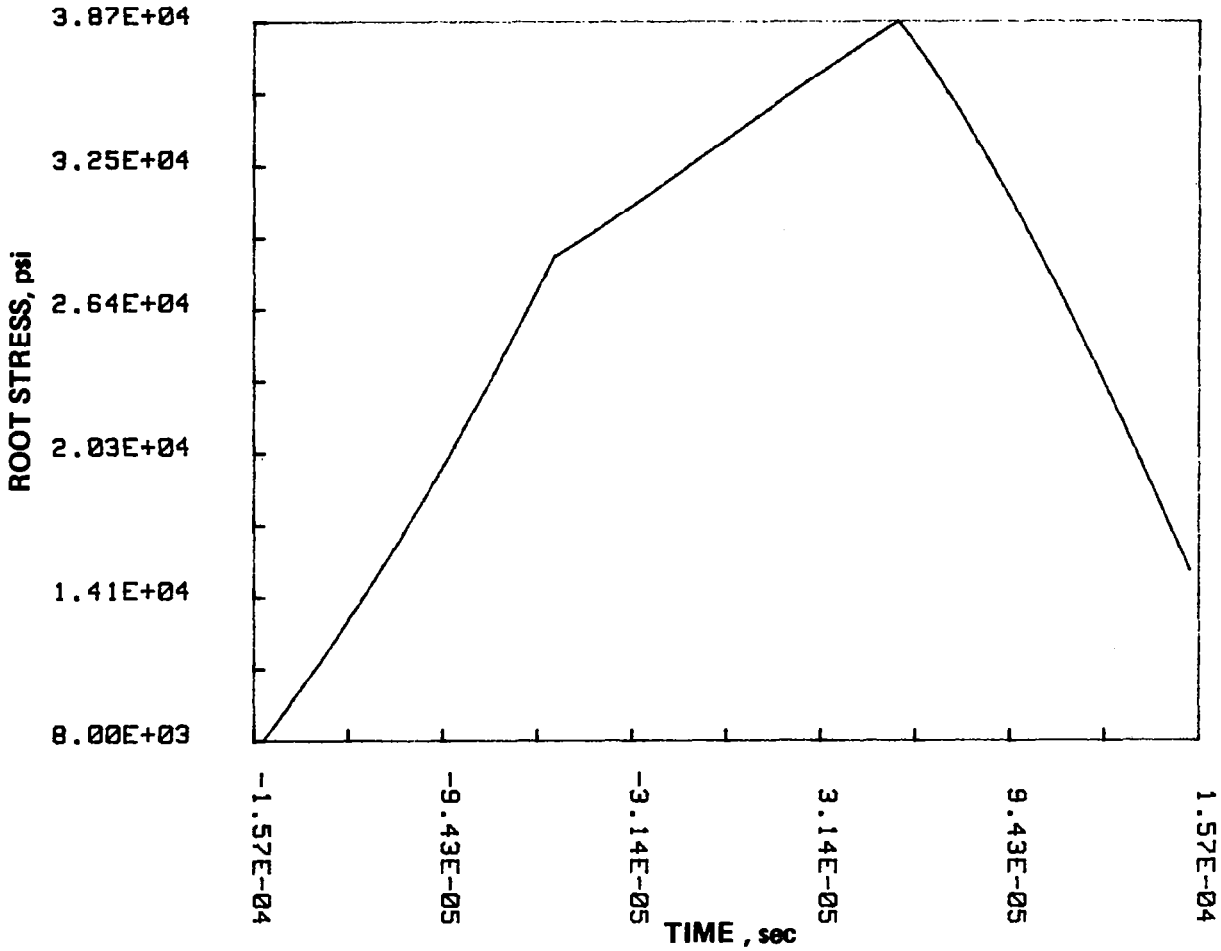

FIG. 27. PREDICTED ROOT STRESS HISTORY ON A TYPICAL TOOTH OF THE DRIVING TEST GEAR. LINEAR TIP RELIEF CASE. STRESSES ARE PREDICTED FROM FORCE HISTORY SHOWN IN FIG. 22. FIGURE EXCLUDES STRESS INCREMENT ARISING FROM DYNAMIC EXCITATION BY SLAVE GEARS.

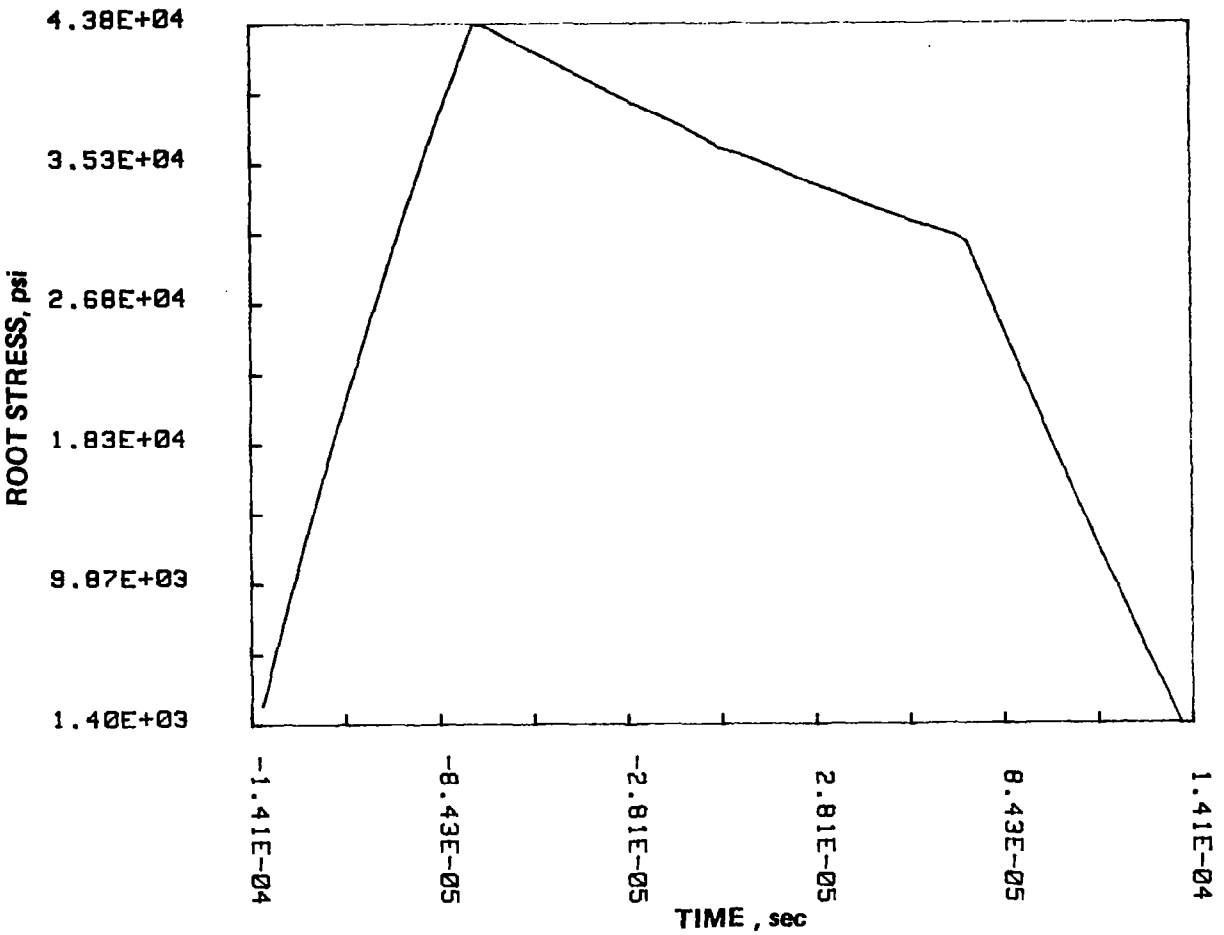

FIG. 28. PREDICTED ROOT STRESS HISTORY ON A TYPICAL TOOTH OF THE DRIVEN TEST GEAR. "OPTIMUM" PROFILE RELIEF CASE. STRESSES ARE PREDICTED FROM FORCE HISTORY SHOWN IN FIG. 23. FIGURE EXCLUDES STRESS INCREMENT ARISING FROM DYNAMIC EXCITATION BY SLAVE GEARS.

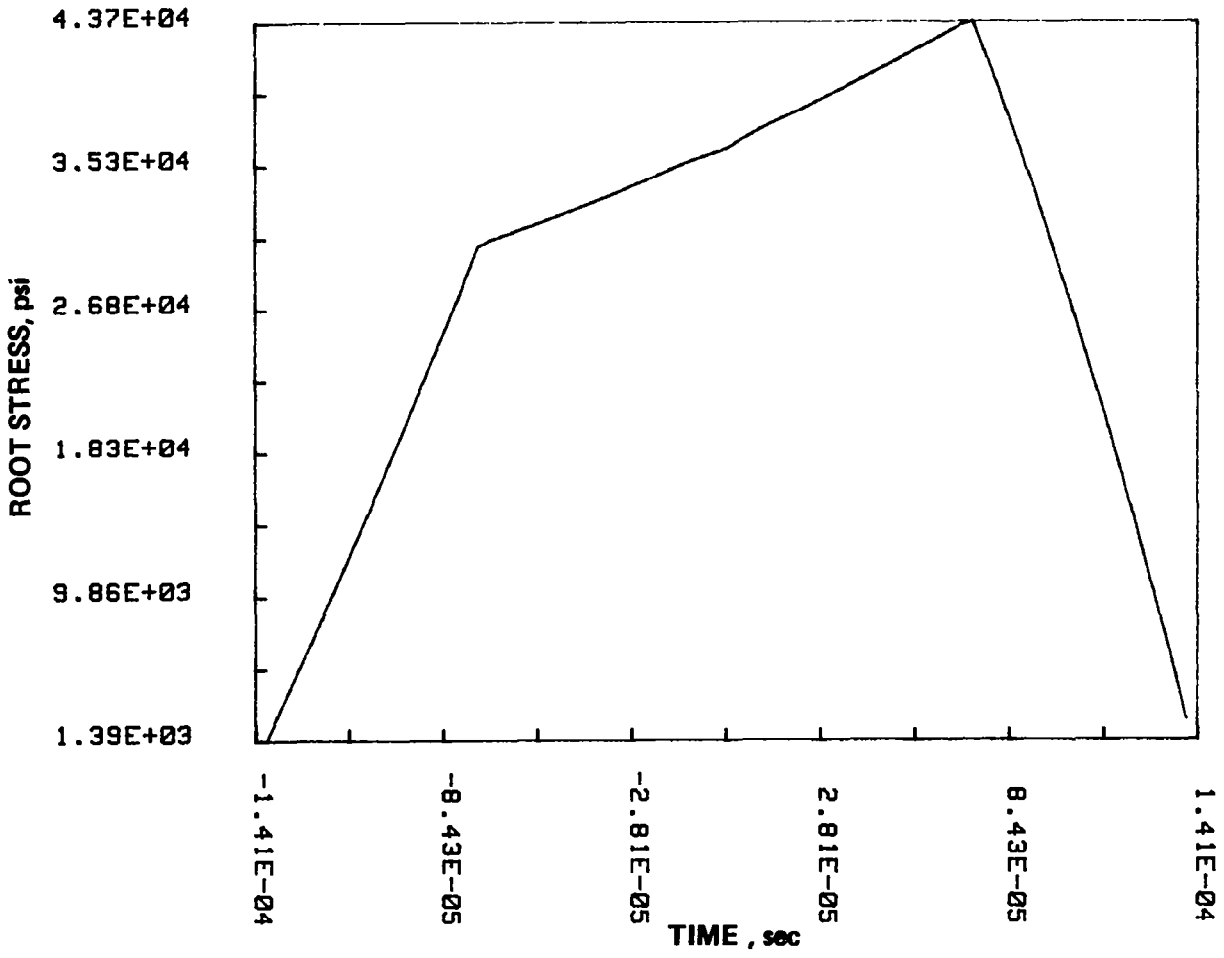

FIG. 29. PREDICTED ROOT STRESS HISTORY ON A TYPICAL TOOTH OF THE DRIVING TEST GEAR. "OPTIMUM" PROFILE RELIEF CASE. STRESSES ARE PREDICTED FROM FORCE HISTORY SHOWN IN FIG. 23. FIGURE EXCLUDES STRESS INCREMENT ARISING FROM DYNAMIC EXCITATION BY SLAVE GEARS.

APPENDIX A

DERIVATION OF EXPRESSION FOR EFFECTIVE LOCAL TOOTH PAIR STIFFNESS

Let $u_j^{(1)}$ and $u_j^{(2)}$ denote, respectively, the elastic deformations of the mating teeth j on meshing gears (1) and (2). Let

$$u_j \triangleq u_j^{(1)} + u_j^{(2)} \tag{A.1}$$

denote the combined deformation of the two mating teeth, where $u_j^{(1)}$, $u_j^{(2)}$, and u_j are defined as positive when they are "equivalent" to removal of material from the tooth surfaces [4]. Let $u_{jj'}$ denote the component of the combined deformation u_j arising from the force transmitted by tooth pair j'. Then u_j can be expressed as the superposition

$$u_j = \sum_{j'} u_{jj'} \tag{A.2}$$

where the summation over j' includes all tooth pairs j' in contact at the particular instant under consideration. Let $c_{jj'}$ denote the deformation of the contact point of tooth pair j arising from a unit force transmitted by tooth pair j' as defined earlier,* and let $W_{j'}$ denote the force transmitted by tooth pair j'. Then,

$$u_{jj'} = c_{jj'} W_{j'} ; \tag{A.3}$$

hence, substituting Eq. (A.3) into Eq. (A.2), we have

$$u_j = \sum_{j'} c_{jj'} W_{j'} . \tag{A.4}$$

Let $\left[k_{jj'}\right]$ be the inverse of the matrix $\left[c_{jj'}\right]$. Then the force W_j transmitted by tooth pair j can be expressed as

$$W_j = \sum_{j'} k_{jj'} u_{j'} , \tag{A.5}$$

---

*The quantity $c_{jj'}$ applies to the tooth pair; thus, we have $c_{jj'} = c_{jj'}^{(1)} + c_{jj'}^{(2)}$ where $c_{jj'}^{(1)}$ and $c_{jj'}^{(2)}$ are as defined in Figure 2.

which is the inversion of Eq. (A.4). Let W denote the total force transmitted by all pairs of meshing teeth — i.e.,

$$W = \sum_j W_j$$

$$= \sum_j \sum_{j'} k_{jj'} u_{j'}$$

$$= \sum_{j'} \left[\sum_j k_{jj'} \right] u_{j'} \qquad (A.6)$$

where Eq. (A.5) has been used in going to the second line and the order of summation has been reversed in going to the third line. Interchanging the roles of j and j' in the last line of Eq. (A.6), we have

$$W = \sum_j \left[\sum_{j'} k_{j'j} \right] u_j$$

$$= \sum_j K_{Sj} u_j \ , \qquad (A.7)$$

where we have defined the effective local tooth pair stiffness as

$$K_{Sj} \triangleq \sum_{j'} k_{j'j} \ . \qquad (A.8)$$

Equation (A.8) expresses K_{Sj} in terms of the elements $k_{jj'}$ of the inverse of the matrix $\left[c_{jj'}\right]$. However, the matrix $\left[c_{jj'}\right]$ does not have to be inverted to compute K_{Sj}. Let $\bar{W}_{j'}$ be the loading distribution in Eq. (A.4) that yields a constant value $u_j = \bar{u}$ independent of j for all $\bar{u}_j$ — i.e.,

$$\bar{u} = \sum_{j'} c_{jj'} \bar{W}_{j'} \ . \qquad (A.9)$$

Then from Eq. (A.5), we have in this case

$$\bar{W}_j = \sum_{j'} k_{jj'} \bar{u}$$

$$= \bar{u} \sum_{j'} k_{jj'}$$

$$= \bar{u} \sum_{j'} k_{j'j} \ , \qquad (A.10)$$

where the last line in Eq. (A.10) is a consequence of Maxwell's reciprocal theorem [p. 9 of Reference 15]. Comparing Eqs. (A.8) and (A.10), we see that

$$K_{Sj} = \frac{\bar{W}_j}{\bar{u}} \; ; \tag{A.11}$$

that is, the solution $\bar{W}_j$, to the matrix equation (A.4) that yields a constant deformation $u_j = \bar{u}$ yields the effective local tooth pair stiffness K_{Sj} when $\bar{W}_j$ is divided by $\bar{u}$. The above derivation is the matrix counterpart to the derivation contained in Appendix B of Reference 4.

Finally, we note that the effective tooth pair stiffness K_{Sj} depends on the position of the point of contact on the faces of the teeth of tooth pair j. When this position is expressed as a function of the coordinate z, K_{Sj} becomes the (effective) local tooth pair stiffness $K_S(z)$ encountered in the first section of this report. Coordinate z is defined in terms of the involute roll angle ε of the tooth under consideration by

$$z = R_b \varepsilon \sin\phi + c \; , \tag{A.12}$$

where R_b is the base circle radius, ϕ is the pressure angle, and the constant c is chosen so that the origin of the coordinate z is placed at the exact midpoint of the range D of z where tooth contact takes place. (Thus, except in the case of identical meshing gears, the origin of z is not generally located at the pitch point.)

APPENDIX B

GEOMETRY REQUIRED FOR EVALUATION OF ROOT STRESS FORMULA PARAMETERS

The modified Heywood formula given by Cornell [8] for the root fillet tensile stress in a gear tooth is

$$\sigma = \frac{W_j \cos\phi'_W}{t'}\left[1+0.26\left(\frac{h_s}{2r}\right)^{0.7}\right] \times\left[\frac{6\ell'_s}{h_s^2}+\left(\frac{0.72}{h_s\ell_s}\right)^{\frac{1}{2}}\left(1-\frac{h_W}{h_s}\nu\tan\phi'_W\right)-\frac{\tan\phi'_W}{h_s}\right] \qquad (B.1)$$

where σ is the root fillet tensile stress at the location indicated in Fig. B.1, t' is the tooth thickness measured parallel to the gear axis, W_j is the instantaneous force normal to the tooth surface that is transmitted by the tooth, $\nu \approx \frac{1}{4}$ according to Cornell [8] and Heywood [9], and the remaining quantities in Eq. (B.1) are defined in Fig. B.1.

Angle γ_s in Fig. B.1 defines the point where the root fillet tensile stress is calculated by Eq. (B.1). Cornell [8] provides an equation for the value of γ_s that locates the position of the *maximum* root stress. Cornell's equation is

$$\tan\gamma_{si+1} = \frac{(1+0.16A_i^{0.7})A_i}{B_i(4+0.416A_i^{0.7})-(\frac{1}{3}+0.016A_i^{0.7})A_i\tan\phi'_W}, \qquad (B.2)$$

where

$$A_i = \frac{h_0}{r} + 2(1-\cos\gamma_{si}), \qquad (B.3)$$

and

$$B_i = \frac{\ell_0}{r} + \sin\gamma_{si}, \qquad (B.4)$$

where h_0 and ℓ_0 are defined in Fig. B.1, and subscripts i and i+1 denote that the transcendental equation (B.2) can be solved iteratively for γ_s with i counting the steps in the iteration procedure.

Once the angle γ_s is determined, the dimension h_s shown in Fig. B.1 also is determined by the formula

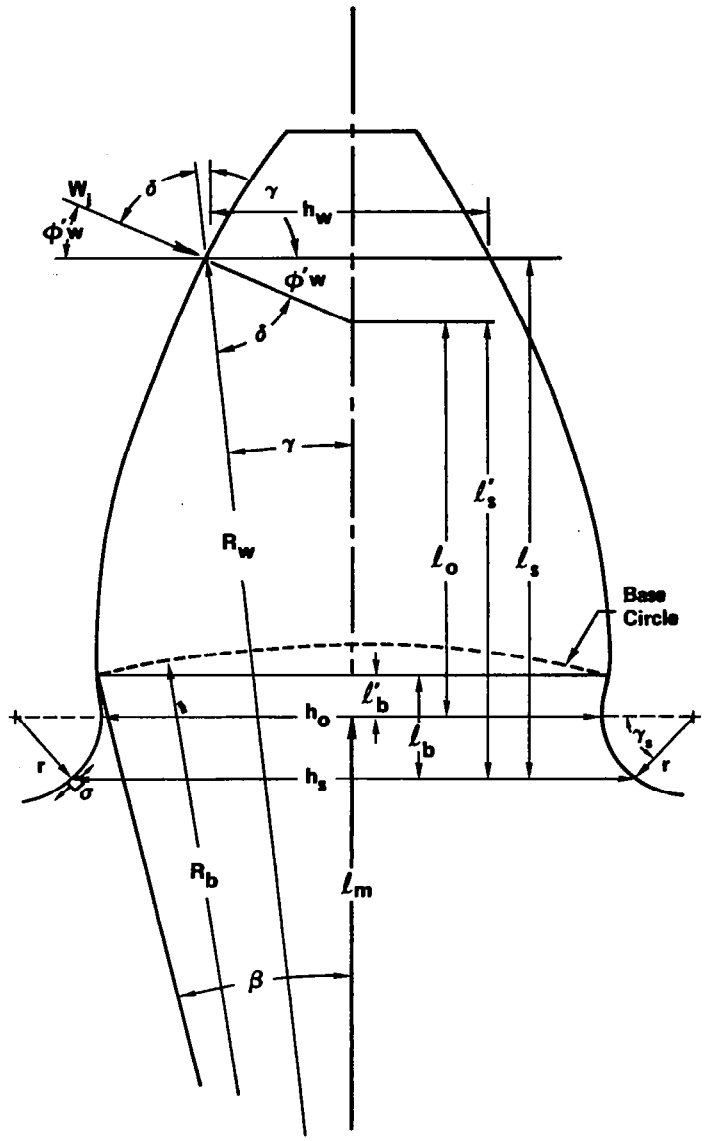

FIG. B.1. TOOTH GEOMETRY FOR EVALUATION OF ROOT STRESS FORMULA PARAMETERS. (ADAPTED FROM CORNELL [8].)

$$h_s = h_0 + 2r(1-\cos\gamma_s) ,$$

as one can readily show from Fig. B.1. The quantities t', r, ν, and h_0 in Eqs. (B.1) through (B.4) are independent of the point of application of loading W_j and the angle γ_s, and therefore may be regarded as constants. Equations (3.23) and (3.29) of this report determine the *magnitude* of the load $W_{Ij} = W_j$ transmitted by a generic tooth j of mesh I.

To utilize Eqs. (B.1) through (B.4) in the present analysis, we must find expressions for the remaining quantities ϕ'_W, ℓ'_s, ℓ_s, h_W, and ℓ_0 in terms of fixed parameters and a variable readily related to time t. Each of the quantities ϕ'_W, ℓ'_s, ℓ_s, h_W, and ℓ_0 is directly dependent on the instantaneous position of tooth pair contact – i.e., the instantaneous position of the load W_j which changes with time as the gears rotate. The "temporal" variable that we shall use here to identify with time is the roll angle ε of tooth j which is illustrated in Fig. B.2. Also shown there is the angle β between the tooth centerline and the intersection of the involute (active) tooth surface with the base circle. Several other quantities required in the present analysis also are defined in Figs. B.1 and B.2.

We shall now derive the following expressions for the above "time-dependent" parameters:

$$\phi'_W = \varepsilon-\beta \tag{B.5}$$

$$h_W = 2R_b(1+\varepsilon^2)^{\frac{1}{2}}\sin\gamma \tag{B.6}$$

$$\ell_s = \ell'_b+r\sin\gamma_s+R_b[(1+\varepsilon^2)^{\frac{1}{2}}\cos\gamma-\cos\beta] \tag{B.7}$$

$$\ell'_s = \ell_s-R_b(1+\varepsilon^2)^{\frac{1}{2}}\sin\gamma\tan(\varepsilon-\beta) \tag{B.8}$$

$$\ell_0 = R_b(1+\varepsilon^2)^{\frac{1}{2}}[\cos\gamma-\sin\gamma\tan(\varepsilon-\beta)]-\ell_m \tag{B.9}$$

where

$$\gamma = \beta-\varepsilon + \arctan\varepsilon. \tag{B.10}$$

When Eq. (B.10) is substituted into the right-hand sides of Eqs. (B.6) through (B.9), the right-hand sides of Eqs. (B.5) through (B.9) all are dependent on only fixed parameters except for the time-dependent roll angle ε.

To show the validity of Eq. (B.5), we note first from Fig. B.1 that

$$\phi'_W = \frac{\pi}{2} - \gamma - \delta. \tag{B.11}$$

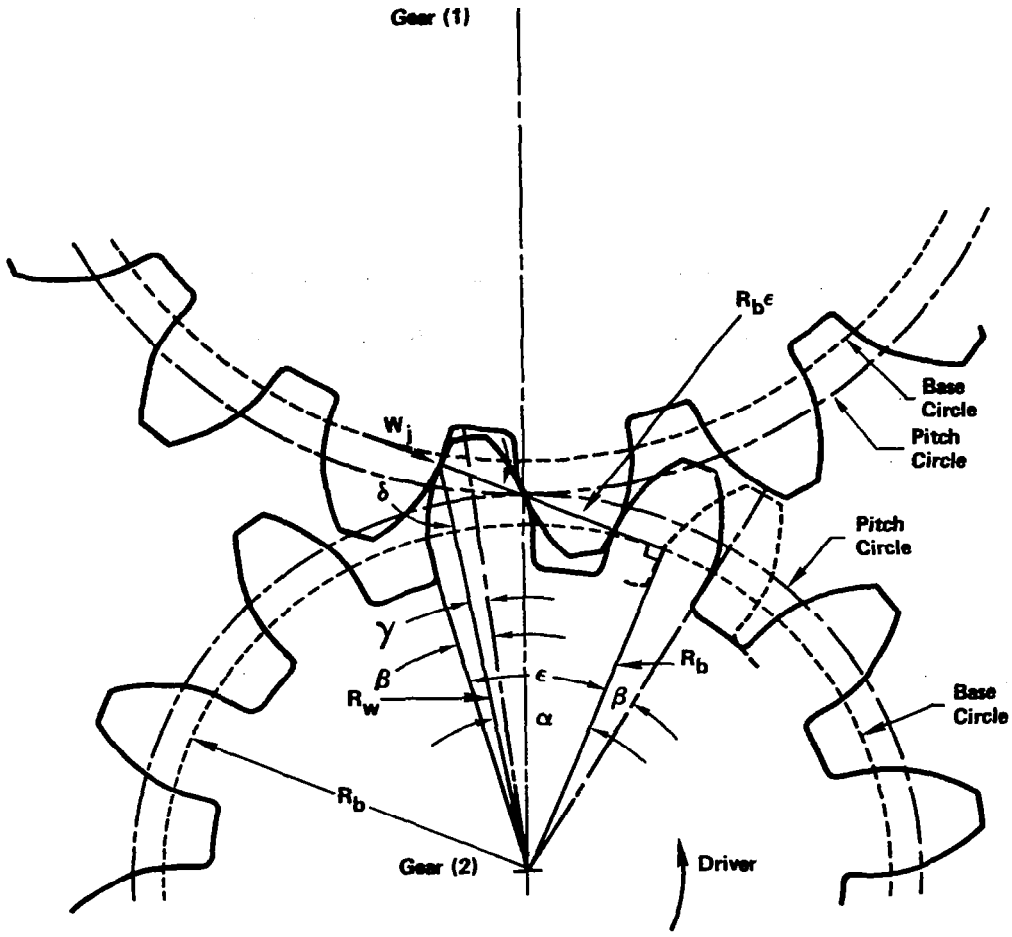

FIG. B.2. GEAR GEOMETRY FOR EVALUATION OF ROOT STRESS FORMULA PARAMETERS.

From Fig. B.2, we see that

$$\gamma = \beta - (\varepsilon-\alpha) = \beta - \varepsilon + \alpha \qquad (B.12)$$

and, also, that

$$\alpha + \delta + \frac{\pi}{2} = \pi$$

or

$$\delta = \frac{\pi}{2} - \alpha. \qquad (B.13)$$

Substituting Eqs. (B.12) and (B.13) into Eq. (B.11) yields Eq. (B.5).

To show the validity of Eq. (B.6), we see from Fig. B.1 that

$$h_W = 2R_W \sin\gamma. \qquad (B.14)$$

From Fig. B.2, we further see that

$$R_W^2 = R_b^2 + (R_b\varepsilon)^2;$$

hence,

$$R_W = R_b(1+\varepsilon^2)^{\frac{1}{2}}. \qquad (B.15)$$

Substituting Eq. (B.15) into Eq. (B.14) yields Eq. (B.6).

Turning to Eq. (B.7), we may see from Fig. B.1 that

$$\ell_s = R_W\cos\gamma - R_b\cos\beta + \ell_b \ . \qquad (B.16)$$

From Fig. B.1, we further see that

$$\ell_b = \ell_b' + r\sin\gamma_s \ . \qquad (B.17)$$

Substituting Eqs. (B.15) and (B.17) into Eq. (B.16) yields Eq. (B.7).

Next, from Fig. B.1, we note that

$$\ell_s' = \ell_s - \frac{h_W}{2}\tan\phi_W' \ . \qquad (B.18)$$

Substituting Eqs. (B.5) and (B.6) into Eq. (B.18) yields Eq. (B.8).

To show the validity of Eq. (B.9), we note from Fig. B.1 that

$$\ell_o = R_W\cos\gamma - \frac{h_W}{2}\tan\phi_W' - \ell_m \ . \qquad (B.19)$$

Substituting Eqs. (B.5), (B.6), and (B.15) into Eq. (B.19) yields Eq. (B.9).

Finally, to show the validity of Eq. (B.10), we note from Fig. B.2 that

$$\tan\alpha = \frac{R_b \varepsilon}{R_b} = \varepsilon. \tag{B.20}$$

Substituting $\alpha = \arctan \varepsilon$ into Eq. (B.12) yields Eq. (B.10).

REFERENCES

1. Zeman, J.: Dynamische Zusatzkrafter in Zahnradgetrieben. Z. Ver. Dtsch. Zucker Ing., Vol. 99, 1957, pp. 244-.

2. Harris, S.L.: Dynamic Loads on the Teeth of Spur Gears. Proc. Inst. Mech. Eng., Vol. 172, 1958, pp. 87-100.

3. Gregory, R.W.; Harris, S.L.; and Munro, R.G.: Dynamic Behavior of Spur Gears. Proc. Inst. Mech. Eng., Vol. 178, 1963-1964, pp. 207-218.

4. Mark, W.D.: Analysis of the Vibratory Excitation of Gear Systems: Basic Theory. J. Acoust. Soc. Am., Vol. 63, 1978, pp. 1409-1430.

5. Mark, W.D.: Analysis of the Vibratory Excitation of Gear Systems. II: Tooth Error Representations, Approximations, and Application. J. Acoust. Soc. Am., Vol. 66, 1979, pp. 1758-1787.

6. Sloane, A.: Engineering Kinematics. Macmillan Co., 1941. (Republished by Dover Publications, 1966.)

7. Hildebrand, F.B.: Methods of Applied Mathematics. Prentice-Hall, 1952.

8. Cornell, R.W.: Compliance and Stress Sensitivity of Spur Gear Teeth. Trans. ASME, Jour. of Mech. Design, Vol. 103, 1981, pp. 447-459.

9. Heywood, R.B.: Designing by Photoelasticity. Chapman and Hall, 1952.

10. Kelley, B.W.; and Pederson, R.: The Beam Strength of Modern Gear-Tooth Design. SAE Trans., Vol. 66, 1958, pp. 137-157.

11. Harris, S.L.: Dynamic Loads on the Teeth of Spur Gears. Proc. Inst. Mech. Eng., Vol. 172, 1958, pp. 87-100.

12. Gregory, R.W.; Harris, S.L.; and Munro, R.G.: Dynamic Behavior of Spur Gears. Proc. Inst. Mech. Eng., Vol. 178, 1963-1974, pp. 207-218.

13. Remmers, E.P.: Analytical Gear Tooth Profile Design. ASME Paper No. 72-PTG-47, October 1972.

14. Kasuba, R.; and Evans, J.W.: An Extended Model for Determining Dynamic Loads in Spur Gearing. Trans. ASME, Jour. of Mech. Design, Vol. 103, 1981, pp. 398-409.

15. Fung, Y.C.: Foundations of Solid Mechanics. Prentice-Hall, 1965.

16. Timoshenko, S.P.; and Goodier, J.N.: Theory of Elasticity, 3rd ed., McGraw-Hill Book Co., 1970.

17. Sigg, H.: Profile and Longitudinal Corrections on Involute Gears. AGMA Paper 109.16, October 1965.

18. Coy, J.J.; and Chao, C. Hu-Chih.: A Method of Selecting Grid Size to Account for Hertz Deformation in Finite Element Analysis of Spur Gears. ASME Paper No. 81-DET-116, September 1981. (To appear in Trans. ASME, Jour. of Mech. Design.)

1. Report No.	2. Government Accession No.	3. Recipient's Catalog No.
NASA CR-3626		

4. Title and Subtitle	5. Report Date
THE TRANSFER FUNCTION METHOD FOR GEAR SYSTEM DYNAMICS APPLIED TO CONVENTIONAL AND MINIMUM EXCITATION GEARING DESIGNS	OCTOBER 1982
	6. Performing Organization Code
7. Author(s)	8. Performing Organization Report No.
William D. Mark	4712
	10. Work Unit No.
9. Performing Organization Name and Address	11. Contract or Grant No.
Bolt Beranek and Newman Inc. 10 Moulton Street Cambridge, Massachusetts 02238	NAS3-21978
	13. Type of Report and Period Covered
12. Sponsoring Agency Name and Address	Contractor Report
National Aeronautics and Space Administration Washington, D. C. 20546	14. Sponsoring Agency Code
	511-58-12 (E-1208)

15. Supplementary Notes

Final report. Project Manager, John J. Coy, Propulsion Laboratory, AVRADCOM Research and Technology Laboratories, Lewis Research Center, Cleveland, Ohio 44135.

16. Abstract

A transfer function method for predicting the dynamic responses of gear systems with more than one gear mesh is developed and applied to the NASA Lewis four-square gear fatigue test apparatus. Methods for computing bearing-support force spectra and temporal histories of the total force transmitted by a gear mesh, the force transmitted by a single pair of teeth, and the maximum root stress in a single tooth are developed. Dynamic effects arising from other gear meshes in the system are included. A profile modification design method to minimize the vibration excitation arising from a pair of meshing gears is reviewed and extended. Families of tooth loading functions required for such designs are developed and examined for potential excitation of individual tooth vibrations. The profile modification design method is applied to a pair of test gears.

17. Key Words (Suggested by Author(s))	18. Distribution Statement
Vibration Gears Transmissions Noise	Unclassified - unlimited STAR Category 37

19. Security Classif. (of this report)	20. Security Classif. (of this page)	21. No. of Pages	22. Price*
Unclassified	Unclassified	110	A06

* For sale by the National Technical Information Service, Springfield, Virginia 22161

NASA-Langley, 1982